ION GENARATION, DEFLECTION AND DEPOSITION IN VACUUM

LUNGA CLEOTON BAM

A thesis submitted in fulfilment of the Degree of Magister Scientiae in the faculty of Natural Sciences
University of the Western Cape

SUPERVISOR: MR R.T DOBSON
CO-SUPERVISOR: PROF R LINDSAY

Department of Mechanical Engineering, University of Stellenbosch

March 2010

Declaration

I declare that the Ion Generation, Deflection and Deposition in Vacuum is my own work, that it has not been submitted before for any degree or examination in any university, and that all the sources I have used or quoted have been indicated and acknowledged as complete references.

Lunga Cleoton Bam

March 2010

Signed:

Key words

Arc Discharge

Cathodic Arcs

Collimator

Corona

Graphite Dust

Ion Source

Macroparticles

Silver-110m

Thermionic Arcs

Vacuum Arc

Abstract

ION GENERATION, DEFLECTION AND DEPOSITION IN VACUUM

L. C. Bam

L. C. Bam thesis, Department of Physics, University of the Western Cape.

In the PBMR it is known that at high temperatures (above 1250 °C) silver-110m is known to have been released from the TRISO particles and taken up by the helium coolant stream. The released silver-110m travels with the helium through the reactor, plates-out on the wall of the power conversion unit and is radioactive with a half-life of 245 days. In order to get a better idea of the dynamic behaviour of silver particles this thesis was initiated with the specific objective of building an experimental apparatus in which silver ions could be generated, deflected and collected on a target plate in vacuum. A literature study was conducted to find a method to produce the silver ions and resulted in the choice of using an electric arcing method to generate the ions.

Four different silver electrode geometries (ion sources) were developed and tested using different arc voltages in the range of kilovolts to generate the silver ions. The first and second design of the ion source used two flat electrodes separated by a glass insulator, central rod and outer sheet electrodes separated by glass tube insulator respectively. Both ion sources used arc voltages between 1.0 and 10.0 kV. The ion sources stopped working because of their sensitivities to high voltage and deposition of silver ions was not observed on the target plate. The third design of the ion source used two silver needle-like rods with 1.0 mm separation distance. The ion source made use of a very high arc voltage ($\approx$ 20 kV) because an arc could not be initiated and sustained using the same range of arc voltage used to the first and second design of the ion sources. The extraction, acceleration, and deflection voltages used were -2.5, -3.0 and 1.0 kV respectively. The results obtained using the third design of the ion source showed that more neutral particles were produced compared to charged particles. This ion source was thus discontinued.

The final (fourth) design of the ion source comprised of a central rod and outer sleeve of silver electrodes separated by a Teflon insulator. With the final design of the ion source sustainable arcs at 2.0 kV were obtained. Deflection voltages used were 1.0, 1.5 and 2.0 kV and the extraction voltage used was -3.0 kV. The experimental and theoretical deflection results obtained using deflection voltages of 1 and 2.0 kV are 2.14 mm and 4.59 mm, and 2.42 mm and 4.88 mm respectively, for an electric field deflection length of 25.0 mm and a target distance from the deflector plates of 10.0 mm. The experimental results so obtained are in agreement with the theoretical results to within 11.6% and 5.9%, respectively.

March 2010

Acknowledgements

I would like to thank the following individuals who made this work possible:

- To my supervisors, Mr Robert Dobson and Prof Robert Lindsay for their guidance, supervision and support through out this project.
- Mr O.O Kritzinger for the designs and building the apparatus.
- PBMR for their financial support throughout the project.
- Dr Rainer W. Thomae for his time and assistance whenever there was a problem.
- Gerrit deVilliers for building the power supplies.
- Mr Ulrich Buttner for lending us his power supplies.
- iThemba Labs for lending us their power supplies.
- Stellenbosch Physics Department.
- Kgothatso Maduse for patiently waiting, loving and supporting me throughout the project.
- Leanne Haworth for helping in structuring and writing the thesis.
- My family for their prayers, love and support.

Dedication

To my parents, if it was not for them I would not be here.

Nomenclature

Abbreviations

AVIS	Advanced Vacuum-Arc Ions Source
AVR	Arbeitsgemeinschaft Versuchsreaktor
DV	Deflection Voltage
HIF	Heavy Ion Fusion
HTGR	High Temperature Gas Cooled Reactor
HTR	High Temperature Reactor
IGDDV	Ion Generation Deflection Deposition in Vacuum
MEVVA	Metal Vapour Vacuum Arc
MIS	Magnetic Isotope Scrubber
MWe	Megawatt Electrical
PBMR	Pebble Bed Modular Reactor
RPCU	Reactor Power Conversion Unit
PyC	Pyrolytic Carbon
SD	Standard Deviation
SE	Standard Error
SiC	Silicon Carbide
TRISO	Three Isotropic Layers
THTR	Thorium High Temperature Reactor

Roman Symbols

a	acceleration of the particle, $m.s^{-2}$
A	universal Richardson constant, $A/(m^2.K^2)$, surface area, mm^2
AV	arcing voltage, kV
b	impact parameter, maximum impact parameter
B	ratio of cross sectional area of the axis
C_h	is specific, J/(kg.K)
CI	confidence interval
d	separation distance of the deflector length, mm
D	length of deflector plate, mm, diameter of the beam spot, mm
e	elementary charge, electron charge, C
E	electric field, V/m, total energy at the anode, eV
$E(Q)$	total energy, eV
E_Q	ionization energy of ions, eV
$E_{kin}, E_{kin}(Q)$	kinetic energy, eV, average kinetic energy, eV
EV	extraction voltage, kV
E_s	energy of the ion at the cathode, eV
f	electron beam fraction
F	force, N, parameter depending on geometry and current, $kg/(s^{5/2}.A)$
h	separation distance of the grid points
$\hbar$	Plank's constant, $\hbar = 1.055 \times 10^{-34}$ J.s

H	hardness, (s^2.mm)/kg
I	current, A
j_e	current of an electron, A
J	current density, A/m^2
K	thermal conductivity, W/(m.K), wear coefficient for adhesive wear
k	Boltzmann's constant, k = 1.38 x 10^{-23} J/K
k_C	Coulomb's constant, k_c = 8.99 x 10^9 (N.m)/C^2
k_h	coefficient of the heat conductivity, W/(m.K)
kTe	electron enthalpy, J
L	distance from the deflector plate to the target, mm, length slide, mm
L'	distance from the middle of the deflector plate to the target, mm
l_c	collimator distance from the ion source, mm
l_r	radius of the collimator, mm
l_R	resultant, mm
L_{Ti}	distance of target plate from the ion source, mm
m	mass, kg
M	average experimental deflection, mm
N	normal force, N
n_o	neutral density, kg/m^3, plasma density, (A.s)/mm^3
P	power density, W/m^2
p	initial momentum, (kg.m)/s^1, equilibrium vapour pressure, Torr
q_1, q_2	charge of the particles, C
Q	charge state number, C, charge of the source particle, C,
$\bar{Q}$	mean charge state, C
$Q(h)$	heat transferred by gas enthalpy, eV
$Q(R)$	net input radiation, eV
r	distance between particles, mm, radius of the beam spot, mm
S	surface area of the electrode wall, m^2
SD	standard deviation
SE	standard error
t	time, s
T	temperature, K
$T_m(K\rho C_h)^{1/2}$	thermal characteristic, kg/$s^{5/2}$
U	potential difference, V, bias voltage, V, plasma sheath potential, V
v	beam frequency, s^{-1}, velocity, m/s
V	voltage, V, wear volume, mm^3, potential difference of ions, V
V_{sheath}	voltage drop in the sheath, V
V_x	deflection voltage, mm
W	cohesion energy, J
X	experimental deflection, mm
y, y'	transverse deflection of ions, mm, total transverse deflection of ions, mm

Greek symbol

ε	emission coefficient of the substrate
ε_r	dielectric constant

ε_o	permittivity, $C^2/(N.m^2)$
ϕ	cathode wall potential, eV, ion potential, eV, sheath potential, eV
ξ	is an area factor related with plasma and shape of substrate ,m^{-2}
σ	Stefan constant, $\sigma = 5.6 \times 10^{-8}$ $W/(m^2.K^4)$, charge density, C/mm^2
σ_m	momentum transfer, (kg.m)/s
σ_{bi}	cross section, m^2
Ψ	work function of anode, eV, work function of the metal, eV
β	angle at which silver ions were produced, degrees
φ_w	electron work function, eV
Γ	atom emitted flux, $(atoms/m^2.s)$, equilibrium vapour flux, $mol/(m^2.s)$
ρ	mean density, kg/mm^3
Δp	change in momentum, (kg.m)/s
Δx	length of the axis which heat is conducted, mm

Subscripts

a	anode
ad	adhesive
as	anode spot
avc	average current
b	bombardment
B	Boltzmann's
be	beam excitation
bi	beam ionization
BP	boiling point
c	heat conductivity, collimator
coh	cohesion
d	radiation
dc	direct current
e	electron
ew	electron emission
fl	floating substrate
h	heat
i	running index, ion, ionization
kin	kinetic
m	melting point, momentum
max	maximum
n	neutral particle/atom
o	environmental
0	initial point
ow	equilibrium vapour
p	particle, plasma
pl	plasma sheath
pw	plasma wall
Q	ionization
r	radius
R	resultant

s	surface, source particle, sheath
st	substrate temperature
t	total
Ti	target
w	wall
w'	anode
w''	cathode
x	x-axis, longitudinal
y	y-axis, transverse

List of figures

List of tables

Contents

Chapter 1

1 BACKGROUND, MOTIVATION AND OBJECTIVES

1.1 Introduction

The genesis of the PBMR (pebble bed modular reactor) design began with the German high-temperature reactor (HTR) development programme. This programme included two operational prototypes, the 15 MWe AVR and the 300 MWe thorium high temperature reactor (THTR). The concept of the PBMR design brings together the direct coupling of the high-temperature reactor system to a gas turbine and the achievement of a very high level of passive safety without the use of active engineering systems. The direct cycle gas turbine excludes the complex and costly steam cycle for power conversion and results in a much higher thermal efficiency. Passive safety is achieved by making use of high-integrity particle fuel that has a strong negative temperature coefficient and large thermal capacity. This concept of the PBMR was introduced to South Africa in 1993 due to the anticipated future growth in electrical demand (Ion, *et al.* 2004).

The PBMR reactor is a small, modular reactor that is helium cooled and graphite moderated. It makes use of spherical fuel elements called pebbles which are approximately the size of the tennis ball. These pebbles are loaded into the top of the reactor (Cogliati, and Ougouag, 2008) and they travel down the reactor to the outlet chute below. At the bottom of the reactor the pebbles are removed and the degree of burn up of the fuel determines whether the pebble will be reused or permanently removed. As these pebbles travel through the reactor they produce graphite dust which acts as a site for the deposition of radioactive particles. This dust travels through the cooling system and the coolant (helium) becomes radioactive. The graphite and impurities are the primary source of ionizing radiation away from the fuel elements. It is known that at high temperatures radioactive Ag-110m is released from the TRISO (three isotropic layers) particle. The released silver is one of the isotopes which causes the coolant to become radioactive. As the Ag-110m travels with the helium through the reactor it plates out on the walls of the reactor.

The focus of this thesis is on silver ions, to find and make use of an appropriate method of generating them and then to extract, accelerate and deflect the generated ions. The deflected ions must be collected on a glass target plate where they will be observed. It must be ensured that the chosen method generates silver ions, as opposed to neutral particles. Chapter 2 of this thesis discusses the method chosen and the processes involved in generating these ions. Chapter 3 gives a brief description of the application and the theory of electrostatics. Chapter 4 discuses the experimental work and all the results found. Chapter 5 provides the overall discussions and conclusions of the research.

1.2 Graphite as a sphere carrying the fuel

The PBMR core contains about 452000 pebbles which are packed in a reactor pressure vessel that is approximately 2 m in diameter and 11 m tall. Only 75 % of the pebbles contain the nuclear fuel. The remaining pebbles are pure graphite. The pebbles with fuel contain 15000 microspheres of uranium fuel that must be specially fabricated. The 0.5 millimetre internal microsphere is enriched uranium (up to 9.6 %

U-235). This fuel is coated with a dense layer of pyrolytic carbon (PyC), a layer of silicon carbide and an outer pyrolytic carbon layer (OPyC) (Harding, 2004). The low density graphite provides a volume for gaseous fission products, accommodates kernel swelling and represents a sacrificial layer for fission fragments. The inner, dense pyrocarbon layer acts as a gas-tight coating, diffusion barrier for metallic fission products to protect the kernel from Cl_2 and to reduce tensile stresses in the SiC layer. The high density silicon carbide (SiC) layer retains the pressure and acts as a diffusion barrier for primary metallic fission products. The outer high density pyrolytic carbon layer also acts as a diffusion barrier for gaseous and metallic fission products and reduces tensile stress on the SiC, protecting the silicon carbide during particle handling and sphere/compact formation (Verfondern, *et al.* 2007).

After all the coatings have been applied the TRISO sphere is slightly less than 1 mm in diameter. 15000 TRISO spheres are mixed into a graphite matrix of 50 mm diameter and covered with a pressed and sintered 5 mm layer of graphite to form a pebble about 60 mm in diameter. The presence of graphite and the core geometry play a vital role with regard to inherent safety. The graphite yields a power density of less than 5 MW thermal per cubic meter. The surface area of the pebbles and the mass of the core create much opportunity to dissipate decay heat (Harding, 2004).

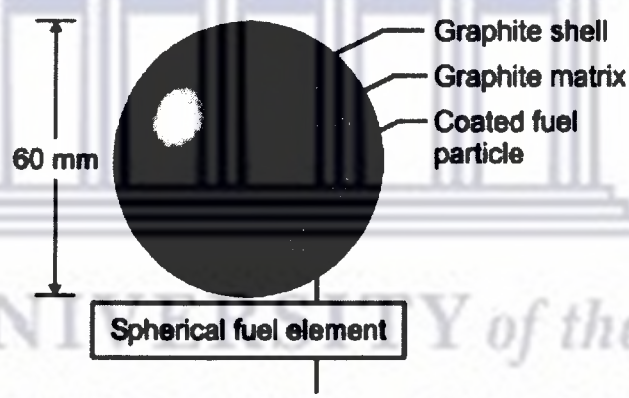

Figure 1-1 Spherical graphite pebble containing fuel element (Verfondem, *et al.* 2007)

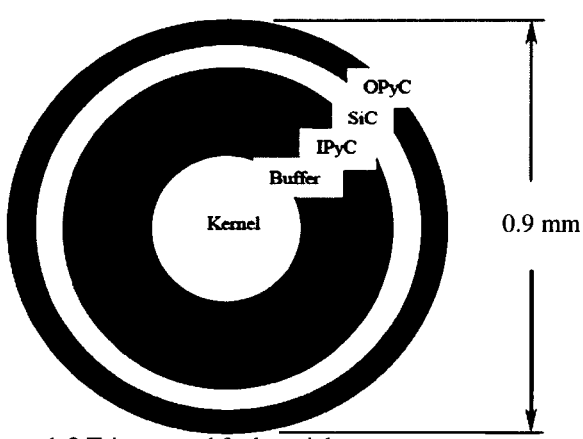

Figure 1-2 Triso coated fuel particles

1.3 Graphite dust formation

The pebbles are loaded into the top of the reactor and move to the outlet chute below. As they move down the reactor they slide against each other and the resulting wear produces graphite dust. The moving pebbles do not only rub against each other, but also against the surfaces that they come into contact with, including the fuel handling system and graphite reflector in the core. The exact dust production depends on the microscopic surface conditions of the graphite. Relevant factors contributing to the wear rate include the temperature, atmosphere, normal forces and history of collisions/wear. The first order approximation for calculating the production volume (Ougouag, *et al.* 2008) is

$$V = K_{ad} \frac{N}{H} L \qquad 1.1$$

where V is the wear volume, mm^3
K_{ad} is the wear coefficient for adhesive wear
L is the length slide, mm
N/H is the real contact area, mm^2
N is the normal force, N
H is the hardness, $(s^2.mm)/kg$

This dust is a concern because it is radioactive and travels through the cooling system together with helium. The graphite and its impurities are sources of ionizing radiation from the fuel elements. This dust can also decrease the efficiency of the heat exchangers and graphite particles colliding with turbine blades would decrease the operating lifetime of the blades (Ougouag, *et al.* 2008).

1.4 The release of silver-110m from the pebbles

The fuel performance depends on temperature, the fast fluent and the burn-up trajectory experienced during service, which varies spatially within the core. The modular high temperature gas-cooled reactor (HTGR) concept, with its emphasis on the passive safety features, relies upon the capability of the fuel to retain radionuclides to a very high degree during both normal operation and accident conditions. Irradiation tests were conducted by Verfondern (2007) to demonstrate appropriate fuel performance. It was found that the irradiation caused the kernel to swell and the buffer layer to shrink. During irradiation the PyC shrinks in both the radial and tangential direction and the fission gases are released from the kernel into the porous buffer layer (Verfondern, *et al.* 2007). The inner pressure builds up from the accumulation of fission gases and CO (carbon monoxide) which increase with burn up. This results in tensile stresses on the dense coating layers of the particle.

The coating on the fuel pellets begins to lose effectiveness at 1250 °C. If operation allows the fuel temperature to exceed of 1250 °C over an extended period of time the SiC (silicon carbide) coating thickness deteriorates due to palladium attack. This condition can lead to fission product release which would create maintenance problems in the case of an accident, because Ag-110m plates-out on the surrounding materials. At high temperatures Ag-110m is released from the TRISO particle. Not knowing the extent of Ag-110m release as well as continuous high temperature operation may significantly increase the maintenance considerations on the reactor

power conversion unit (RPCU) components. It could also cause deterioration of the life of the turbine blades (Harding, 2004).

1.5 Motivation and objectives of the study

1.5.1 Motivation

Previous work was done by (Monageng, 2010) using a Magnetic Isotope Scrubber (MIS) method to deflect silver ions in vacuum. Monageng's results showed that deflection of silver ions in vacuum using MIS is possible, but the degree of deflection was not determined. The focus of this thesis is to use an electric field to deflect the silver ions in vacuum, because electric forces are larger than magnetic forces. The degree of deflection of the silver ions must be determined. Successfully deflecting the silver ions in vacuum will lead to another study to be conducted during which these ions will be deflected in helium. The success of these projects will play an important role in the PBMR reactor where silver is known to plate out on the surrounding materials of the reactor. The released silver from the pebbles is radioactive which is potentially harmful if the personnel are exposed to it. The released silver from the pebbles will be deflected, collected and safely stored until the radiation levels of silver are low enough for normal maintenance to be done.

1.5.2 Objectives of the study

The main objectives of the study are to:

- Generate silver ions using a reliable method to generate ions.
- Extract and accelerate the generated beam of silver ions.
- Collimate and focus the silver ion beam to the target plate.
- Deflect the accelerated silver ion beam with an electric field in vacuum.
- Collect the deflected silver ion beam on the target plate.
- Measure the deflected silver deposit on the target plate to determine the degree of deflection.

In order to achieve the main objectives it is necessary to construct an experimental apparatus with which the experimental work can be performed. This apparatus must be able to generate uniform electric fields and should be designed so that the deflection and plate-out process can be visually observed during the operation of the experiment.

Chapter 2

2 LITERATURE SURVEY AND THEORY

This literature study gives background theory of the physical processes that take place during arcing.

2.1 Introduction

A vacuum arc is a high current, low voltage electrical discharge (Boxman, *et al.* 1995) between two electrodes situated in a vacuum (Grissom, and McClure, 1971). Vacuum on its own cannot support a high current discharge at low voltage and so a conducting medium is required. Arcing creates its own medium in the form of a highly ionized plasma of vaporized electrode material, produced by an intensive interaction of a plasma (ionized gas) with the electrodes (Siemroth, *et al.* 1995). The plasma produced by vacuum discharges is very similar to laser induced plasma (Siemroth, *et al.* 1997). It is fully ionized with an average electron temperature between 1 eV and 3 eV and is fast expanding, with even higher kinetic energies between 50 eV and 250 eV (corresponding to velocities in the range of 10-30 km/s).

An electrical discharge is the passage of an electrical current through a medium or device which is normally insulating and it is a source of charged and neutral particle under vacuum conditions (Fuchs, *et al.* 1998). An example is lightning, where the medium is air which under normal conditions is a very poor conductor. However, when a sufficiently high voltage or electrical field is applied, breakdown occurs, and the medium changes state from an insulator to a conductor. Some fraction of the atoms and molecules present in the medium become ionized, forming a plasma, and the electrical current is conducted primarily by the movement of free electrons, with some contribution also made by ion movement (Boxman, *et al.* 1995).

In most vacuum arcs having currents less than a few kA, the production of plasma is localized at one or several minute locations on the cathode, known as cathode spots. The highly visible cathode spot is the most striking and highly studied aspect of the arc. In addition to providing the conducting medium, the cathode spots also supply the mechanism for releasing electrons from the generally cool electrode. With all of the arc current concentrated in minute areas, local conditions of extremely high temperature and electrical field occur. If the current was distributed uniformly neither sufficient electrons nor plasma production could occur (Boxman, *et al.* 1995).

2.2 Formation of an arc

Arc discharge is the most convenient way to generate the thermal plasma as shown in figure 2.2 (Ushio, M. 1988). The arc consist of three major sections namely the arc column, the cathode region and the anode region (as shown in figure 2.1). The column has charge equilibrium, low electric field and high temperature. These conditions play an important role in heating the gas.

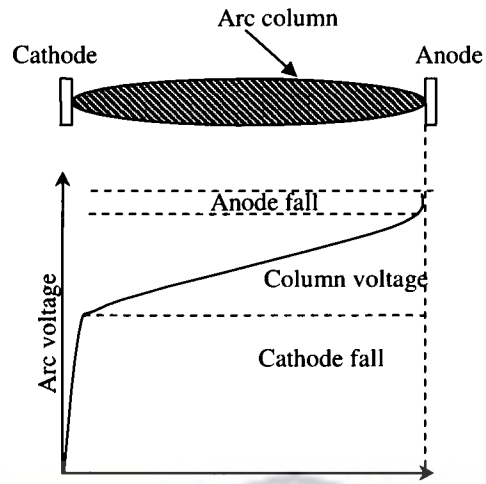

Figure 2-1 Arc voltage distribution (Ushio, 1988)

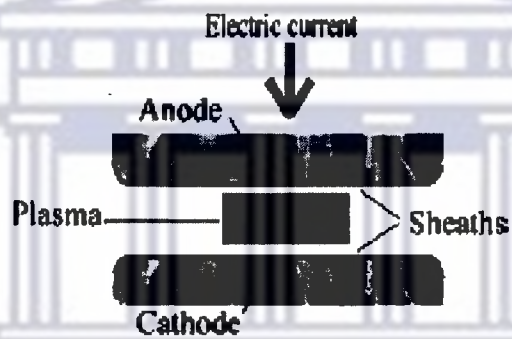

Figure 2-2 Arc discharge with evaporation electrodes: short arc (Djakov, 2000)

If a direct current is applied between two electrodes (a spark gap) in a gas it will illuminate the electrode with light and a photoelectric current will be formed at the cathode (Grove, 2000). As the two electrodes are moved closer together the current will become self-sustaining at a particular distance, without light, and this is known as Townsend discharge. During the Townsend discharge primary electrons produced by photon excitation generate more electrons by electron or neutron collisions. Research has shown (Grove, 2000) that secondary events such as ion impact on the cathode and the photoelectric effect of the photons generated in the discharge were large contributors to the formation of light. Secondary events at some points happen in sufficient numbers to secure the regeneration of the primary electrons.

The initial stage of breakdown between broad area electrodes involves field emissions from the cathode (Boxman, *et al.* 1995). These emissions arise from a highly localised site on the cathode and proceed as a beam to the anode where the anode metal is vaporised. The vapour ionizes while it is back streaming towards the cathode in the electron beam and forms a positive space charge near the cathode. The space charge enhances the cathode field and strengthens the emissions movement, causing breakdown of the gap.

Arcs are characterised by a collective electron emission mechanism from the cathode (Anders, 2006). There are two basic modes of collective electron emissions, thermionic and

explosive. In thermionic arcs, the most energetic electrons of the Fermi-Dirac distribution are able to overcome the potential barrier at the cathode surface, provided that the cathode has a high enough temperature. Emission of the electron is often assisted by the electric field that deforms the potential barrier. The current density is described by Richardson-Dushman equation

$$J = AT^2 \times 10^{\left(-\frac{\phi}{kT}\right)} \qquad 2.1$$

Where $A = A_o\lambda$ is the universal Richardson constant, A/(m^2.K^2)
λ is the material depending coefficient
$A_o = 1.2 \times 10^{\frac{6A}{(mK)^2}}$, A/(m^2.K^2)
ϕ is the work function (height of the potential barrier), eV
T is the cathode surface temperature, K
k is the Boltzmann's constant, eV/K

In the explosive events, a large number of electrons overcome the potential barrier. The cathode material in the area of the spot experiences phase transformation, which result in fully ionised and expanding plasma. Thermal conduction in the solid increases the active spot area and reduces the power density. The electrical conductivity below the spot is reduced at high temperature. Therefore a micro explosion destroys its own favourable conditions. A side effect of plasma formation is that the material between the dense plasma and colder electrode is in liquid form. This results in material being ejected as droplets or macrodroplets. The formation of such macroparticles is undesirable, and this is the major reason why arcing is of great concern to sputter deposition. The generation of macroparticle is observed to be less (Brown, *et al.* 1996) in cathode materials that have high melting point. There is also a natural way of separating the wanted plasma from unwanted macroparticle flux because the plasma is peaked in the direction normal to the cathode surface, while the macroparticle flux is peaked in a direction close to parallel (approximately 20°) to the cathode surface.

In case of both thermionic and cathodic arcs, large amounts of electrons are emitted. The emission is a result of the collective behaviour of many particles. In the case of cathodic arc there is a minimum chopping (cutting) current and a minimum localized action.

While the use of vacuum arcs has many advantages, the method also has disadvantages. One of the disadvantages is the occurrence of microdroplets in the plasma from which crystallisation takes place. The microdroplets of the cathode metal are melted and discharged from the cathode spot area and are deposited on the substrate surface. These particles take part in the coating of the substrates as well as ionized atoms. This increases the roughness of deposited coatings while at the same time worsening the homogeneity of substrate surface and chemical composition (Miernik, and Walkowicz, 2000).

2.3 Electrode system

For any given electrode geometry of a particular material there is a critical current I_{as} at which the anode spot will first appear. The value of I_{as} is the probabilistic threshold such that for a current I less than I_{as} an anode spot will never form. As the value of I approaches I_{as} value anode spot formation becomes more probable and when I is just above I_{as} the anode spot forms (Boxman, *et al.* 1995). The ion current I as a function of (bias voltage) V is determined by Langmur-Child formula

$$I = \frac{4\varepsilon_r}{9}\sqrt{\frac{2e}{m}}\sqrt[3]{V}\,\frac{A_s}{d^2} \qquad 2.2$$

Where ε_r is the dielectric constant, d is the distance between the electrodes and A_s is the surface area that emits ions of mass m (Hassan, *et al.* 2008). If both electrodes are of the same material the anode characteristics dominate. Materials with higher thermal characteristics $(K\rho C_h)^{1/2}$ have higher threshold currents for anode spot formation, as shown in table 2-1. The relationship between the critical current I_{as} and the thermal characteristic is

$$I_{as} = T_m \frac{\sqrt{K\rho C_h}}{F} \qquad 2.3$$

where $T_m(K\rho C_h)^{1/2}$ is the thermal characteristic, kg/s$^{5/2}$
T_m is the melting temperature, K
C_h is specific, J/(kg.K)
K is the thermal conductivity, W/(m.K)
ρ is the mean density, kg/mm^3
F is a parameter whose value depends upon the particular geometry and current waveform, kg/(s$^{5/2}$.A)

Table 2-1 Anode threshold current and threshold current densities (Boxman, *et al.* 1995)

Electrode material	I_{as} (kA)	J_{avc} (A/mm^2)	$T_m(K\rho C_h)^{1/2}$ (10^5kg/s$^{5/2}$)
S_n	2.3	0.9	53
Al	6.8	2.6	249
Ag	9.7	3.8	422
Cu	10.3	4	532
Mo	13.6	5.3	612
W	13.8	5.4	694

2.4 Cathode spots

A vacuum arc is characterised by arc spots on the cathode (Tekada, and Tekeuch, 2002). Cathode spots are a source of plasma which has an ionisation degree of 50-100% between the electrode gap (Fuchs, *et al.* 1998). The current is localised in these spots and each spot has a high energy density (Sugimoto, *et al.* 2004). During discharge one cathode spot splits and recombines many times so the number of these spots changes very quickly within a short time. The preferred direction of ion emission when using direct current source (also a known as continuous source) was found to be perpendicular to the plane of the cathode (Fuchs, *et al.* 1998). Continuous sources have high coating rates and the design of the cathode should allow it to dissipate the heat generated by the arc (Karpov, 1997).

When a higher current is used it leads to an increase in perpendicular ion emission and decreasing ion energies. At higher pulse current (pulse sources) ion energy also decreases and ion emissions increase. The arc duration is short enough in the case of pulsed source (Karpov, 1997) for cathode cooling to be unnecessary. In this case the confinement of the arc spot is also not important because the duration is short enough that there is not enough time

for the arc spot to move off the cathode surface. The total ion current ratio to the value of arc current is not dependent on the cathode material and it ranges from 8-12% (Fuchs, *et al.* 1998).

2.5 Atomic emission

Atomic emission is caused by the heat flux on the cathode which indicates a local vaporisation of the cathode (Zine, *et al.* 2005). When the surface of the cathode is in equilibrium with the surrounding vapour the emitted atom-flux is given by

$$\Gamma_n = n_o \sqrt{\frac{kT_s}{2\pi m_n}} \tag{2.4}$$

where k is the Boltzmann's constant, k = 1.38 x 10^{-23} J/K
T_s is the surface temperature, K
m_n is the mass of an atom, kg
n_o is the neutral density which is given by, kg/mm^3

$$n_o = \sqrt[3]{\frac{m_n kT_s}{2\pi\hbar^2}} \times 10^{\left(-\frac{W_{coh}}{kT_s}\right)} \tag{2.5}$$

with W_{coh} being the cohesion energy, eV

2.6 Emitted electrons

Electrons flow from the cathode wall (spots) (Messaad, *et al.* 2006) towards the plasma due to electron emission and thermal evaporation (Djakov, 2000). This electron flow is governed by the following surface conditions: wall temperature T_w, electric field E_w, and an electron work function φ_w. From these surface conditions the electron emission current density J_{ew}, the equilibrium vapour pressure p_{ow} and vapour flux Γ_{ow} are calculated.

$$J_{ew} = J_{ew}(E_w, T_w, \varphi_w) \tag{2.6}$$

$$\Gamma_{ow} = \frac{p_{ow}}{\sqrt{2\pi m k T_w}} \tag{2.7}$$

To maintain the electric arc discharge, a sufficient flux of electrons is needed, which is provided by the cathode (Meunier, and Coulombe, 1998). The electron beam is emitted from the cathode at the high surface temperatures. The ion flux bombarding the cathode surface maintains the electric field that forms the cathode sheath. The emitted electrons are accelerated through the sheath without collisions and when they reach the ionisation zone inelastic collision of electrons takes place, which leads to the production of ions. This phenomenon results in arc column formation between the two electrodes. The electron beam fraction left for ionization after inelastic collision is

$$f_{bi} = \frac{\nu_{bi}}{(\nu_{bi} + \nu_{be})} = \frac{\sigma_{bi}}{(\sigma_{bi} + \sigma_{be})} < 1 \tag{2.8}$$

where the i refers to ionization, e to excitation, ν indicates the frequency of each of the collision processes, σ the collision cross section and b the electron beam.

2.7 Ionic bombardment on the cathode

The ionic bombardment on the surface of the cathode is the energy flux of the ions colliding with the surface (Zine, *et al.* 2005) and is given by the ionic power density

$$P = e\phi_w + \frac{kT_e}{2} + \phi_i - \phi_s + \sqrt{\frac{e^3 E_s}{4\pi\varepsilon_0}} + W_{ev} \qquad 2.9$$

where e is the elementary charge
T_e is the temperature of an electron, K
ϕ_w is the cathode wall potential, eV
ϕ_i is the ion potential, eV
ϕ_s is the potential in the sheath, eV
ε_o is the permittivity constant, $C^2/(N.m^2)$
E_s is the energy of the ion, eV

2.8 Plasma ions

The ions from the plasma have a velocity corresponding to a kinetic energy of 19 to 150 eV depending to the material of the cathode. This energy is high enough so that ions can penetrate the surface of the substrate and come to rest under the surface. In addition to the kinetic energy of the ions gained at the cathode spot, ions are also accelerated in a thin space around the charge sheath when the substrate is biased (Anders, 2003). The average kinetic energy of the ions is given by

$$E_{kin}(Q) = E_{kin,0} + QeV_{sheath} \qquad 2.10$$

where Q is the charge state number
V_{sheath} is the voltage drop in the sheath, V
e is the electron charge, C

The accelerated ions not only bring kinetic energy to the substrate but also the potential energy. The sum of these kinetic and potential energies causes substrate heating by ion bombardment. The total energy of the ions arriving at the substrate is approximately

$$E(Q) \approx E_{kin}(Q) + \sum EQ \qquad 2.11$$

The summation symbol $\sum$ indicates that in the case of multiple charged ions the individual energies of ionization need to be added.

2.9 Role of cathode surface

The contamination of the surface layer and the use of non-metallic surface layers cause an important modification to the electron emission in arcs. The potential barrier from Fermi level to vacuum level is hidden by an additional potential structure as determined by the non-metallic or contaminant material. For arc discharges, the visibility and parameters of cathode spots depend on the presence of non-metallic and metallic layers.

There are two types of cathode spots, type 1 and type 2 and one can easily distinguish between the two (Anders, 2006). Type 1 cathode spots occur in the presence of non-metallic layers and type 2 burn on metal surfaces. Both types of cathode spots may appear in the same arc discharge, depending on the circumstances. Due to material erosion the arc may

initially exhibit type 1 spots and then undergo transition to type 2 spots. Type 1 spots produce small, separate craters (bowl-shaped cavity), have relatively low erosion rates and fast spot motion. The plasma contains metal and non-metallic species. Type 2 spots make chains of large craters. The spots move slowly and have a high erosion rate. The plasma contains ions of the cathode material with multiple charge states (Anders, 2006).

2.10 Anode electrode phenomena

The operation of the anode is either in a cold mode or in an evaporating mode, depending on the discharge and electrode conditions. The anode electrode also operates as the electron collector. The total energy transferred to the anode is

$$E_a = J(V_a + \Psi + \frac{5}{2}kT_e) + Q(R) + Q(h) \qquad 2.12$$

where J is the current density, A/mm^2
V_a the anode fall voltage, V
Ψ the work function of anode, eV
$(5kT_e/2)$ the electron enthalpy impinging to anode, eV
$Q(R)$ the net input by radiation, eV
$Q(h)$ the heat transferred by gas enthalpy flow, eV

The temperature of the anode rises to a steady state depending on the thermal properties and size of the anode as well as the current value. By increasing the current and decreasing the thermal diffusivity it is possible for the anode surface to reach evaporation point within a given duration (Ushio, 1988).

There are two common modes of anode operation. The first mode is a low current density mode where the anode acts only as an electron collector (and is essentially passive). The second mode is high current density mode with a fully developed anode spot. The two modes can be observed distinctively in the vacuum arc. The region of the anode has a steep temperature gradient which results in a thermodynamic state that is far from equilibrium. At the anode surface chemical reactions may also take place including ionisation, decomposition and recombination (Ushio, 1988).

2.11 Electric field and electric current

The electric field generated at each wall surface (Djokov, 2000) by the positive electric charge of the sheath is

$$E_w^2 = \frac{4}{\varepsilon_o}\sqrt{\frac{m_e U_w}{2e}}\left(J_{pw}\sqrt{\frac{m}{m_e}} - J_{ew}\right) \qquad 2.13$$

where U_w is the plasma-wall electric potential difference, V
J_{pw} is the ion current density at the wall, A/mm^2
m is the mass of the ion, kg
ε_o is the permittivity constant, C^2/(N.m^2)
J_{ew} is the emission current density, A/mm^2

The total electric current is the sum of all currents on the anode and cathode electrodes which is given by

$$I_t = \sum_{w'} I_{w'} = \sum_{w''} I_{w''} \qquad 2.14$$

where w' and w'' refer to the walls that serve as the anode and cathode respectively (Djokov, 2000).

2.12 Vacuum arc ion sources

Vacuum arc ion sources form high current beams of metal ions. The metal plasma from which the ion beam is formed is produced by the vacuum arc discharge. Vacuum arc ion sources are used for ion implantation in material surface modification research and for particle accelerator injection for fundamental nuclear physics research. They can deliver ion beams of nearly all solid conducting material (Anders, and Hollinger, 2001). Over 50 beams of ions of solid metal in the periodic table have been produced, with ion energies of several hundred keV and with beam current of several amperes (Brown, 2004).

The vacuum arc discharge provides a direct method of generating metal plasma and there is no need for additional gas (as in the case of sputtering). Vacuum arcs work in high vacuum for all metals. High density pure metal plasmas can be produced and high current pure metal ion beams can be formed. Ions are removed from the fast streaming, high density metal plasma that originates at cathode spots (Anders, and Hollinger, 2001). The maximum current of the ions that can be produced is determined by the beam formation system, not by the plasma. The individual ions produced are of low charge state and the charge state of ion beams lies between 1^+ and 3^+ depending on the metal species (Brown, 2004). Two types of vacuum arc ion source will now be discussed.

The first type discussed is the largest ion source available based on the metal vapour vacuum arc (Treglio, *et al.* 1997), and was designated the Metal Vapour Vacuum Arc IV (MEVVA IV) 80-50, by Lawrence Berkeley National Laboratory. It has ion sources that use up to 12 cathodes. The ability of this source to use many cathodes increases the operating time of the machine and allows multi-element implantations without breaking vacuum. This type of source is able to produce circular beams at a distance of 1000 mm from the source. Operating at an accelerating voltage of 80 kV and 50 mA power supply, the ion current typically of chromium ions is 25 mA. MEVVA ion source is also an attractive option for heavy ion fusion (HIF) (Anders, and Kwan, 2001) because it can produce ions of practically all conductive solids.

The second vacuum arc metal ion source discussed is referred to as the Advanced Vacuum Arc Ion Source (AVIS), and was developed for large industrial application. The source was mounted on a commercial implantation system and ran regularly at ion beam currents of 100 mA for more than 4 hours. In tests performed by Treglio (1997) the system was run continuously at 80 kV and over 75 mA average beam current for chromium ion implantation for a period of 24 hours without breaking vacuum. As shown schematically in figure 2.3, the ion source of the AVIS system comprises of an arc plasma source, the drift tube through which the metal plasma expands and drifts to the extraction area, and the ion extraction and acceleration system (Treglio, *et al.* 1997).

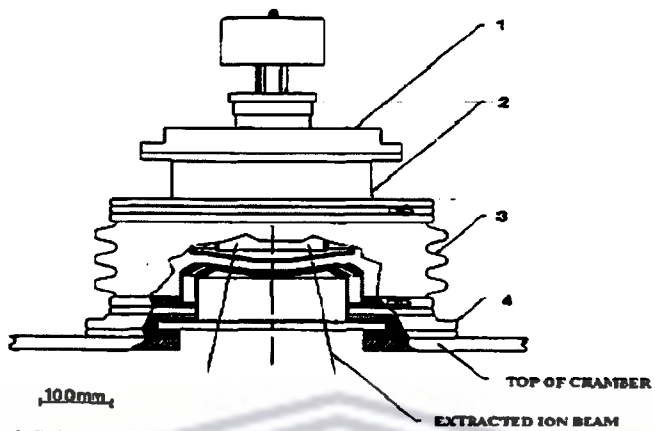

Figure 2-3 Schematic diagram of ion source assembly showing 1) Arc source with cathode drive 2) Drift tube 3) High voltage insulator assembly containing ion extraction system 4) Group cup assembly (Tregio, *et al* 1997)

2.13 Charge state enhancement

The ions that are produced in the vacuum arc plasma are multiply stripped of electrons and the ion charge state spectrum is distinct for different metals. The charge states produced range from 1+ to about 6+, with the mean charge state for a given metal in the range 1+ to 3+ as shown in Table 2-2.

Table 2-2 Charge state distribution and mean charge state, all in particles current fractions for range of metal ion species without a magnetic field (Brown, *et al.* 1996)

Metal	Without magnetic field					
	1+	2+	3+	4+	5+	$\bar{Q}$
C	96	4				1
Mg	51	49				1.5
Al	38	51	11			1.7
Ti	11	76	12	1		2
V	11	72	15	2		2.1
Cr	14	70	15	1		2
Fe	28	68	6			1.8
Ni	43	50	7			1.6
Co	34	59	7			1.8
Cu	28	53	18	1		1.9
Nb	3	40	39	16	2	2.7
Mo	7	30	40	20	3	2.8
Ag	13	61	25	1		1.9
Hf	7	26	48	18	1	2.8

The metals that have a low boiling point and are low in the periodic table have lower charge states, while metals that have a high boiling point and are higher in the periodic table have higher charge states. The ion energy can be increased by increasing the charge state rather than increasing the implanter operating voltage (Brown, *et al.* 1996). An empirical

expression that provide a reasonable prediction for the mean charge state (referred to as the distribution in particle current) is

$$\bar{Q} = 0.38\left(\frac{T_{BP}}{1000} + 1\right) \qquad 2.15$$

where T_{BP} is the boiling point of the metal in K (Brown, 1993)

2.14 Collisions with real atoms and ions

The collisions of particular interest in electrical discharges are between electrons, ions and atoms. In the case of electron-ion collision, the fields follow coulomb's law and the force between the particles varies as $1/r^2$ where r is the distance between the two particles. In the case of the electron-atom collision, the approaching electron produces a Coulomb field in the vicinity of the target atom, which polarizes the atoms. The resulting dipole produces a field which is proportional to the dipole moment, and varies as $1/r^3$. Thus the force on the oncoming electron varies as $1/r^5$. In both cases the test particle experiences deflection, even for a large impact parameter. The momentum transfer collision cross section is described as

$$\sigma_m = \int_0^{b_{max}} \frac{\Delta p 2\pi b}{p_0} d \qquad 2.16$$

where Δp is the change of momentum experienced by the test particles as the result of a collision with impact parameter b, and p_o is the initial momentum of the test particle. The maximum impact parameter at which the integral is terminated, b_{max} would be infinite in the case of a single ion target and would still lead to an infinite electron-ion cross section (Boxman, *et al.* 1995).

2.15 Low-voltage vacuum-arc discharge

Low-voltage discharge is produced by separating electrodes which were initially in contact. One of the electrodes contains the material of interest. During the mechanical separation the contact area (between the electrodes) decreases and the resistance of the interface increases, leading to a localized heating of a small volume of the material. The temperature of the material rises to a high value which causes the electrodes to vaporize. As the separation distance is increased, and the resistance increases the potential difference also increase across the vapour, producing a highly ionized plasma. The discharge can sustain itself for a longer period if the correct conditions prevail (as discussed in Section 2.2). Such discharges produce ions with a single charge (Dunning, *et al.* 1995).

2.16 High-voltage vacuum-arc discharge

Applying a voltage which exceeds the vacuum breakdown voltage across the gap that separates the electrodes initiates the high-voltage discharge. Initiating and sustaining the high-voltage discharge is complex, as no comprehensive theoretical basis for the breakdown vacuum arc discharge has been formulated. The initiation mechanism can be explained in terms of field emission theory. The current density from a field emitting tip as a function of electric field at the tip is given by the Fowler-Nordheim equation

$$J = \frac{1.54 \times 10^{-2} E^2}{\Psi t^2(y)} exp\left(\frac{9\Psi^{\frac{3}{2}}}{E}\right) \frac{A}{m^2} \qquad 2.17$$

$$y = \frac{3.795 \times 10^{-2}\sqrt{E}}{\Psi}$$

where J is the current density, E is the electric field strength and Ψ is the work function of the metal. The expressions $v(y)$ and $t(y)$ are slowly varying, tabulated functions of the work function and electric field and are usually regarded as constant (Dunning, *et al.* 1995).

Chapter 3

3 DEFLECTION AND DEPOSITION OF CHARGED PARTICLES

3.1 Introduction

The previous chapter discusses the generation of ions and the mechanisms by which the generation is achieved. This chapter focuses on extraction, acceleration, deflection and deposition of ions. The concept used to accelerate ions is similar to the accelerator method used in electrostatic thrusters. In electrostatic thrusters the ion accelerator consists of electrically biased multi-aperture grids and this assembly is often called the ion optics. For this application the optics are made of two collimators and a target plate. The first collimator acts as an extractor and the second collimator accelerates the extracted ions. Both these collimators are held at different potentials (Claypool, 2007). The first collimator is held at a potential that is half that of the accelerator collimator. The target plate is held at a potential that is higher than that of the first and second collimator to further accelerate and attract the ion beam. Between the second collimator and the target plate are deflector plates held at a certain potential difference to allow a uniform electric field to be formed and deflection of the accelerated ion beam to occur.

3.2 Physics of charged particles

Three types of particles play a role in ion propulsion system operation, namely neutral atoms, ions and electrons. The focus of this research is on ions. The movement of particles is influenced by the external forces that are applied to them as defined by Newton's second law

$$\boldsymbol{F} = m\boldsymbol{a} \tag{3.1}$$

The predominant force operating on charged particles in this case is the electric force from the electric field generated by all charges (Claypool, 2007). The forces occurring between these charged particles are defined by Coulomb's Law (Young, and Freeman, 1996) which is expressed as

$$F = k_C \frac{|q_1||q_2|}{r^2} \tag{3.2}$$

Where k_C is Coulomb's constant, 8.988 x 10^9 $(N.m^2)/C^2$
q_1 and q_2 are the charges of particles 1 and 2, C
r is the distance between the two particles, m

Coulomb's law gives rise to the concept of electric field which is defined as

$$E = \frac{F}{q} = k_C \frac{Q_s}{r^2} \tag{3.3}$$

where E is the magnitude of the electric field, V/m
Q_s is the charge of the source particle, C

When charged particles enter the region of the electric field they are accelerated by a force proportional to the product of the electric field and the charge of the particle (Claypool,

When charged particles enter the region of the electric field they are accelerated by a force proportional to the product of the electric field and the charge of the particle (Claypool, 2007). The direction of the resultant force is determined by the direction of the electric field in the region of the electric field. This force vector is given by

$$\boldsymbol{F} = q\boldsymbol{E} \qquad 3.4$$

where $\boldsymbol{E}$ is the magnitude and direction of the electric field
q is the charge of the particle

3.3 Extraction and acceleration of ions from plasma

The collimator extracts the ions from the discharge plasma, focusing them into a collimated ion beam. This focusing is accomplished by the small single opening on each collimator that allows the beam to pass through. Unlike the collimators, the accelerator grids in ion thrusters have many small openings (Cassy, *et al.* 2008). This minimizes ion impingement on the screen grid because the screen grid transparency has an impact on the discharge loss. The maximum number of ions that are delivered by the plasma discharge to the screen grid surface must be extracted by the accelerator grids as show in Figure 3-1 to minimize ion impingement on the screen grid (Goebel, and Kats, 2008). For this work shielding of the plasma is crucial to enhance the collimated beam, as shown in Figure 3-2.

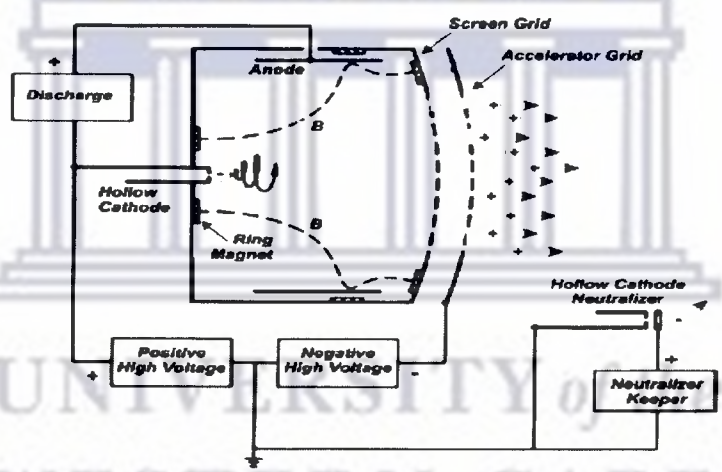

Figure 3-1 Ion thrusters showing acceleration grid (Cassy, *et al.* 2008)

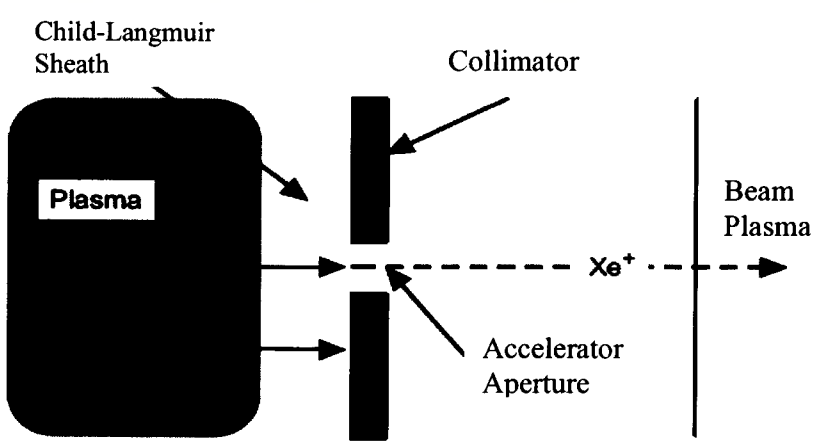

Figure 3-2 Shows the accelerator aperture in contact with a plasma (Goebel, and Kats, 2008)

To accelerate ions a potential difference should be established between the plasma and a collimator/accelerator grid (Goebel, and Kats, 2008). If the potential is small compared to the electron temperature T_e a Debye sheath is formed and if the potential is very large compared to T_e then a Child-Langmuir sheath will form. To accelerate ions to high energy it is necessary to establish a sheath that will accelerate ions and reflect electrons from the plasma. In order to do this the dimensions of the aperture at the plasma boundary must be reduced to the order of the Child-Langmuir distance as shown in Figure 3.3.

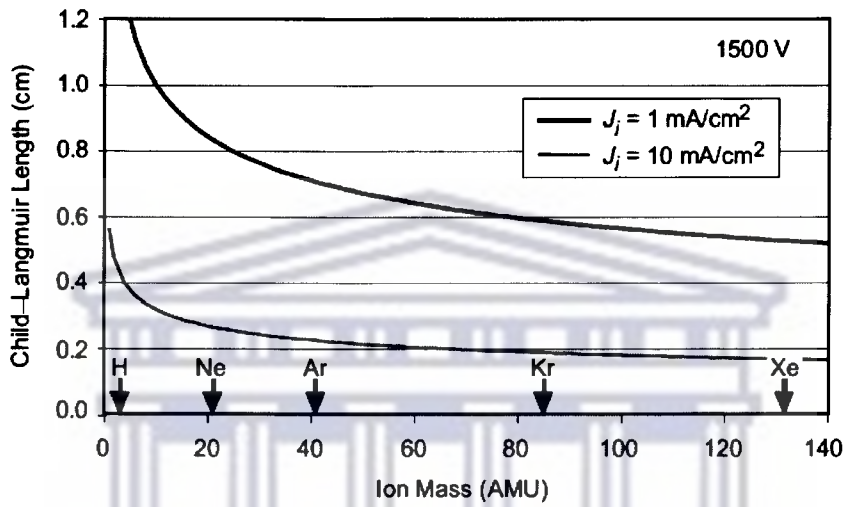

Figure 3-3 Child-Langmuir sheath Length versus ion mass for two ion current densities at 1500 V acceleration voltage (Goebel, and Kats, 2008)

3.4 Deflection of ions by uniform electric field

The generated ions are extracted by the collimator and enter the region of uniform electric field. In this region they experience a transverse deflection in the y-axis and are collected on the target as shown in the figure below (Young, and Freeman, 1996). Figure 3.3 shows the path of the ion from where it is born to where it is collected on the target.

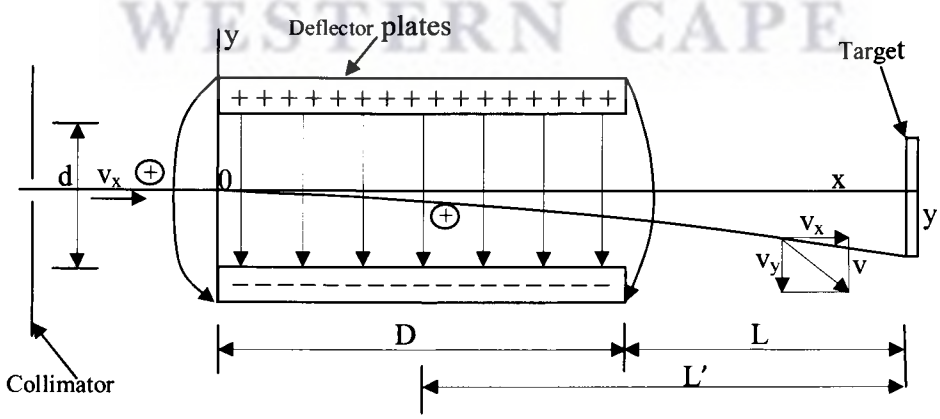

Figure 3-4 Deflection of silver ions in a uniform electric field (Young, and Freeman, 1996)

$$E_{kin} = \frac{mv_x^2}{2} = eV \quad 3.5$$

Where e is the elementary charge of the silver ion
The longitudinal velocity v_x of the beam is thus

$$v_x = \sqrt{\frac{2eV}{m}} \quad 3.6$$

Considering ions with velocity v_x which enter a region of uniform transverse field E, the transverse force on an ion is eE. This force produces a transverse acceleration a_y whose magnitude is given by Newton's law of motion

$$ma_y = eE \quad 3.7$$

Acceleration lasts for a time t equal to the time spent in the field of

$$t = \frac{D}{v_x} \quad 3.8$$

where D is the length of the deflection region. The acquired transverse velocity is therefore

$$v_y = a_y t = \frac{eED}{mv_x} \quad 3.9$$

The ion travels with uniform velocity and takes an additional time L/v_x to reach the target where L is the longitudinal distance travelled. The ion undergoes a displacement y, given by

$$y = \frac{Lv_y}{v_x} \quad 3.10$$

Substituting for v_y from equation 3.9 into equation 3.10 gives

$$y = \frac{L\,eE\,D}{v_x m v_x} \quad 3.11$$

Substituting for v_x from equation 3.6 into equation 3.11 gives

$$y = \frac{L\,D\,E}{2V} \quad 3.12$$

Electric field is determined by the potential difference V_x between the plates and the plate separation distance d and is given by

$$E = \frac{V_x}{d} \quad 3.13$$

Substituting equation E as given by equation 3.13 into equation 3.12 gives

$$y = \frac{LDV_x}{2dV} \quad 3.14$$

This is the transverse deflection which occurs after the ion leaves the deflection region. It can be shown that equation 3.14 gives total deflection y', if L is replaced by L', the distance from the middle of the deflection region to the target which is given by

$$y' = \frac{L'DV_x}{2dV} \quad 3.15$$

3.5 Electric field computation for an non-uniform field

Charge density σ can be described in terms of the potential that, in the absence of an external source charge, satisfies the Laplace equation (Pham, 1998). Steady state distribution of electrical potential $V(x, y)$ (Kalenderli, *et al.* 2004) in a two dimensional plane is given by

$$\nabla^2 V(x,y) = \frac{\partial^2 V(x,y)}{\partial x^2} + \frac{\partial^2 V(x,y)}{\partial y^2} = 0 \quad 3.16$$

Equation 3.16 can be discretized into two-dimensional Cartesian coordinates with equal sized grids using first order central difference, benefiting from a Taylor series as follows

$$\frac{\partial^2 V(x,y)}{\partial x^2} = \frac{V(x+h,y) - 2V(x-h,y) + V(x,y)}{h^2} \quad 3.17$$

$$\frac{\partial^2 V(x,y)}{\partial y^2} = \frac{V(x,y+h) - 2V(x,y-h) + V(x,y)}{h^2} \quad 3.18$$

where h is the separation distance of the grid points

From equation 3.17 and 3.18 and placing $V(x,y)$ as the subject of the formula gives

$$V(x,y) = \frac{[V(x+h,y) + V(x-h,y) + V(x,y+h) + V(x,y-h)]}{4} \quad 3.19$$

Equation 3.19 is used for all grid points and which results in a number of linear equations equal to the number of grid points. The potential for each point between the plate boundary conditions needs to be determined. The Laplace equation, together with the boundary conditions, can be solved using finite difference or finite element methods (Pham, 1998).

3.6 Ion deposition

Vacuum arc deposition is a process that uses a cathode vapour plasma produced from a high current discharge to form a highly ionized plasma. Vacuum arc deposition is conducted with an arc running in a cathode spot mode, with the cathode spot plasma jets impinging on a substrate located relatively far from the cathode (Boxman, 2001). The object onto which the ions are to be implanted is immersed in a plasma of the desired ion species. At the plasma-substrate the plasma sheath forms and ions are accelerated through the sheath and into the substrate. The ions accelerated towards the substrate suffer collisions with previously-deposited metal atoms and thus experience recoil implantation (Brown, 2001). The substrate is not only bombarded by energetic ions, it is also bombarded by energetic electrons from the plasma. The energy and velocity of these electrons is higher than that of ions, thus the substrate will acquire a negative potential with respect to the plasma. The current density of

the electrons and ions at the edge of the plasma sheath is given by the thermal velocity inside the plasma and plasma density n_o (Bartzsch, *et al.* 2000). The ion current density is given by

$$J_i = 0.6 n_0 \sqrt{\frac{kT_e}{m_i}} \qquad 3.20$$

where T_e is the electron temperature, K
m_i is the mass of the ion, kg
n_o is the plasma density, (A.s)/mm^3

The current of electrons at the substrate that overcome the repulsive potential U_p - U_{fl} is expressed by

$$I_e = \frac{1}{4} n_0 \sqrt{\frac{8kT_e}{m_i}} \, exp\left(-\frac{e(U_p - U_{fl})}{kT_e}\right) \qquad 3.21$$

where m_e is the mass of an electron, kg
U_p is the plasma potential, V
U_{fl} is the floating substrate potential, V

3.7 Effects of ion bombardment on the substrate

When coating the substrate, the process conditions (arc power, gas pressure, distance between target and ion source) should be kept constant. Factors that have an impact on the substrate are ion bombardment, heat radiation, heat convection, heat released by vapour deposition and by chemical reaction and the energy of back-sputtering particles from the substrate surface. During deposition a substrate is covered by plasma and there is a potential difference between the substrate and the plasma which is given by (Guoqiang, *et al.* 2005)

$$U = U_{pl} + |U_{dc}| \qquad 3.23$$

Where U is the total voltage between the substrate and the plasma, V
U_{pl} is the plasma sheath potential, V
U_{dc} is the bias voltage provided by the normal dc bias power, V

The substrate current density is given by

$$J = \frac{I_s}{A} \qquad 3.24$$

where I_s is substrate current, A
A is the substrate surface area, mm^2

The power density of the ion bombardment is given by

$$P_b = UJ \qquad 3.25$$

The effective parameter leading to ion bombardment is the kinetic energy of the ions at which they are emitted from the arc source. This energy is equivalent to the energy gained by the

ions passing through an electric field. In any plasma a substrate always possesses a positive space charge U_{pl} which attracts and accelerates the ions towards it during deposition.

3.8 Heat radiation and heat conductivity of substrate

The heat radiation power density at a substrate with temperature T_{st} is given by (Guoqiang, *et al.* 2005)

$$P_d = \xi\varepsilon\sigma\,(T_{st}^4 - T_o^4) \tag{3.26}$$

and the heat conductivity power density is given by

$$P_c = \frac{k_h}{B\Delta x}\,(T_{st} - T_o) \tag{3.27}$$

Where ξ is an area factor related with the distribution of plasma and shape of substrate, mm^{-2}
ε is the emission coefficient of the substrate
σ is the Stefan constant, $W/(m^2.K^4)$
T_{st} is the substrate temperature, K
T_o is the environmental temperature, K
k_h is the coefficient of heat conductivity, W/(m.K)
B is factor related with area, equivalent to the ratio of cross section area of the axis
Δx is the length of the axis which heat is conducted, mm

Chapter 4

4 EXPERIMENTAL WORK

Experimental work was performed in order to study the generation, deflection and collection of silver ions using different geometries of the ion source and different power supplies. This chapter explains the experimental design, setup and test procedures. All the experiments were performed in a specially manufactured cylindrical vacuum chamber in the Mechanical Engineering Laboratory of the Department of Mechanical and Mechatronic Engineering, University of Stellenbosch.

4.1 General components of the experimental set-up

The experimental set-up consists of a glass cylinder, base plate, top plate, ion generation unit, collimators, deflector plates, non-conducting column, glass target and voltage supply loads are shown schematically in figure 4-1. The complete experimental setup including vacuum system and power supplies is shown in figure 4-2.

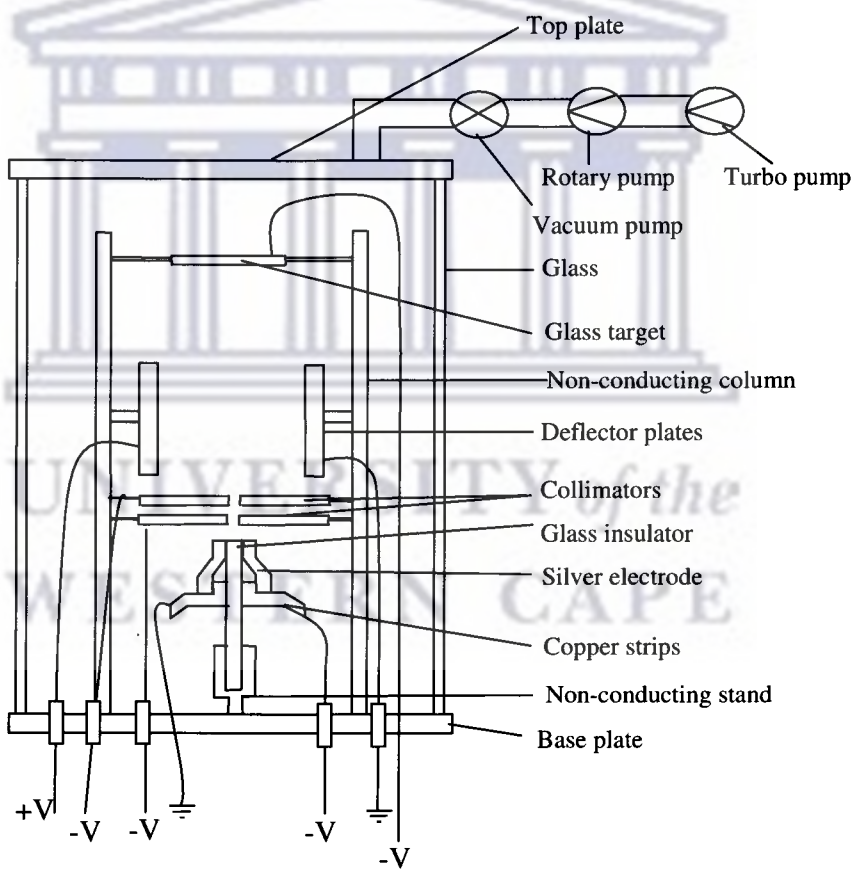

Figure 4-1 Schematic of the experimental set-up

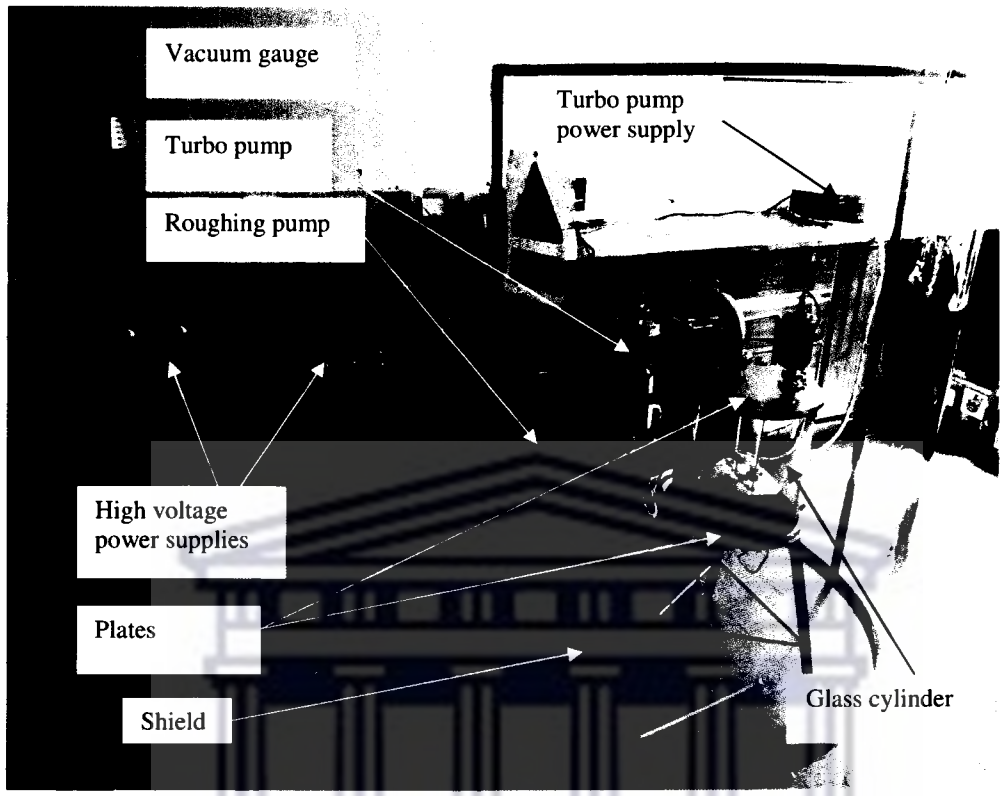

Figure 4-2 Complete experimental set-up

4.1.1 Glass cylinder

The glass cylinder plays a very important role in the experimental set-up as it allows a vacuum to be formed. The edges of the glass cylinder are covered by a rubber seal which also allows vacuum to be formed. The glass cylinder has an inner diameter of 202 mm, outer diameter of 206 mm and a length of 300 mm. It also allows the internal components to be observed during the experiment.

4.1.2 Plates

Plates are positioned at the top and bottom of the glass cylinder. They seal the cylinder after every component of the system shown in figure 4-1 has been placed in its position. The base plate on the bottom of the cylinder has small openings for the spark plugs which provide connections from the power supplies to the ion source, collimator, deflector plates and target. The plate on top has a large opening through which vacuum is drawn.

4.1.3 Shield

The shield is half-cylindrical in shape and acts as a covering for the experimental set-up to protect the personnel from high voltage cables connected to the bottom base plate. The shield also has the important function of stopping broken glass if the glass cylinder implodes during or after drawing the vacuum.

4.1.4 Roughing pump and vacuum gauge

The roughing pump (Leroy Somer, 909190-2000) is switched on first to draw vacuum because it operates at atmospheric pressure. In the experiments it drew pressure from 20 to

0.09 mbar. The turbo pump was then switched on. The vacuum gauge (Balzers, 265778) shows vacuum pressure as the two pumps draw vacuum.

4.1.5 Turbo pump

The turbo pump (Leybold-Heraeus, 0487470012) was switched on when vacuum pressure reached 0.09 mbar and it drew vacuum to 1.3×10^{-5} mbar. The turbo pump plays a very important role because if the vacuum is not high enough a corona forms during the experiment.

4.1.6 Power supplies

Power supplies provided the necessary voltages to the ion source, collimator, deflector plates and target. These voltages allowed the objectives of this study to be met. Before switching on the power supplies during the experiments, safety procedures were followed as described in Appendix C.

4.2 First design of the experimental setup

Figure 4-3 shows the preliminary design of the Ion Generation, Deflection and Deposition in Vacuum, (IGDDV). Different ion sources and power supplies were tested for the design. The silver electrodes represent the ion source. Two collimators have been used in this design, the first collimator extract and accelerate the silver ion beam after it has been produced from the ion source. The second collimator accelerates the beam further to enter the deflection region created by the deflector plates as shown in figure 4-3. The collimators in this design are less broad than the collimator used in the final design shown in figure 4-13 and this led to less shielding of the silver ion beam.

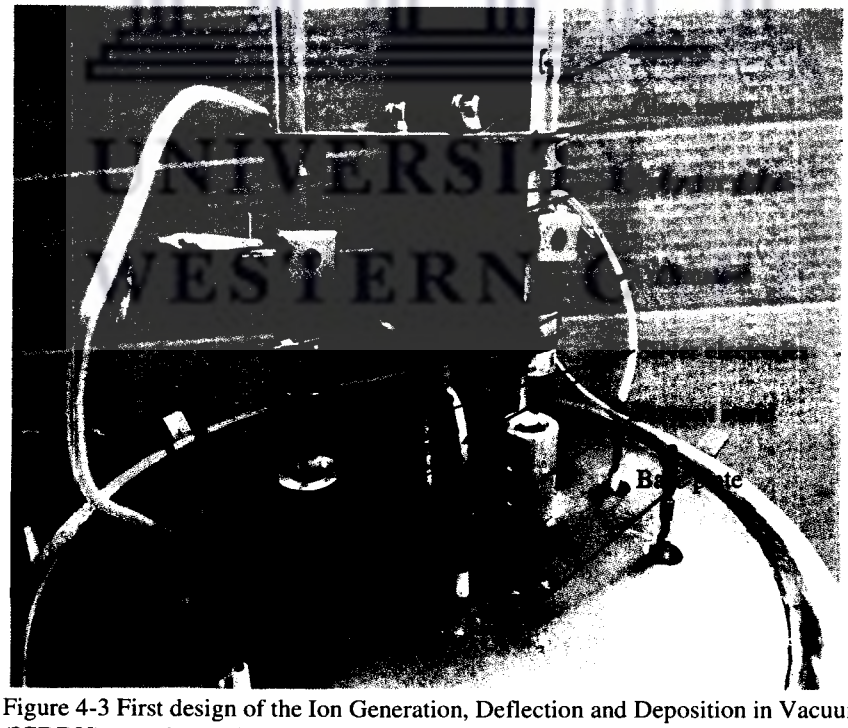

Figure 4-3 First design of the Ion Generation, Deflection and Deposition in Vacuum (IGDDV) experimental set-up

4.2.1 The preliminary design of the power supply

Figure 4-4 shows a power supply with a positive output range of 1 to 10 kV. This supply was used to generate silver ions from the ion source with ion energies ranging from 1 to 10 keV.

Figure 4-4 High voltage power supply

4.2.2 Principle of a power supply circuit

The circuit diagram for the power supply is shown in figure 4-5. The step-down transformer lowers the voltage from 220 V_{AC} to 15 V_{rms} and the bridge rectifier converts the alternating current to direct current. The capacitor next to the bridge rectifier smoothes the output of the bridge rectifier after it has been converted from ac to dc. The LM338 mosfet with the two resistors and the two capacitors forms a circuit that controls the power delivered to the fly-back transformer. The LM338 supplies a current over a 1.2 V to 32 V output range.

The LM555 semiconductor with a capacitor and two resistors forms a timing circuit that switches the LM338 mosfet at 20 kHz so that the fly-back transformer operates at that frequency. The LM555 produces timing pulses and the delayed time is controlled by the resistor and the capacitor (6.2 nF) next to the LM555. The frequency at which the fly-back transformer operates is controlled by the two resistors and the capacitor. The high voltage capacitor (3 kV, 0.15 μF) charges up and as soon as the breakdown voltage occurs in the electrode gap it discharges, producing high current.

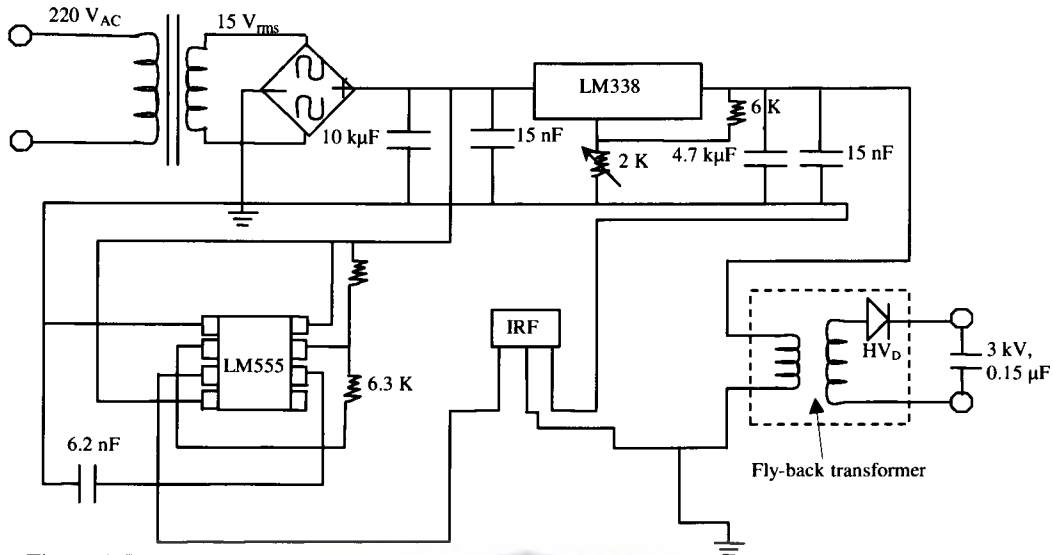

Figure 4-5 Power supply circuit diagram

4.3 First design of the ion source

Figure 4-6 shows the first ion source used to produce silver ions and section 4.3.1 gives a description of this ion source.

4.3.1 Description of the first design of the ion source

In the first design the two silver electrodes are separated by a 1 mm glass slide which acts as an insulator, as shown in figure 4-6(a). One electrode is earthed and the other electrode has a positive potential. When the arcing power supply is switched on arcing takes place as shown in figure 4-6(b). Positive ions are produced and accelerated towards the collimator that has a negative potential. This design of the ion source was very sensitive and the glass insulator would crack while the experiment was running. This caused arcing to take place through the crack and made it necessary to continuously make new ion sources for this design. However, several tests were performed using this ion source design and the results are shown in section 4.3.2

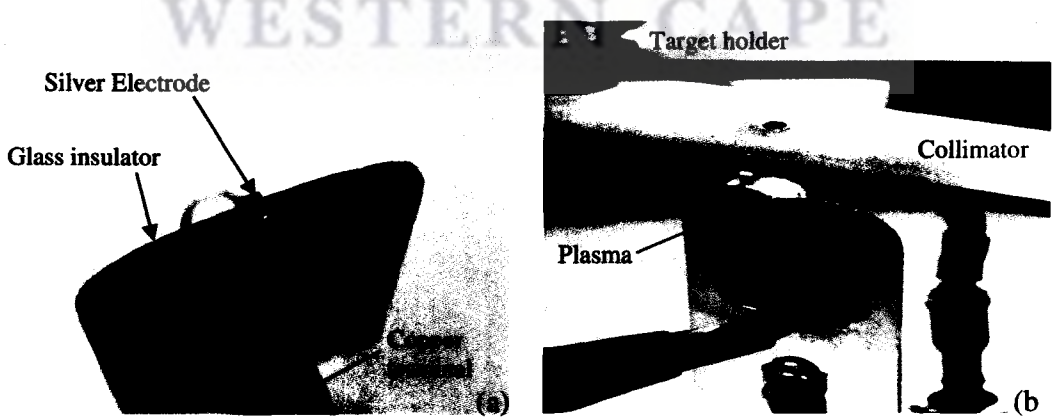

Figure 4-6 Photograph of the ion source (a) Shows the generation of silver ions (b)

4.3.2 Results and discussion of the first ion source

Figure 4-7 shows the results obtained during the testing of the first ion source design. The circles around the opening of the collimator support stand show the distribution of silver particles that deposited during the experiment.

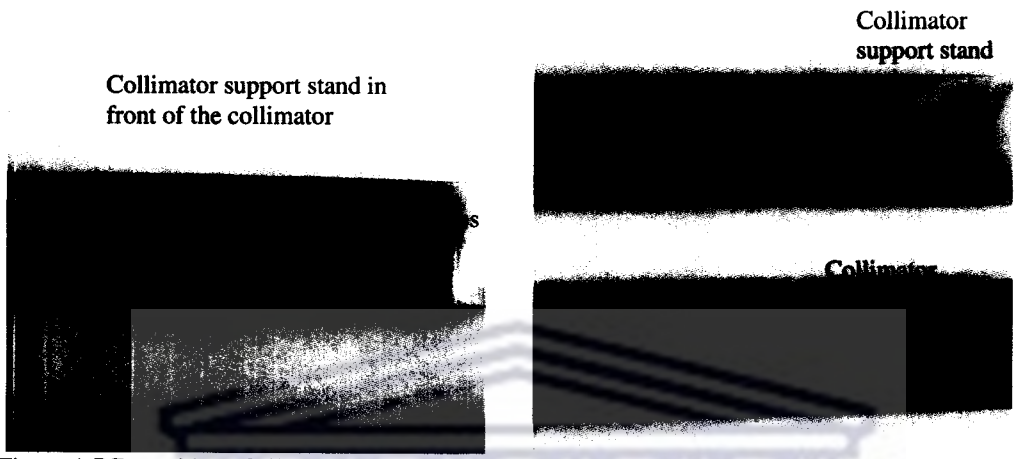

Figure 4-7 Deposition of silver particles on the collimator and collimator support stand

4.3.3 Results and discussion of the first ion source

Deposition of silver particles as well as etching marks/spots are also clear on the collimator. Etching spots were expected because of the energetic silver particles that were travelling at high speed. The energy of these particles ranged between 1 to 10 keV. The arcing voltage was not kept constant during the experiment because the power supply used was a DC high voltage supply and arcing would stop from time to time. When this occurred the voltage was increased to re-initiate the arc. However no silver particles were collected on the glass target. This is attributed to the sensitivity of the ion source which prevented the experiment from running for a long enough time to allow the deposition of silver on the glass target.

4.4 Second design of the ion source

The first ion source discussed in section 4.3.1 gave problems. To overcome these problems a second ion source was made.

4.4.1 Description of the second ion source

The second design for the ion source, shown in figure 4-8 consisted of a 3 mm diameter grounded silver electrode and a concentric outer sheet of silver electrode covering the glass insulator. The outer electrode had a positive potential and this connection led to silver particles being generated on this electrode. During the experiment the glass insulator expanded and cracked due to the high voltage. Constructing more of these ion sources was hindered by the 3.1 mm diameter glass tube, which broke easily during the assembly of the ion source. The same power supply shown in figure 3-4 was used to generate the ions and again consistent pulses were difficult to maintain. When arcing stopped the power supply was switched off and then on again and the voltage was increased. This would initiate an arc but did not sustain it. The power supply also over-heated during the experiment and so could not run for a long time.

Figure 4-8 (a) Second design of the ion source (b) Formation of plasma

4.4.2 Results and discussion of the second design

The (yellowish) brown colour on the collimator shown in figure 4-9 indicates the deposition of silver particles. From this result it is observed that the experiment did not run for an appreciable amount of time due to the sensitivity of the ion source and power supply as compared to results shown in figure 4-7. This is seen because of the less colouration of the silver deposits on the collimator (0.45 mm thick) and collimator stand (0.8 mm thick).

Figure 4-9 Deposition of silver ions on the collimator and its support stand

4.5 Third design of the ion source

A high voltage ion source that operates from 0 to -20 kV is shown in figure 4.10 (a)-(c).

4.5.1 Description of the third ion source

The third design of the ion source consisted of two silver electrodes with flat surfaces at the end of the electrodes, as shown in Figure 4-10 (a). For this ion source plasma could not form using the first design of the power supply (shown in figure 4-4). A high voltage Heinzinger HNCs 40 kV/-15 mA was used instead, because it can deliver very high voltages and an arc was easily initiated. When running the experiment an arc would form between the electrodes with one electrode at ground potential and the other electrode at -20 kV. The pulses of the

power supply were however not consistent and the time difference between the pulses varied which caused the experiment to run for a longer time.

Figure 4-10 Two silver rods with 1 mm separation distance (a), Corona forming (b) and Machined silver electrodes (c).

At the beginning of the experiment the pulses seemed continuous but as the experiment continued they stopped. Different approaches were undertaken to solve the problem, the first approach was to start the experiment at atmospheric pressure. As the experiment progressed the pulses seemed consistent and when the pressure reached 14 mbar a corona (arc discharge) formed. At 1.33 x 10^{-4} mbar the corona stopped. This approach did not work because arcing would not re-initiate after the corona had stopped. The second approach was to machine the spark plug threads down, just below the base plate as shown in figure 4.13. This approach helped to stop the corona formation but did not help to sustain an arc. The third approach was to machine the silver electrodes at the tip so as to force an arc to form, as shown in figure 4-10 (c). This approach helped to sustain an arc in high vacuum (1.33 x 10^{-5} mbar). The machined silver electrodes had a rough surface at the tip which contributed to sustaining the arc. The rough surface was made by a drill (Dremel 300 F013 0300 45 roughing bit) during machining of the electrodes. The machined electrodes could easily be placed at separation distances of less than 1 mm. The smaller gap also contributed to sustaining an arc.

However running the experiment for a long time interfered with the electronics of the turbo pump. Several measures were undertaken to prevent this interference but were not

successful. The methods investigated included a) placing the power supply of the turbo pump far away from the experiment so that electromagnetic waves produced during arcing would not interfere with the power supply of the turbo pump, (b) covering the glass cylinder of the experimental set-up with aluminium foil to stop the electromagnetic waves and (c) cover the cable of the power supply that runs from the power supply to the turbo pump with aluminium foil. None helped. This ion source was therefore discontinued because it required very high voltage and caused the safety interlock in the electronic controller to switch the power to the turbo pump off.

4.5.2 Results and discussion of the third ion source

From the experimental results obtained from the third ion source as shown in figure 4-11(a)-(d), it was observed that more uncharged particles were produced than charged particles. The production of uncharged particles can be attributed to arcing, extraction, acceleration and deflection voltages used which were -20 kV, -2.5 kV, -3 kV and 1 kV respectively. When arcing with -20 kV and extracting with -2.5 kV, the only ions that were extracted from the plasma were the ions that were born between the potential of 0 to -2.5 kV because of the restriction on the extraction potential. The ions that were formed at potential greater that -2.5 kV were not extracted by the collimator. Instead these ions were attracted by the strong negative charge of the electrode relative to the collimator.

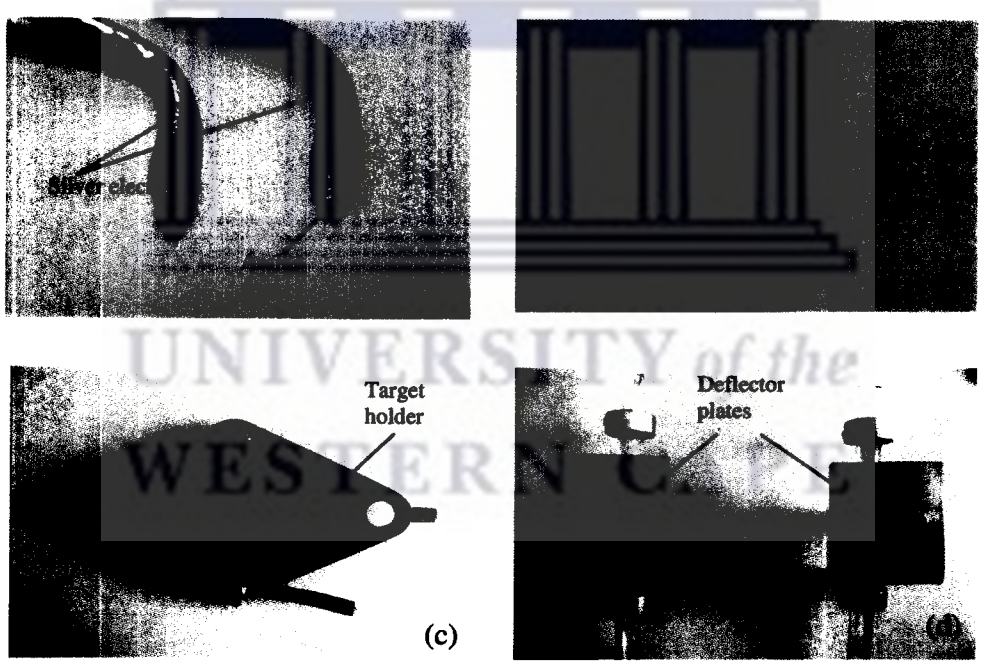

Figure 4-11 Silver electrodes (a), Deposition of silver particles on glass target (b), Deposition of silver particles on target holder (c), and Deposition of silver particles on deflection plates, deflector plate on the left was on positive potential and the one on the right was at ground potential (d).

It was observed that more particles deposited on the deflector plate that was at ground potential compared to the one at the positive potential (1 kV) as shown in figure 4-11(d). This shows that not only neutral particles but also charged particles deposited on the grounded deflector plate. Only a few particles deposited on the glass target compared to the target holder. This was caused by the charge induced on the glass target by the ions. As the ions deposited on the glass target the glass was charged to the same potential as that of the

accelerated ions. This caused repulsion of ions as more ions were accelerated to the glass target, hence more particles deposited on the target holder as shown in figure 4-11(c).

4.6 The final design of the ion source

The final design of the ion source is similar to the second design of the ion source, but with a different insulator material. The two electrodes are separated by a Teflon sleeve as shown in figure 4-12(a). The voltage connection was also different for this ion source. The central electrode had a positive potential (2 kV) and the outer sheet (electrode) was grounded. Ions were formed from the central electrode and accelerated upwards due to the positive charge on the positive electrode and the extraction voltage (-3 kV) of the collimator, as shown in figure 4-12(b).

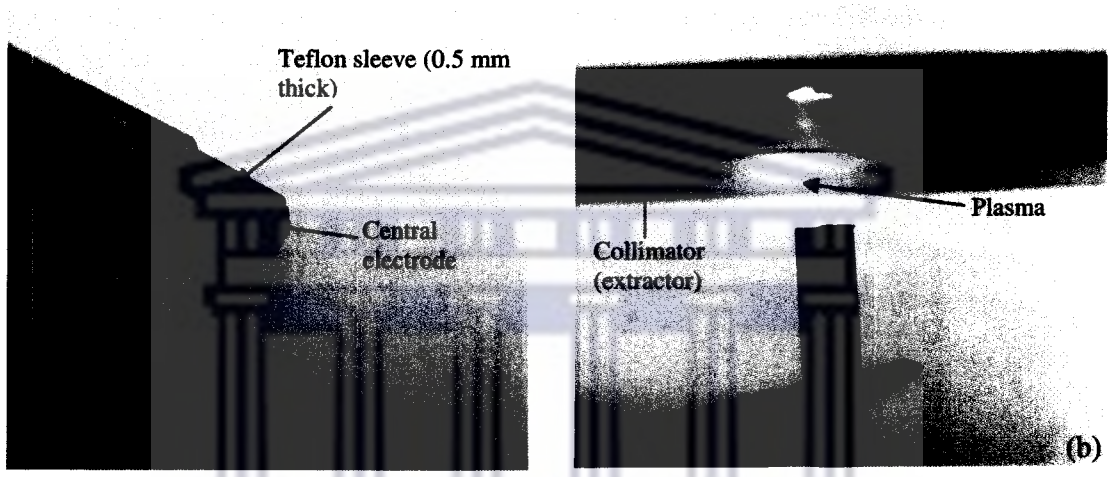

Figure 4-12 Ion source (a) Plasma formation from the ion source (b)

4.7 The final design of the IGDDV

Figure 4-13 shows an improved design of a IGDDV. A few changes were made for this design of the experimental set-up to improve the results. A wider and broader collimator (168 x 167 mm, 0.52 mm thick) compared to collimators used in the first design of IGDDV is used to shield part of the silver beam. This prevented silver by-passing the collimator and plating on the experimental components. The small collimator on top of the broader collimator has a small diameter hole to collimate the beam. The target holder was changed from a conducting to an insulating material to prevent the deposition of silver particles on it. In this set-up the glass target was covered with aluminium foil so that all charged particles are accelerated to the target. This IGDDV worked well and hence is called the "final" design.

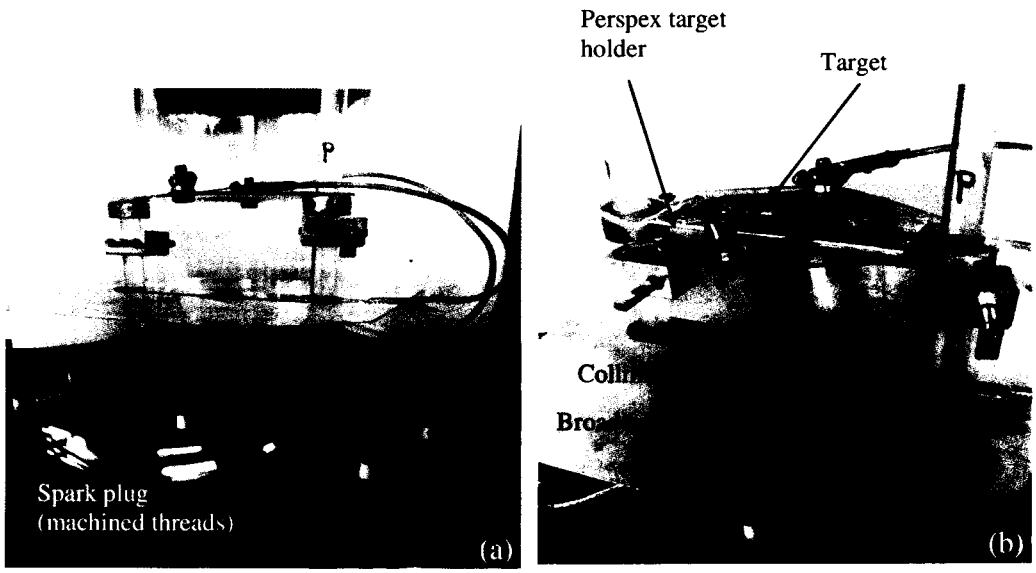

Figure 4-13 Side view of final design of the IGDDV (b) and The broader collimator (b)

4.7.1 Extraction, deflection and deposition of ions

Figure 4-14(a)-(c) give an idea of the processes experienced by the extracted and accelerated ions during the experiment. The formation of the corona at low vacuum is shown. In figure 4-14(a) the collimator and the target were at the same potential (-3 kV), so that the ions would drift at constant speed to the target after passing through the collimator. In figure 4-13(b) only the deflection voltage (-1 kV) was switched on. The deflector plate on the right was connected to -1 kV and the one on the left was grounded. The corona represents the potential between the two deflector plates. As the corona moves to the grounded deflector plate its intensity decreases, showing that the potential also decreases. The corona is approximately zero on the grounded electrode. Figure 4-13(c) shows the result when both extraction and deflection voltages were switched on. From this result it was clear that both voltages have c together. These pictures were taken at a pressure of 6.65 x 10^{-3} mbar.

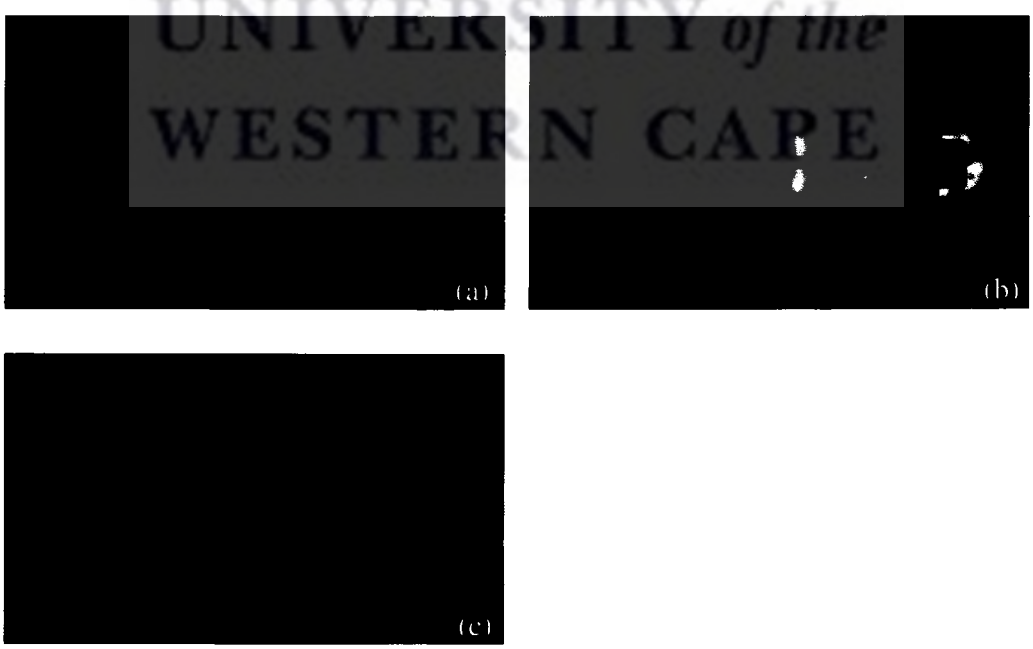

Figure 4-14 Extraction voltage (a), Deflection voltage (b), and Extraction and deflection voltage (c)

4.7.2 Preliminary results and discussion of the final ion source

Figure 4-15(a) shows the result obtained after testing the ion source. The top target slide in the photograph shows the reference target slide with the beam of silver collected on it and the bottom target slide shows the deflected beam of silver ions. The reference target slide show the result obtained when no deflection voltage was switched on and the position of the beam on the slide depended on how the ion source was positioned. This result indicates that when the target was far away from the collimator the spot of silver ions on the target slide became larger and less intense. The deflector plates used were 40 mm in length, the separation distance between deflector plates was 34.2 mm, the collimator was 17.2 mm above the ion source and the target was 10 mm above the deflector plates and 60 mm above the collimator. The arcing voltage was 2 kV, the extraction and acceleration voltages were both -3 kV and the deflection voltage was 1 kV.

The result shown in Figure 4-16(a) was obtained when the target was brought closer to the collimator and shorter (25 mm) deflector plates were used. The target slide on top in figure 4-16(a) shows the reference target slide and the bottom slide shows the deflected beam of silver ions. The result showed that the deflected beam of silver ions was not clear enough on the target because the round spots on both target slides were not equal and this made it difficult to measure the deflection. The experiment was repeated and figure 4-17(a) shows result obtained after repeating the experiment. From this result the deflected beam of silver ions on the target was clear. The length of deflector plates was 25 mm, the separation distance between the deflector plates was 20 mm, the target was 10 mm away from the deflector plates and 40 mm away from the small collimator. The arcing voltage was 2 kV, the extraction and acceleration voltages are -3 kV and the deflection voltage was -1 kV. The results shown in figure 4-15(a) figure 4-16(a) and figure 4-17(a) were the results obtained during the testing of the ion source. The enhanced photographs were obtained using Microsoft Word by adjusting the contrast until the spots became clearer.

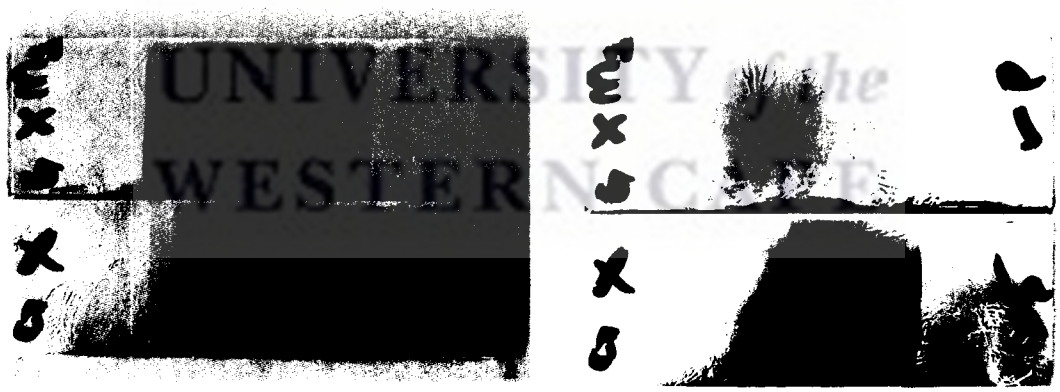

Figure 4-15 (a) Original photograph and (b) Enhanced photograph of figure 4-15 (a)

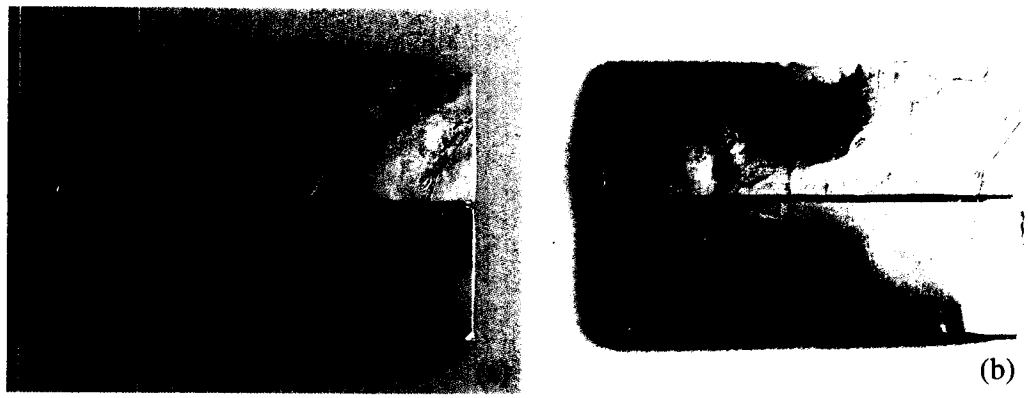

Figure 4-16 (a) Photograph results of the deposited silver ions and (b) Enhanced photograph of figure 4-16 (a)

Figure 4-17 (a) Results of the repeated experiment of Figure 4-16 (b) and Enhanced photograph of figure 4-17 (a)

4.7.3 Final results and discussion of the final ion source

Figure 4-18(a) shows all the results obtained after running the experiments. At the top of figure 4-18(a) is the reference target slide. The beam of silver was collected on the far left of the target so that the beam of silver ions can be seen to move to the right hand side of the target as the particles experience deflection. For the reference target the deflection voltage was not switched on. The deflection voltages used for the second, third and fourth target were 1.0, 1.5 and 2.0 kV respectively. Moving down the target slides, the beam spots were observed to move to the right hand side, which confirmed deflection of silver ions by uniform electric field. The deflector plates used were 25 mm in length, separation distance between the deflector plates was 30 mm, the collimator was 10 mm above the ion source, the deflector plates were 5 mm above the collimator and the target was 10 mm above the deflector plates and 40 mm above the collimator.

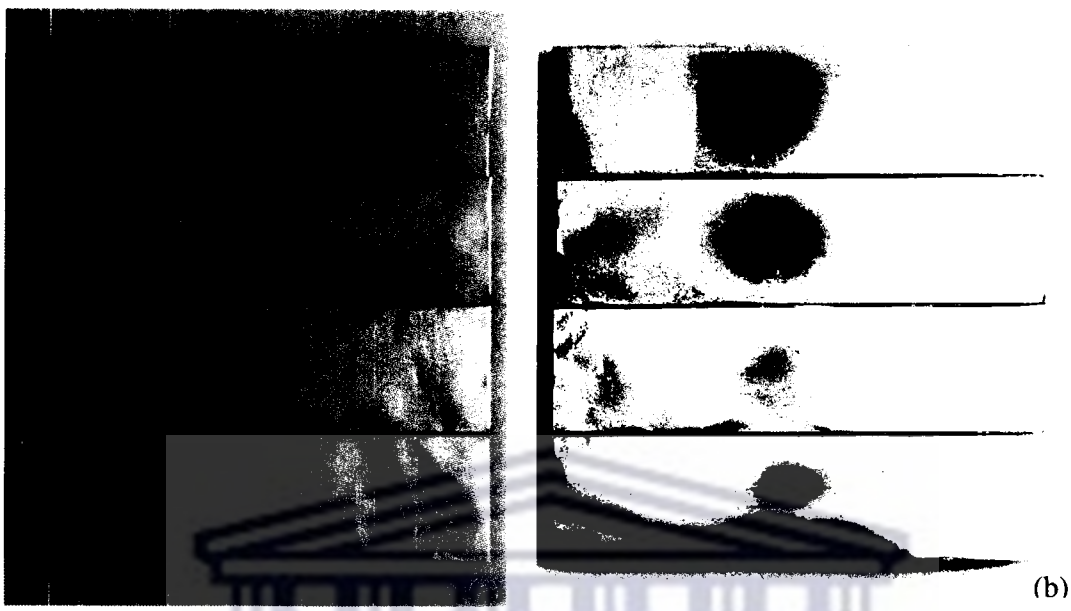

(b)

Figure 4-18 (a) Final results (b) Enhanced photograph of the final results

Table 4-1 shows the experimental deflection results measured independently by different people. This was done because the exact deflection is not clearly defined and its precise position subject to personal interpretation hence a number of people were asked to do the measurements. The samples measured are shown in figure 4-18 (a). The top target slide in figure 4-18 (a) is the reference target. It was measured first to get a reference value. The reference target is the result obtained when the deflection voltage was not switched on. The measured values on the second, third and fourth target were subtracted from the reference value to get the experimental deflection results shown in table 4-1. Each row in the table represents a set of results measured by each individual. The columns categorises the deflection results according to their deflection voltages DV.

Table 4-1 Experimental results of deflection measured independently by different people

Deflection (mm) at 1 kV DV	Deflection (mm) at 1.5 kV DV	Deflection (mm) at 2 kV DV
3.0	2.6	5.3
1.7	2.1	4.9
1.5	2.4	4.0
1.9	2.3	4.8
2.2	1.0	4.4
2.7	2.3	4.5
1.9	1.2	4.2
2.2	2.5	4.6

Table 4-2 show the average deflection results of table 4-1 of each column and table 4-3 show the average theoretical deflection results obtained using different deflection voltages. The theoretical and experimental deflection results obtained when deflection voltages of 1 and 2 kV were used are in agreement to within 11.6 and 5.9 % (as shown in table 4-2 and table 4-3 respectively. However the deflection results for theory and experiment when a deflection voltage of 1.5 kV was used are not in agreement. The experimental result differs by 43 % from the theoretical. This was attributed to an erratic voltage switching device in the electronic circuit of the power supplies.

Table 4-2 Average experimental deflection results

Extraction voltage (kV)	Deflection voltage (kV)	Average experimental deflection (mm)
3.0	1.0	2.14
3.0	1.5	2.05
3.0	2.0	4.59

Table 4-3 Average theoretical deflection results

Extraction voltage (kV)	Deflection voltage (kV)	Average theoretical Deflection (mm)
3.0	1.0	2.42
3.0	1.5	3.62
3.0	2.0	4.88

Figure 4-19(a) – (h) show the plots of measured experimental deflection results of each individual person against deflection voltages. Figure 4-20 shows the plot of the average theoretical deflection results and the average of the experimental deflection results measured by each individual against deflection voltage. The experimental result shown in figure 4-20 is an average of the experimental results of all the plots of figure 4-19(a) – (h)

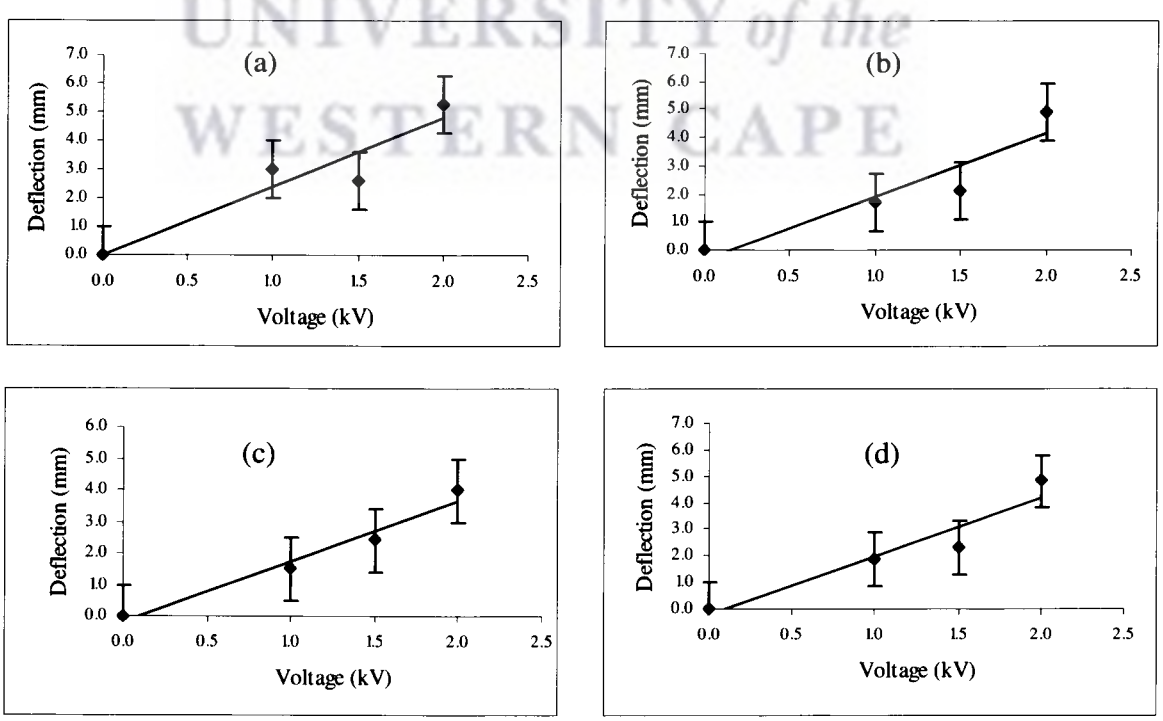

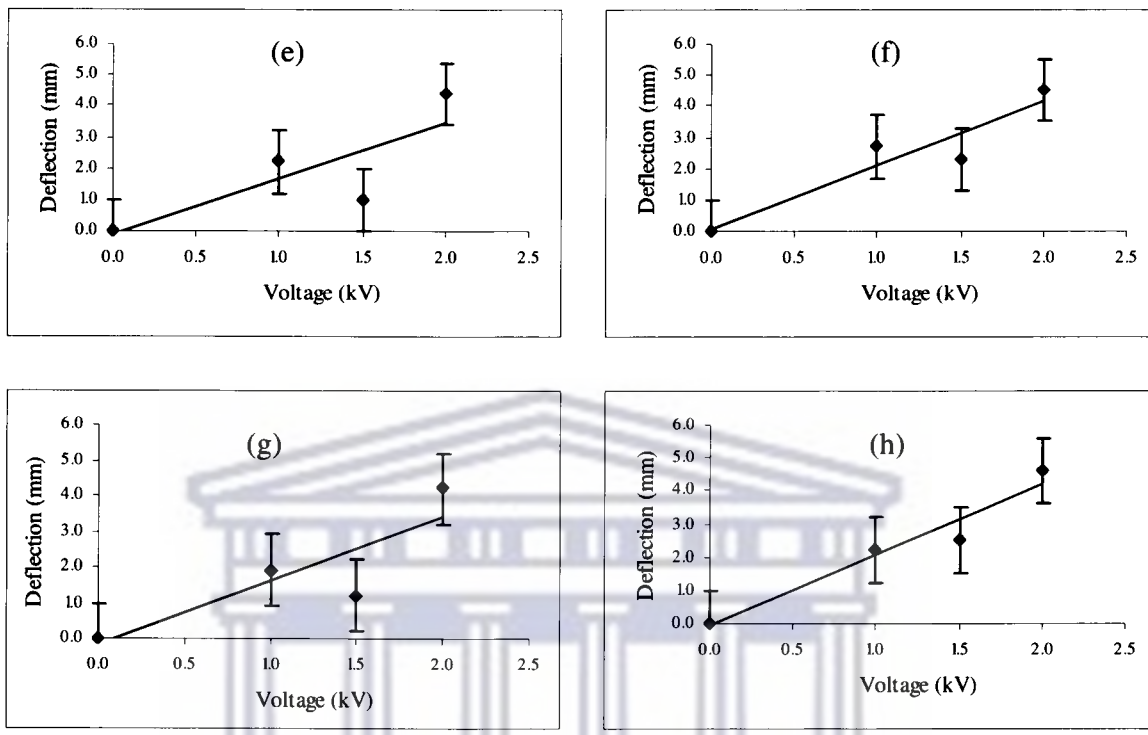

Figure 4-19 (a)-(h) Plots of measured experimental deflection results against deflection voltages

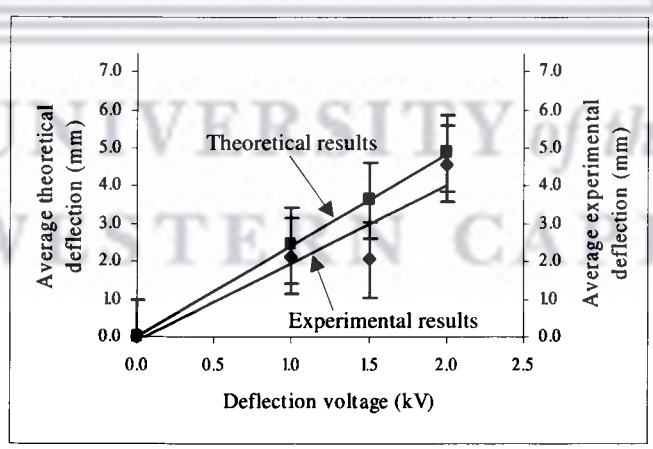

Figure 4-20 Theoretical and experimental results

Figure 4-20 show the comparison of the theoretical and experimental results. The theoretical results in the figure show a linear relationship between the voltage increase and the deflection increase. The linear regressions of the theoretical and experimental results are not far apart, as shown in figure 4-20 which shows that both results are in agreement.

4.7.4 Error analysis of the experimental results

For any data acquired, it is important to calculate the error associated with the measured results. In order to calculate the standard error of the data shown in each column of table 4-1, standard deviation was calculated to determine how close the measured experimental results are to each other. Table 4-4 show the variables needed to determine the standard deviation and the column 1 of table 4-4 gives the measured experimental deflection results as shown in column 1 of table 4-1.

Table 4-4 Standard deviation variables

X_i	M	$(X - M)$	$(X - M)^2$	N
3	2.14	0.86	0.74	8
1.7	2.14	-0.44	0.19	8
1.5	2.14	-0.64	0.41	8
1.9	2.14	-0.24	0.06	8
2.2	2.14	0.06	0.00	8
2.7	2.14	0.56	0.31	8
1.9	2.14	-0.24	0.06	8
2.2	2.14	0.06	0.00	8

The standard deviation is calculated as follows

$$SD = \sqrt{\frac{\Sigma(X_i - M)^2}{N-1}} = \sqrt{\frac{1.77}{7}} = 0.5 \quad 4.1$$

where X_i is the measured experimental deflection result, mm
i is the running index
M is the average of the measured experimental deflection results, mm
$(X - M)$ is the difference between the measured value and the average, mm
N is the number of the measured values
SD is the standard deviation, mm
SE is the standard error, mm

The standard error determines the variability of the averages experimental result and is calculated as follows

$$SE = \frac{SD}{\sqrt{N}} = \frac{0.5}{\sqrt{8}} = 0.18 \quad 4.2$$

To determine the range/interval of the measured results a confidence interval was determined and equation 4.3 was used to determine the range/interval. For 95% confident interval (CI) the average value shown in table 4-4 lies within a given interval and the interval is determined as follows

$$95\%\ CI = M \pm (1.96 \times SE) \quad 4.3$$

$$= 2.14 \pm 0.35 = 1.79 \textit{ and } 2.49$$

The average experimental deflection result can be said with 95 % confidence to lie between 1.79 and 2.49 mm. The same procedure was followed to calculate the standard deviation of table 4-5 and table 4-6. Table 4-5 shows the measured experimental results shown in column 2 of table 4-1 and the standard deviation, standard error and confidence interval were determined to be 0.60, 0.21, and 1.63 and 2.47 respectively. Table 4-6 shows the measured experimental results shown in column 3 of table 4-1 and the standard deviation, standard error and confidence interval were determined to be 0.41, 0.15, and 4.30 and 4.88 respectively.

Table 4-5 Standard deviation

X	M	$(X - M)$	$(X - M)^2$	N
2.6	2.05	0.55	0.30	8
2.1	2.05	0.05	0.00	8
2.4	2.05	0.35	0.12	8
2.3	2.05	0.25	0.06	8
1	2.05	-1.05	1.10	8
2.3	2.05	0.25	0.06	8
1.2	2.05	-0.85	0.72	8
2.5	2.05	0.45	0.20	8

Table 4-6 Standard deviation variables

X	M	$(X - M)$	$(X - M)^2$	N
4.30	4.59	0.71	0.50	8
4.90	4.59	0.31	0.10	8
4.00	4.59	-0.59	0.35	8
4.80	4.59	0.21	0.04	8
4.40	4.59	-0.19	0.04	8
4.50	4.59	-0.09	0.01	8
4.20	4.59	-0.39	0.15	8
4.60	4.59	0.01	0.00	8

Chapter 5

5 DISCUSSION, CONCLUSION AND RECOMMENDATIONS

5.1 Discussion

Using the first and second design of the ion sources as discussed in section 4.3.1 and 4.4.1, no silver ions deposited on the glass target. Due to the unreliability of these sources to consistently produce ions for a sufficiently long time, the experiments could not run for enough time for the deposition of silver particles to be visible on the glass target. The unreliability of these ion sources led to the third design of the ion source. With the third design of the ion source deposition of silver particles was observed, but the ion source produced more uncharged particles than charged particles and required very high voltages. At high voltage (-20 kV) the electromagnetic radiation produced during the formation of an arc caused the turbo pump power supply to shut down.

The final design of the ion source showed that changing the insulating material from glass to Teflon improved the performance of the ion source significantly. As discussed in the section 4.7 this design is similar to the second design. The improvement of the performance of this ion source was caused by the high breakdown voltage of Teflon compared to glass (as shown in Appendix D). This property of Teflon allowed the ion source to run for a longer time. Three to four experiments were performed without changing the ion source. Running the experiments for longer time was crucial for this work because silver particles needed time to deposit on the target plate. On average each experiment ran for five hours. Figure 5.1 show results obtained when the experiment operated for less than four hours. This was during the testing of the ion source during which the amount of time required for the experiments was investigated.

Figure 5-1 Unclear results due to short test duration.

The upper and lower target slides in figure 5-1 show results obtained when the experiments were conducted for approximately four and three hours respectively. However the main reason for the experiments being conducted for five hours was the fact that a DC power supply was used (3 kV, 10 mA, 50 Hz). The arcing pulses during the breakdown voltage were not consistent and varied from seconds to minutes. As the experiment progressed it was observed that the time difference between the pulses increased, which led the experiment to run for a longer time. Teflon also burnt away as the experiment progressed, as shown in the figure 5-2. When Teflon burnt away it caused the plasma to be formed at the tip of the

insulator material (between the electrodes) instead of at the tip of the electrodes. This phenomenon also contributed to the increase in the time lapse between the pulses at which the plasma was formed. The increase in time lapse between the pulses made external triggering of the power supply by hand necessary to initiate an arc and this caused the experiments to be run for a long time (5 hours).

Figure 5-2 Ion source after running the experiment

5.2 Conclusion

The objectives of this thesis were met, ions were generated, extracted, deflected and deposited in vacuum. The first and second designs of the ion sources did not generate silver ions due to their unreliability and that they could not run for a long enough time to allow the deposition of silver on the target. The first design of the power supply shown in figure 4.4 could not provide the necessary voltages for arcing for a longer time because it overheated during the experiment. The third design of the ion source generated ions but was discontinued because it required very high arcing voltage (20 kV). The electromagnetic radiation produced when high voltages were used caused the turbo pump to stop working. The final design of the ion source did not only produce the silver ions but operated for a longer time at low arc voltage (2 kV). The performance of this ion source was improved by the use of Teflon as an insulator between the electrodes. Externally triggering the power supply by hand reduced the increase of the time lapse between the pulses of the power supply which allowed the final design of the ion source to produce more ions.

The extraction of silver ions was achieved by using an extraction voltage of -3 kV as is shown in figure 4-12(b). The extraction of ions was also enhanced by the voltage connection on the final design of the ion source. The silver ions were observed to move away from the ion source due to the positive charge on the central electrode and the high negative charge on the collimator. Figure 4-18(a) shows that the deflection of silver ions was achieved. The deposition of silver ions was observed to move to the right hand side of the target plate as shown in figure 4-18(a). The target plate was at the same potential as the collimator which caused the extracted ions to be further accelerated and that led to the deposit of silver ions on the target plate.

Tables 4-2 and table 4-3 show that the average experimental deflection and average theoretical deflection results obtained when ions were deflected with 1 and 2 kV are in agreement to within 11.6 and 5.9 % respectively. However the experimental result obtained

when ions were deflected with 1.5 kV is not in agreement with theoretical deflection result. This result differs by 43% and this was attributed to the discrepancies of the power supply as discussed in section 4.7.3.

5.3 Recommendations

The results obtained for this work show that deflection of silver in vacuum is possible. It is recommended that the same experiment be conducted in helium. When a DC power supply was used to generate ions inconsistent pulses were observed. It is recommended that a pulsing supply be used in order to reduce the experiment operating time

6 References

Anders, A. (2003), *Cathode Arcs*, Lawrence Berkeley National Laboratory, University of California

Anders, A. (2006), Physics of Arcing and Implications to Sputter Deposition, *Thin Solid Films*, Vol. 502, pp. 22-28

Anders, A. and Hollinger, R. (2001), Reducing Ion Beam Noise of Vacuum Arc Ion Source, *Review of Scientific Instruments*, Vol. 73, No. 2, pp. 732-734

Anders, A. and Kwan, J.W. (2001), Arc-Discharge Ion Source for Heavy Ion Fusion, *Nuclear Instrument and Methods in Physics Research A*, Vol. 464, pp. 569-575

Bartzsch, H. *et al.* (2000), Anode Effects on Energetic Particle Bombardment of the Substrate in Pulsed Magnetic Sputtering, *Surface and Coating Technology*, Vol. 132, pp. 244-250

Boxman, R.L. (2001), Recent Developments in Vacuum Arc Deposition, *IEEE Transations on Plasma Science*, Vol. 29, No. 5

Boxman, R.L. (1995), *Handbook of Vacuum Arc Science and Technology*, Neyes Publications, New Jersey

Brown, I.G. (1993), Vacuum Arc Ion Source for Particle Accelerators and Ion Implantation, *IEE Transactions on Plasma Science*, Vol. 21, No. 5.

Brown, I.G. *et al.* (1996), Recent Advances in Vacuum Arc Ion Source, *Surface and Coatings Technology*, Vol. 84, pp. 50-556

Brown, I.G. (2004), *The Physics and Technology of Ion Source*, Wiley-VCH, Second edition

Cassady, R.J. *et al.* (2008), Recent Advances in Nuclear Powered Electric Propulsion for Space Exploration, *Energy Conversion and Management*, Vol. 49

Claypool, I.R. (2007), *A Theoretical and Numerical Study of the use of Grid Embedded Axial Magnetic Fields to Reduce Charge Exchange Ion Induced Grid Erosion In Electrostatic Ion Thrusters*, Dissertation, Ohio State University, USA

Cogliati, J.J. and Ougouag, A.M. (2008), Pebble Bed Reactor Dust Production Model, *Proceedings of the 4th International Meeting on High Temperature Reactor Technology*, September 28 – October 1, Washington DC

Coulombe, S. and Meunier, J-L. (1998), Cold Cathode Arc Attachments the Importance of the High Local Pressure, *Pure and Applied. Chem.*, Vol 70, No. 6

Cylan, O. and Kalenderli, O. (2004), Parallel Computing of two Dimensional Electric Field Distribution Using PETSC, *Lecture Series on Computer and Computational Sciences,* Vol 1, pp. 1-3

Djakov, B.E. (2000), A Model Describing the Arc Between Closely Spaced Electrodes, *Vacuum*, Vol. 58, pp. 233-243

Dunning, F.B. and Hulet, R.G. (1995), *Atomic, Molecular, and Optical Physics: Charged Particles*, Academic Press, Vol. 29A

Fuchs, H. *et al.* (1998), Distribution of Ion Current Density in a Modified Pulse Arc Process as a Function of Pulse Parameters, *Surface and Coatings Technology*, Vol. 98, pp. 839-844

Goebel, D.M. and Kats, I. (2008), *Fundamental of Electric Propulsion Ion and Hall Thrusters*, John Wiley, New York

Guoqiang, L. *et al* (2005), Substrate Temperature Calculation for Pulsed Bias Arc Ion Plating, *Surface and Coatings Technology*, Vol. 194, pp.325-329

Grissom, J.T. and McClure, G.W. (1971), Energy Distribution of Ions from the Anode Plasma of a Pulsed Vacuum Arc, *International Journal of Mass Spectrometry and Ion Physics*, Vol 9

Grove, T.C. (2000), *Arcing Problems Encountered During Sputter Deposition of Aluminum*, Advanced Energy Industries, USA

Harding, J. (2005), *Pebble Bed Modular Reactors-Status and Prospects*, Jim Harding

Hassan, A. *et al.* (2008), Analytical Studies of the Plasma Extraction Electrodes and Ion Beam Formation, *Nuclear Instrument and Methods in Physics Research A*, Vol. 586, pp. 148-152

Integrated Engineering Software, (2009), *Lorentz-2E V7.0*, 220-1821 Wellington Avenue, Winnipeg Manitoba, Canada R3H 0G4

Ion, S. *et al.* (2004), Pebble Bed Modular Reactor-The First Generation IV Reactor to be Constructed, *Nuclear Energy*, Vol. 43, No. 1, pp. 5-62

Karpov, D.A. (1997), Cathodic Arc Sources and Macroparticle Filtering, *Surface and Coatings Technology*, Vol. 96, pp. 22-33

Messaad, M. *et al.* (2006), Model for a Low Current Vacuum Arc Cathode Region Effect of the Electronic Temperature, *Acta Electrotechnica et Information*, Vol 6, No.3

Meunier, J-L. and Coulomb, S. (1998), Cold Cathode Arc Attachment: The Importance of the High Local Pressure, *Pure and Applied Chem*, Vol. 70, No. 6, pp. 117-1180

Miernik, K. and Walkowicz, J. (2000), Spatial Distribution of Microdroplets Generated in the Cathode Spots of Vacuum Arcs, *Surface and Coatings Technology*, Vol. 125, pp. 161-166

Monageng, S.M. (2010), *Design and Operating Aspects of a Magnetic Isotope Scrubber Model for Removing Silver Ions from the Pebble Bed Modular Reactor Hot Pipe*, MARST-Mini-Dissertation, North West University, South Africa

Pham, H.H. (1998), *Numerical Capacitance Extraction for Large-Area Systems*, Dissertation, University of Waterloo, Canada

Siemroth, P. *et al.* (1995), Fundamental Processes in Vacuum Arc Deposition, *Surface and Coating Technology*, Vol. 74-75, pp. 92-96

Siemroth, P. *et al.* (1997), Investigation of Cathode Spots and Plasma Formation of Vacuum Arcs by High Speed Microscopy and Spectroscopy, *IEE Transactions on Plasma Science*, Vol 25, No.4

Sugimoto, M. *et al.* (2004), Grain Structure in Cathode Spot Trial of Low Vacuum Arc Discharge, *Thin Solid Films*, Vol. 457, pp.168-173

Takeda, K. and Tekeuchi, S. (2002), Effects of Pressure on the Cleaning Action of Cathode Spot in Low Vacuum, *Thin Solid Films*, Vol. 407, pp. 163-168

Treglio, J.R. *et al.* (1997), Advance Vacuum Arc Metal Ion Implantation System, *Surface and Coating Technology*, Vol. 96, pp. 1-8

Ushio, M. (1988), Arc Discharge and Electrode Phenomena, *Pure and Appl.Chem*, Vol. 60, No. 5, pp. 809-814

Verfondern, K. *et al* (2007), Coated Particle Fuel for High Temperature Gas Cooled Reactors, *Nuclear Engineering and Technology*, Vol. 39, No. 5

Young, H.D. and Freeman, R.A. (1996), *University Physics*, Addison-Wesley, Ninth Edition

Zine, B. *et al.* (2005), Modelling of Collision in the Plasma Sheath and the Cathode Erosion of Electrical Arc, *M.J. Condensed Matter*, Vol. 6, No. 1

Appendix A

A.1 Deflection of silver ions using uniform electric field

A.1.1 Sample Calculation

A.1.1.1. Electrostatic Deflection of the Ion Beam

Ions emerge from the ion source with a kinetic energy 2 kV. The method used to generate these ions is the arcing method. When arcing with 2 kV the ions produced were born between the potential ranges of 0 to 2 kV. For this calculation only 0, 500, 1500 and 2000 V are considered. The produces ions are further accelerated by the extracting collimator which is at -3 kV. The negative sign represents the direction of the silver beam. The potential differences of all the produced ions are 3, 3.5, 4, 4.5 and 5 kV. The potential difference of the ions in this calculation is designated as V and is calculated as follows

$$V = EV - AV \quad \text{.....A.1}$$

where EV is the extraction voltage, kV
AV is the arcing voltage, kV

The kinetic energy E_{kin} of the particles is given by

$$E_{kin} = \frac{1}{2}mv^2 = eV$$

where m is the mass of the silver particle, eVs^2/m^2
v is the velocity of the particle, m/s

$m = 1.13 \times 10^{-6}\ eVs^2/m^2,\ V = 3\ kV, 3.5\ kV, 4\ kV, 4.5\ kV, 5\ kV$

A.1.1.2 The longitudinal velocity, v of the ion beam is

$$v = \sqrt{\frac{2eV}{m}} \quad \text{.....A.2}$$

$$= \sqrt{\frac{2 \times 3\ keV}{1.13 \times 10^{-6}} \frac{m^2}{eVs^2}}$$

$$= 72928\ m/s$$

Figure A-1 represents the experimental set-up. It shows the path taken by a mono energetic particle of silver after it has been produced by the ion source. The silver ion

passes the extracting collimator and enters the deflection region where it experiences deflection. Figure A-1 also shows the particle depositing on the target after it has experienced deflection.

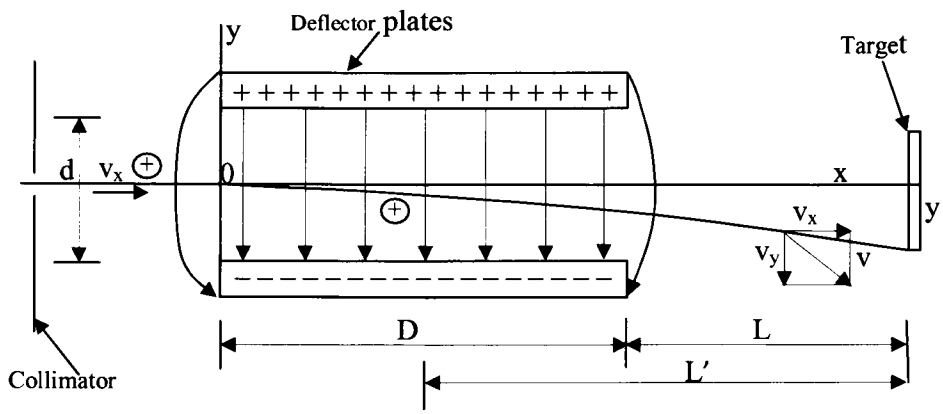

Figure A-1 Deflection of silver ions in a uniform electric field (Young, and Freeman, 1996)

A.1.1.3. Magnitude of the field

The magnitude of the electric field is determined by the potential difference V_x, between the deflector plates separated by distance d:

$$E = \frac{V_x}{d} \quad \text{.....A.3}$$
$$= \frac{0V-(-1000V)}{3 \times 10^{-2}m}$$
$$= 33333\,V/m$$

A.1.1.4. Transverse acceleration

After extraction ions enter the region of uniform transverse electric field E. As these ions enters this region they experience a transverse force which is eE and this force produces a transverse acceleration a_x whose magnitude is given by Newton's second Law of motion:

$$eE = ma_x \quad \text{.....A.4}$$
$$a_x = \frac{eE}{m}$$
$$a_x = 2.95 \times 10^{10} m/s^2$$

A.1.1.5. Time spent in the field

Figure A-2 show the deflector plates that produce the uniform electric field. The deflection region decides the amount of time the particle will spend whilst

experiencing deflection. The longer the deflection region the more time the particle will spend in the deflection region.

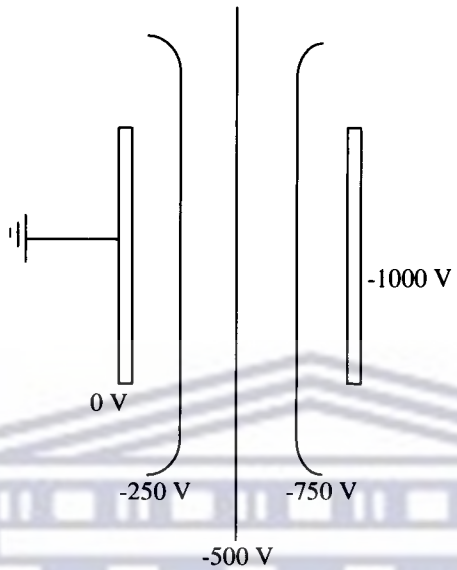

Figure A-2 shows deflector plates with potential lines in between.

The time spent in the field is given by equation A.5 where D is the length of the deflector region

$$D = 2.5\ cm$$

$$t = \frac{D}{v} \quad \text{.....A.5}$$

$$= \frac{2.5 \times 10^{-2}\ ms}{72927.8\ m} = 3.42 \times 10^{-7} s$$

A.1.1.6. Transverse velocity

The acquired transverse velocity is

$$v_x = a_x t \quad \text{.....A.6}$$

$$= 2.95 \times 10^{10} \times 3.42 \times 10^{-7} ms/s^2 = 10113\ m/s$$

A.1.1.7. Transverse displacement

After the particle leaves the deflector region it takes an additional time L/v to reach the target, where L is the additional longitudinal distance travelled. During this time the particle undergoes a transverse displacement, y

$$L = 1\ cm, v_x = 10112\ m/s$$

$$y = \frac{L}{v} v_x \quad \text{.....A.7}$$
$$= 0.0014\ m$$

To verify the result above equation A.7 can also be written as

$$V_x = 1000\ V, V = 3000\ V, d = 0.03\ m$$

$$y = \frac{LD}{2d}\frac{V_x}{V} \quad \text{.....A.8}$$
$$= 0.0014\ m$$

Equation A.7 calculates the transverse deflection which occurs after the ion leaves the deflection region. Equation A.9 gives total deflection, y' if L is replaced by L', the distance from the middle of the deflection region to the target

$$L' = 0.0225\ m$$
$$y' = \frac{L'D}{2d}\frac{V_x}{V} \quad \text{.....A.9}$$
$$= 0.00313\ m$$

The same procedure was used to calculate the theoretical deflection of different potential differences of the ions and different deflection voltages. Table A-1 show the deflection results obtained when the ion was born at different arcing voltage. Table A-1 also show that when the particle is born at high arcing voltage it experiences less deflection (as it is shown in column 4, 5 and 6). Table A-2 show the average theoretical deflection results of table A-1. Deflection increases as the deflection voltage increase.

Table A-1 Theoretical results of deflection

Arcing voltage (kV)	Extraction voltage (kV)	Potential difference of the ions, V (mm)	Deflection (mm) at 1 kV DV	Deflection (mm) at 1.5 kV DV	Deflection (mm) at 2 kV DV
0	3	3	3.1	4.7	6.8
0.5	3	3.5	2.7	4.0	5.4
1	3	4	2.3	3.5	4.7
1.5	3	4.5	2.1	3.1	4.2
2	3	5	1.9	2.8	3.8

Table A-2 Average theoretical results of deflection

Extraction voltage (kV)	Deflection voltage (kV)	Average theoretical deflection (mm)
3	1.0	2.42
3	1.5	3.62
3	2.0	4.88

A.2 Theoretical and Simulation Results

This section shows results obtained theoretically and by simulation using Lorent software. Figure A-1 represents the geometry used to calculate the deflection of silver particles for theoretical and experimental simulation. The drift length L and deflector spacing d were kept constant through out the theoretical calculation and experimental simulation. It was only the deflector plate length (Vertical side), arcing voltage and deflection voltage that were varied.

A.2.1 Theoretical Results

The theoretical results for deflection of silver ions of 1+ charge state in an electric field, for different deflector lengths and arcing voltages for deflection voltages of 300 V, 400 V, 500 V, drift length of 10 cm and deflector spacing of 5 cm are shown in Table A-3a to A-3c.

Table A-3a

Arcing Voltage (V)	Deflector Length (cm)	Deflection y'(cm)
1000	2.5	0.8438
1000	5.0	1.8750
1000	7.5	3.0938
2000	2.5	0.4219
2000	5.0	0.9375
2000	7.5	1.5469
3000	2.5	0.2813
3000	5.0	0.6250
3000	7.5	1.0313
4000	2.5	0.2109
4000	5.0	0.4688
4000	7.5	0.7734

Table A-3b

Arcing Voltage (V)	Deflector Length (cm)	Deflection y' (cm)
1000	2.5	1.1250
1000	5.0	2.5000
1000	7.5	4.1240
2000	2.5	0.5625
2000	5.0	1.2500
2000	7.5	2.0625
3000	2.5	0.3750
3000	5.0	0.8330
3000	7.5	1.3750
4000	2.5	0.2813
4000	5.0	0.6250
4000	7.5	1.0313

Table A-3c

Arcing Voltage (V)	Deflector Plates (cm)	Deflection y' (cm)
1000	2.5	1.4063
1000	5.0	3.1250
1000	7.5	5.1563
2000	2.5	0.7032
2000	5.0	1.5625
2000	7.5	2.5782
3000	2.5	0.4688
3000	5.0	1.0417
3000	7.5	1.7188
4000	2.5	0.3516
4000	5.0	0.7813
4000	7.5	1.2891

Table A-3 Deflection of Silver ions of 1+ charge state in an electric field, for different deflector lengths and arcing voltages, drift length of 10 cm and deflector spacing of 5 cm with a) deflection voltage of 300 V, b) deflection voltage 400V. c) deflection voltage of 500 V

Figures A-3 to A-5 show the deflection results obtained when the arcing voltage, deflection voltage and deflector plates were varied. Figure A-3 shows that the deflection of ions decreases as the arcing voltage increases. Figure A-4 shows the increase in deflection of the ions as the deflection voltage increases. Figure A-5 shows the increase in deflection as the deflector plate length increases.

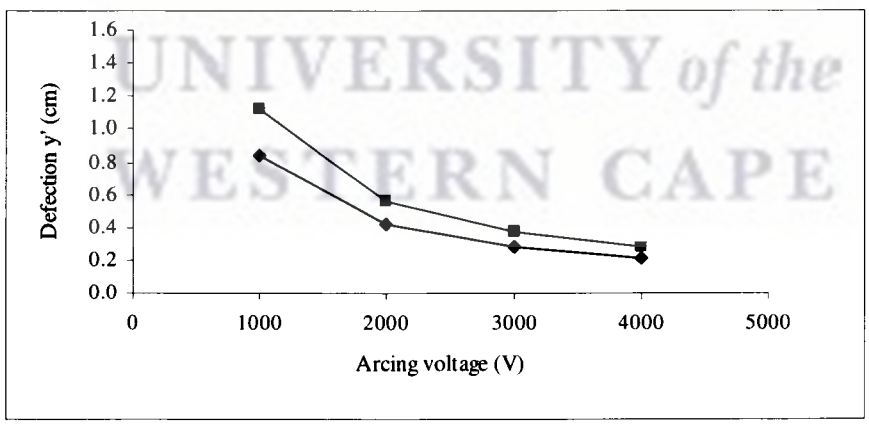

Figure A-3 An increase in deflection when increasing the deflection voltage for different arcing voltages.

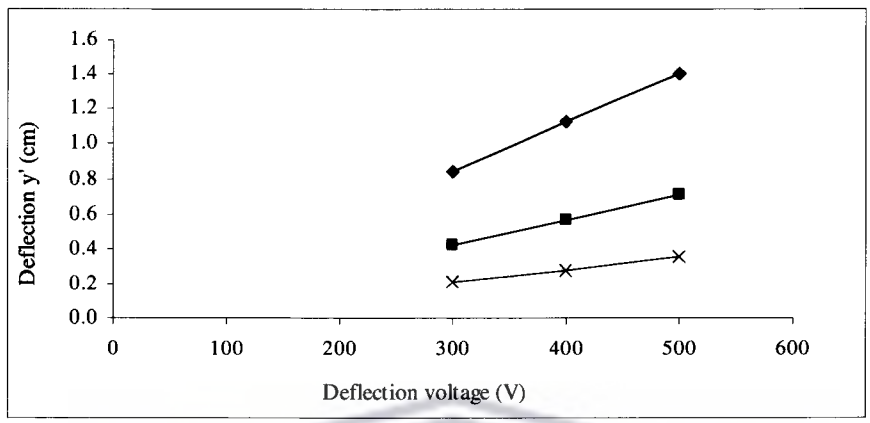

Figure A-4 Deflections obtained when varying the deflection voltage. Increasing the deflection voltage causes more deflection due to higher electric field.

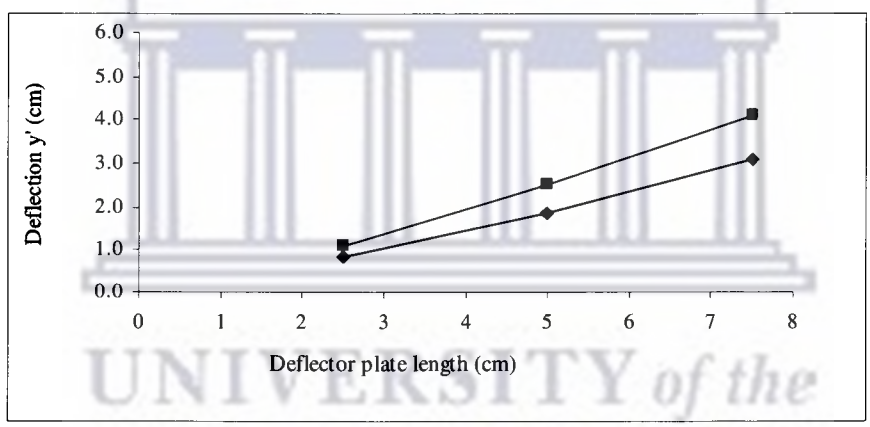

Figure A-5 An increase in the deflection of silver ions when increasing the length of deflector plates.

A.2.2 Experimental Simulation Results

The experimental simulation results show the deflection of silver ions of 1+ charge state in an electric field, for different deflector lengths and arcing voltages for deflection voltages of 300 V, 400 V, 500 V, drift length of 10 cm and deflector spacing of 5 cm (Integrated Engineering Software, 2009).

Table A-4a

Arcing Voltage (V)	Deflector Plates (cm)	Deflection y'(cm)
1000	2.5	1.27
1000	5.0	2.26
1000	7.5	3.57
2000	2.5	0.63
2000	5.0	1.14
2000	7.5	1.76
3000	2.5	0.417
3000	5.0	0.762
3000	7.5	1.17
4000	2.5	0.317
4000	5.0	0.527
4000	7.5	0.881

Table A-4b

Arcing Voltage (V)	Deflector Plates(cm)	Deflection y' (cm)
1000	2.5	1.69
1000	5.0	3.07
1000	7.5	4.79
2000	2.5	0.833
2000	5.0	1.52
2000	7.5	2.37
3000	2.5	0.556
3000	5.0	1.01
3000	7.5	1.56
4000	2.5	0.417
4000	5.0	0.762
4000	7.5	1.18

Table A-4c

Arcing Voltage (V)	Deflector Plates(cm)	Deflection y' (cm)
1000	2.5	2.10
1000	5.0	3.86
1000	7.5	6.10
2000	2.5	1.04
2000	5.0	1.93
2000	7.5	2.95
3000	2.5	0.702
3000	5.0	1.27
3000	7.5	1.94
4000	2.5	0.527
4000	5.0	0.951
4000	7.5	1.47

Table A-4 Deflection of Silver ions of 1+ charge state in an electric field, for different deflector lengths and arcing voltages, drift length of 10 cm and deflector spacing of 5 cm with a) deflection voltage of 300 V, b) Deflection voltage of 400V. c) Deflection voltage of 500 V

Figure A-6 to A-8 show the deflection results obtained when the arcing voltage, deflection voltage and deflector plates were varied. Figure A-6 show that the deflection of ions decreases as the arcing voltage increases. Figure A-7 show the increase in deflection of the ions as the deflection voltage increases. Figure A-8 also shows the increase in deflection as the deflector plate length increases. Theoretical and experimental simulation results show that the deflection of ions increases by increasing the deflection voltage and deflector plate length but increasing the extraction voltage decreases the deflection of the ions.

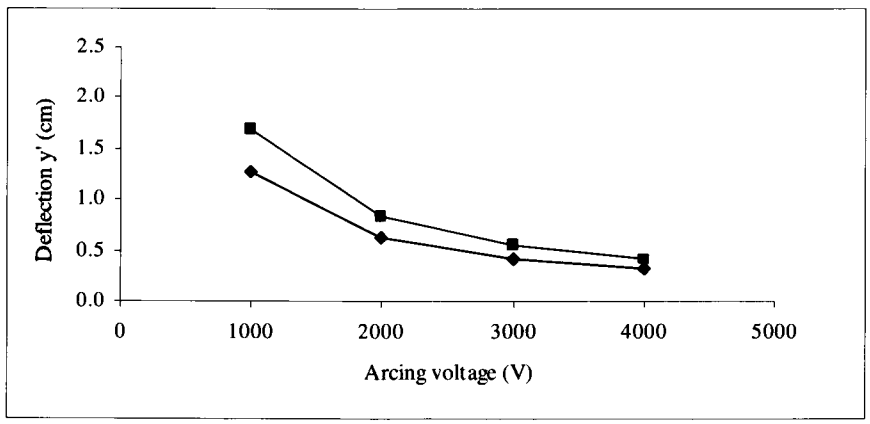

Figure A-6 deflections obtained when varying the deflection voltages. Increasing the deflection voltage causes more deflection due to higher electric field.

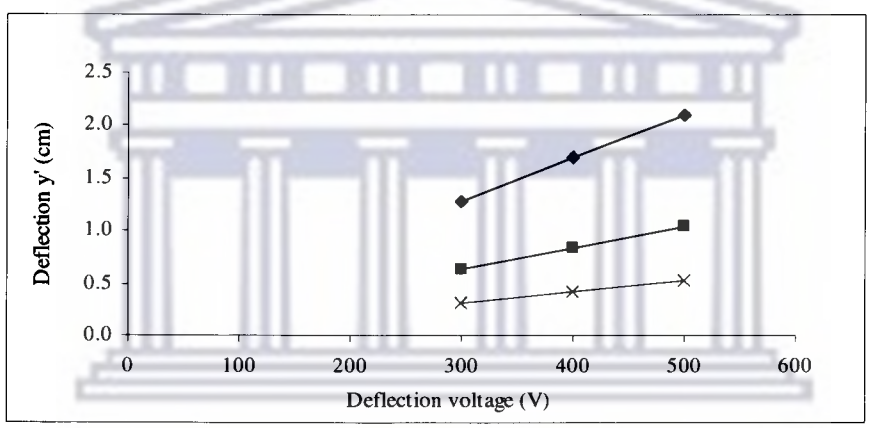

Figure A-7 the increase in deflection when increasing the deflection voltage for different arcing voltages.

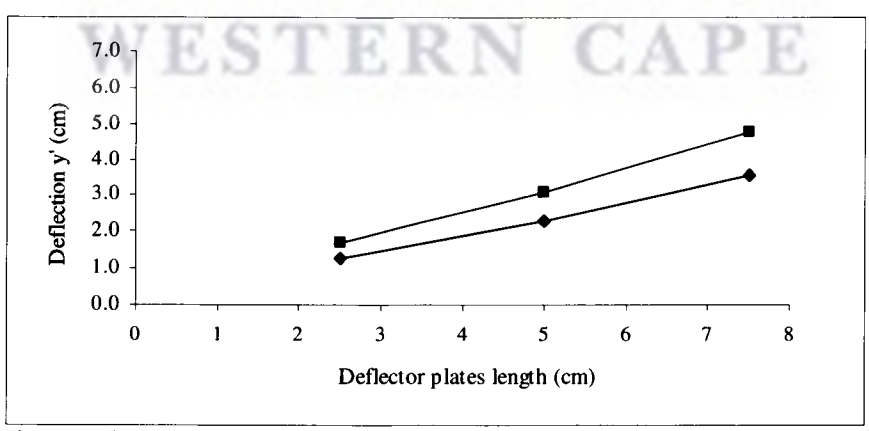

Figure A-8 the increase in the deflection of silver ions when increasing the length of the deflector plates.

Appendix B

B.1 Spot size variation

Figure B-1 shows the variation of the spot of deposited silver ions on the target plate. The calculation shown in this section was done to determine the size of the silver spot that will deposit during the experiment. Determining the size of the spot before running the experiment played an important role in setting the parameters of the experiment, for example the distance of the target from the collimator and the separation distance of the deflector plates. Figure B-1 also shows that choosing a small separation distance between the deflector plates would cause silver particles to deposit on the deflector plates.

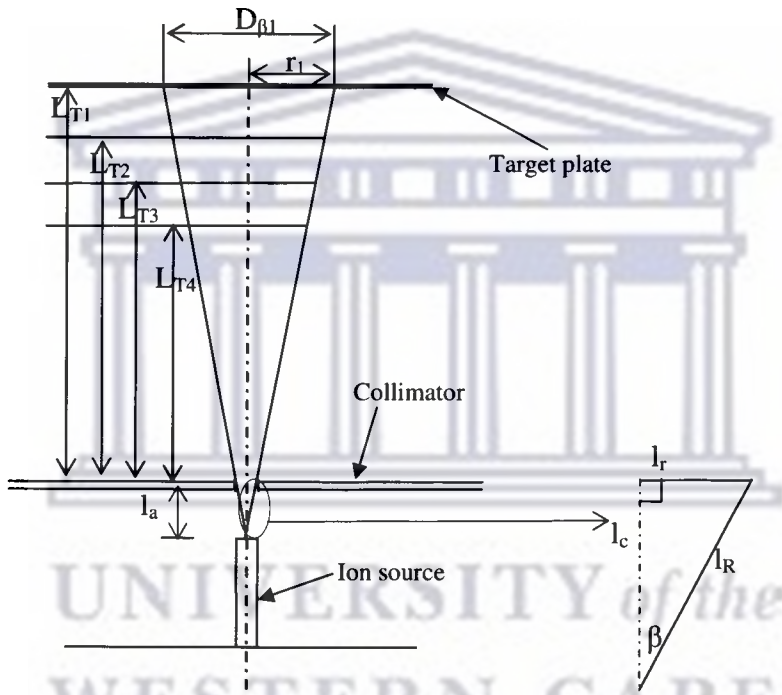

Figure B-1 Schematic of ion source, collimator and target plate

The calculation procedure is as follows:

i) Calculating the resultant of the deposition of silver on the target plate

Before determining the size of the spot of silver particles that will deposit on the target plate, the resultant and the angle at which the silver beam will be produced need to be determined

L_{T1} = 70 mm, L_{T2} = 60 mm, L_{T3} = 50 mm, L_{T4} = 40 mm , l_a = 10 mm, l_r = 1.2 mm,
l_R = ?

$$l_R = \sqrt{{l_a}^2 + {l_r}^2}$$
$$= \sqrt{(10)^2 + (1.2)^2}$$
$$= 10.1 \text{ mm}$$
$$Sin\beta = \frac{l_r}{l_a} = \frac{1.2}{10.1} = 0.12$$
$$\beta = 6.8°$$

where L_{Ti} is the distance of the target plate from the ion source, mm
i is the running index
l_a is the distance of the collimator from the ion source, mm
l_f is the radius of the collimator, mm
l_R is the resultant of the silver beam, mm
r_i is the radius of the beam spot, mm
$D_{\beta i}$ is the diameter of the spot, mm
β is the angle at which the silver beam is produced, degrees (^{o})

ii) Calculating the radius and the diameter

$$tan\beta = \frac{r_1}{L_{T1}} \quad \therefore r_1 = 70\tan(6.8°) = 8.378 \text{ m}$$

$D_{\varphi 1}$ = 2 x (8.378 mm) = 16.8 mm

Following the same procedure as above the radius and the diameter of the spots at L_{T2}, L_{T3}, and L_{T4} are calculated as:

r_2 = 7.16 mm, $D\varphi_2$ = 14.3 mm

r_3 = 5.16 mm, $D\varphi_3$ = 11.9 mm

r_4 = 4.77 mm, $D\varphi_4$ = 9.5 mm

These calculations show that as the distance to the target increases the spot becomes larger. Figure B-2 shows the increase of the spot diameter as the distance between the target and the ion source is increased.

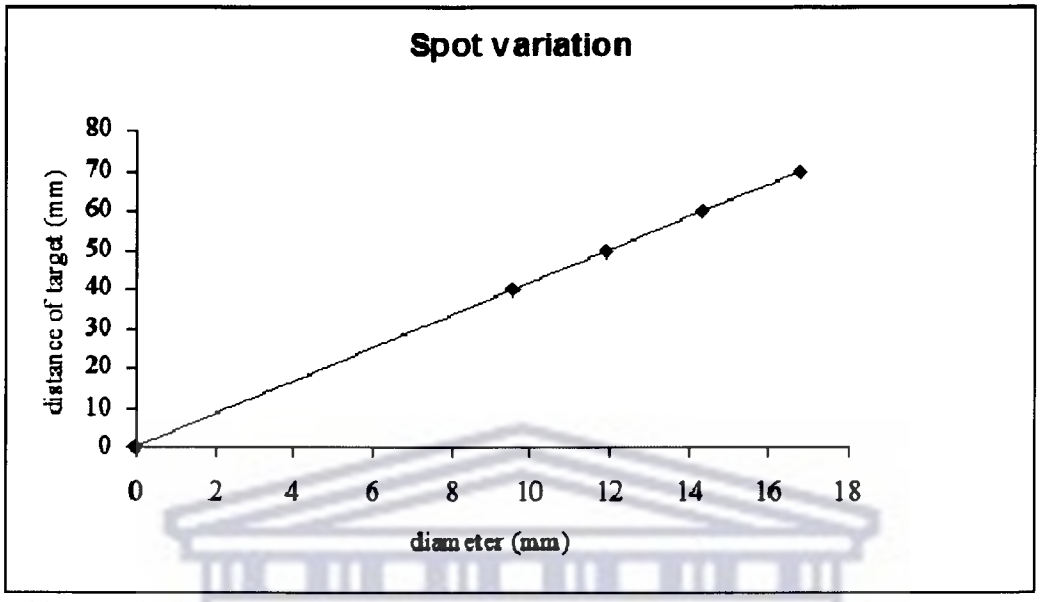

Figure B-2 Diameter of the silver spot on the target plate as the distance from the ion source to the target increase.

Appendix C

Safety Procedures For Experimental Set-up

Safety Measures

- Personnel must wear a lab coat, safety goggles and closed shoes at all times.
- During experimental operation personnel must be separated from the experimental setup by the safety glass shield.
- No unauthorised person may operate or change the experimental set-up.
- High voltage power supply must be handled with care.
- Before switching on the vacuum pumps ensure that all the valves are sealed.

Possible Hazards

- Electric shock
- Explosion of the glass cylinder in high vacuum
- Water leak

Preventatives Measures:

- Electric shock
  - ❖ Switch off the power supplies before changing the deflector plates and collimators.
  - ❖ No unauthorised person may change/adjust the deflector plates and collimators.
- Explosion of the glass cylinder
  - ❖ Ensure the safety glass shield is in place between the personnel and the experiment.
- Water leak
  - ❖ Switch off the power mains and then dry the area.

Operating Procedure

1. Ensure all safety gear is worn (safety goggles, lab coat and closed shoes).
2. Before assembling the apparatus make sure that all the power supplies are on safe mode/switched off and use the ground stick to check whether it is safe to assemble the apparatus.
3. The glass cylinder must be safely stored on an allocated cushion in the laboratory cupboard before and after operation.
4. Assemble the apparatus. Recheck for any errors in the assembly.
5. Vacuum: switch on the rotary vacuum pump first until the pressure of 10^{-3} Torr is reached, then switch on the turbo molecular pump. Test for leaks while the rotary pump is drawing vacuum, before the turbo pump is switched on.
6. Before switching on the arcing power supply make sure that deflector plates, collimators and target plate are at the correct potential and that there is no arcing between them.
7. Switch on the arcing power supply.
8. Open the tap water to run water for cooling and ensure that there is no water leak.

Safety Procedure During Operation

9. Stand behind the safety glass during operation.
10. Do not step on water or touch the experimental apparatus if there is a water (leak to prevent electric shock).

Safety Procedure After Running The Experiment

11. Switch off the turbo molecular pump first. Wait for 8 minutes and then switch off the rotary vacuum pump.
12. Switch off all power supplies and arcing power supply before dissembling the apparatus and use the ground stick to check for voltages.
13. Dissemble the apparatus and ensure that the glass cylinder safely stored.

7 Appendix D

Text Book Values of Various Dielectric Constant

Material	Dielectric constant	Break down voltage volts per mil	Matter phase	Other notes
Air	1	21	gas	
Bakelite	4.4 to 5.4	300	solid	
Cellulose Ascetate	3.3 to 3.9	250 to 600	solid	"cellophane"
Ethyl alcohol	24		liquid	industrial - pure bipolar
Formica	4.6 to 4.9	450	solid	
Glass	7.6 to 8	200 to 250	solid	common/window
Mica	5.4	3800 to 5600	solid	
Mylar®	3.2	7500	solid	
Paper	3	200	solid	no ink
Paraffin	2.1		solid	
Plexiglass	2.8	990	solid	
Polyethylene	2.3	1200	solid	
Polystyrene	2.6	500 to 700	solid	styrofoam
Porcelain	5.1 to 5.9	40 to 100	solid	
Quartz	3.8	1000	solid	
Rubber	2.8		solid	hard type
Teflon	2.1	1000 to 2000	solid	
Vacuum	1		n/a	
Vinyl	2.8 to 4.5		solid	
Water	76.5 to 80		liquid	distilled - bipolar

Appendix E

Engineering Drawings of the Experimental Set-Up

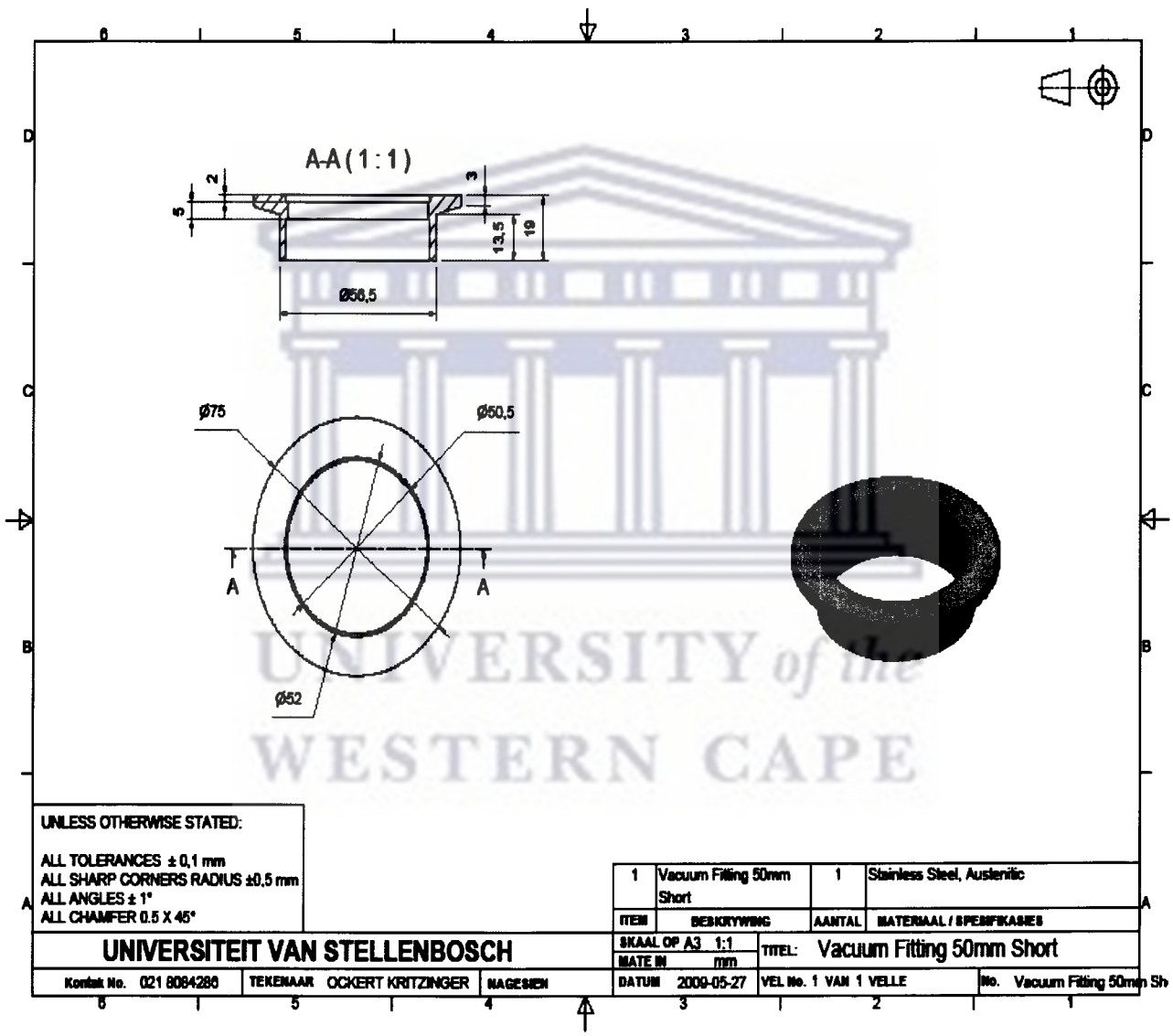

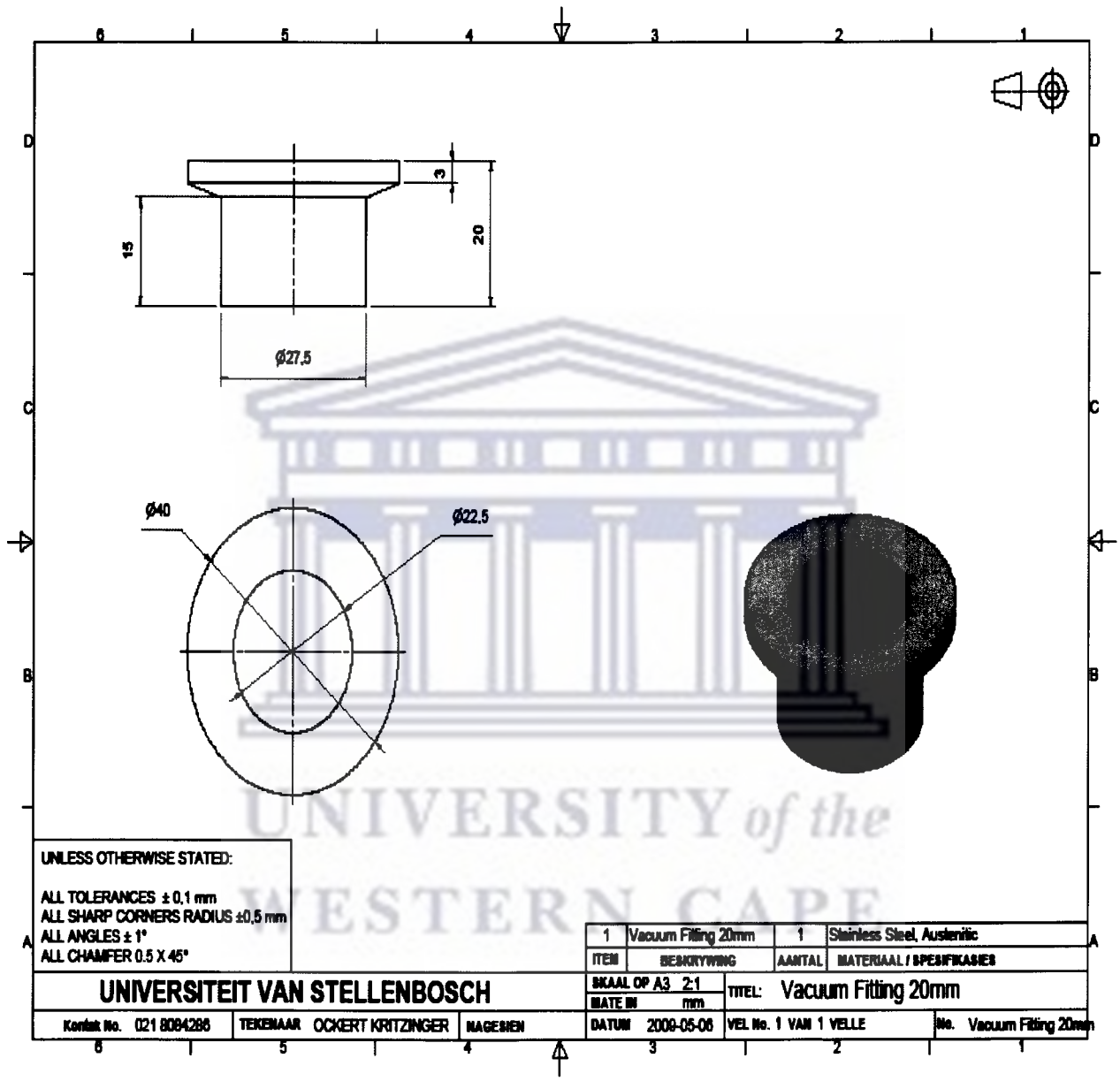

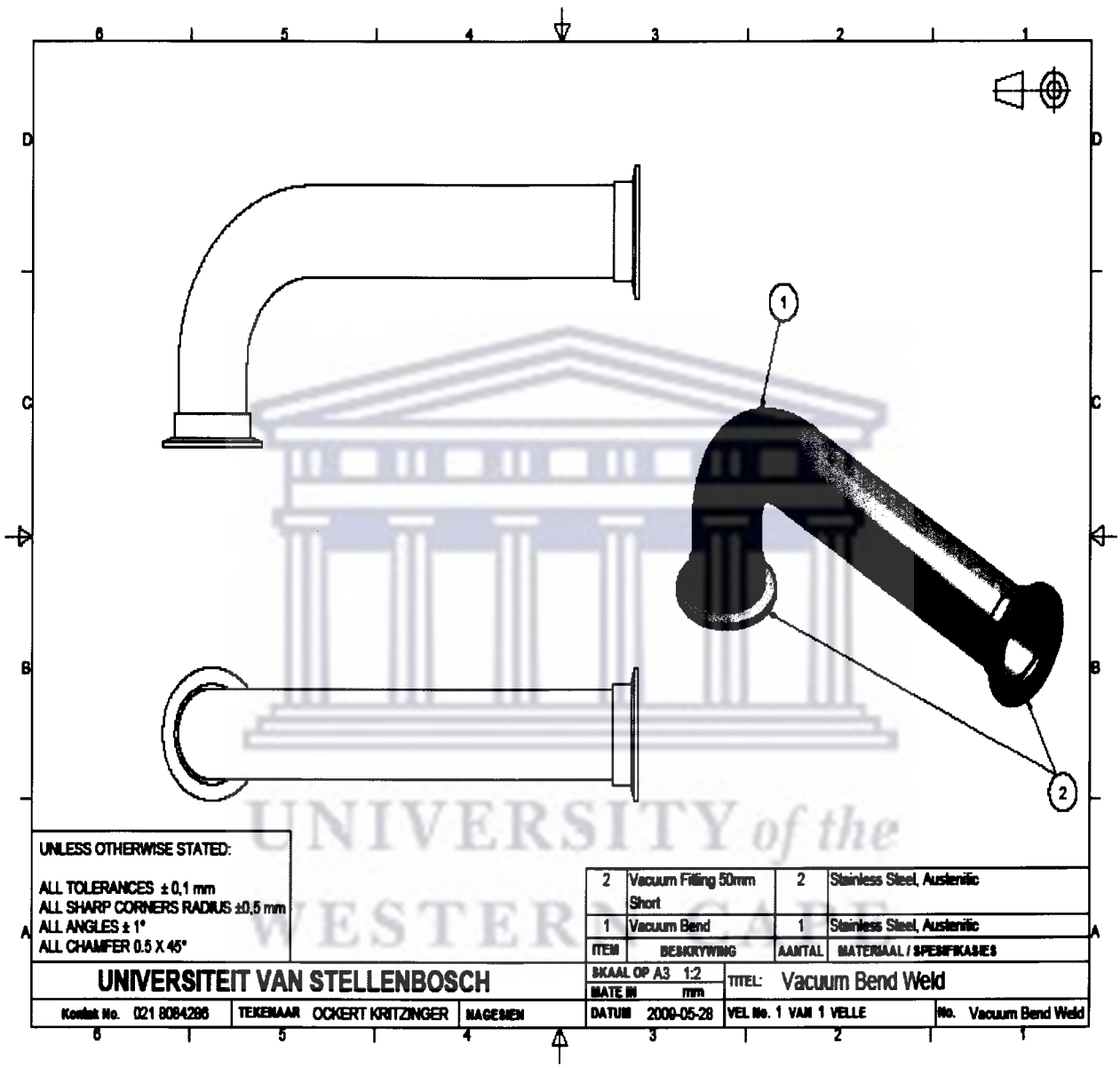

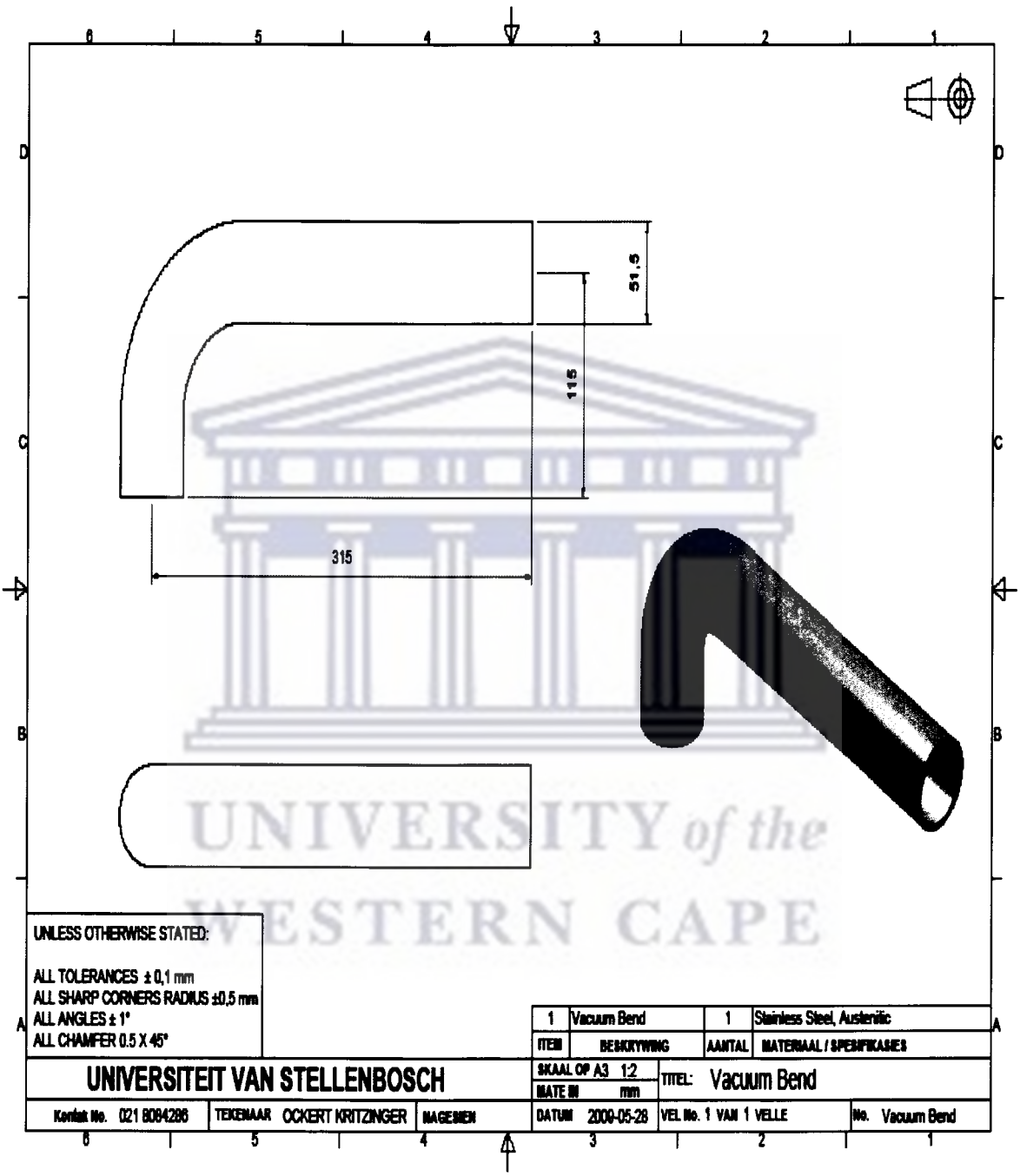

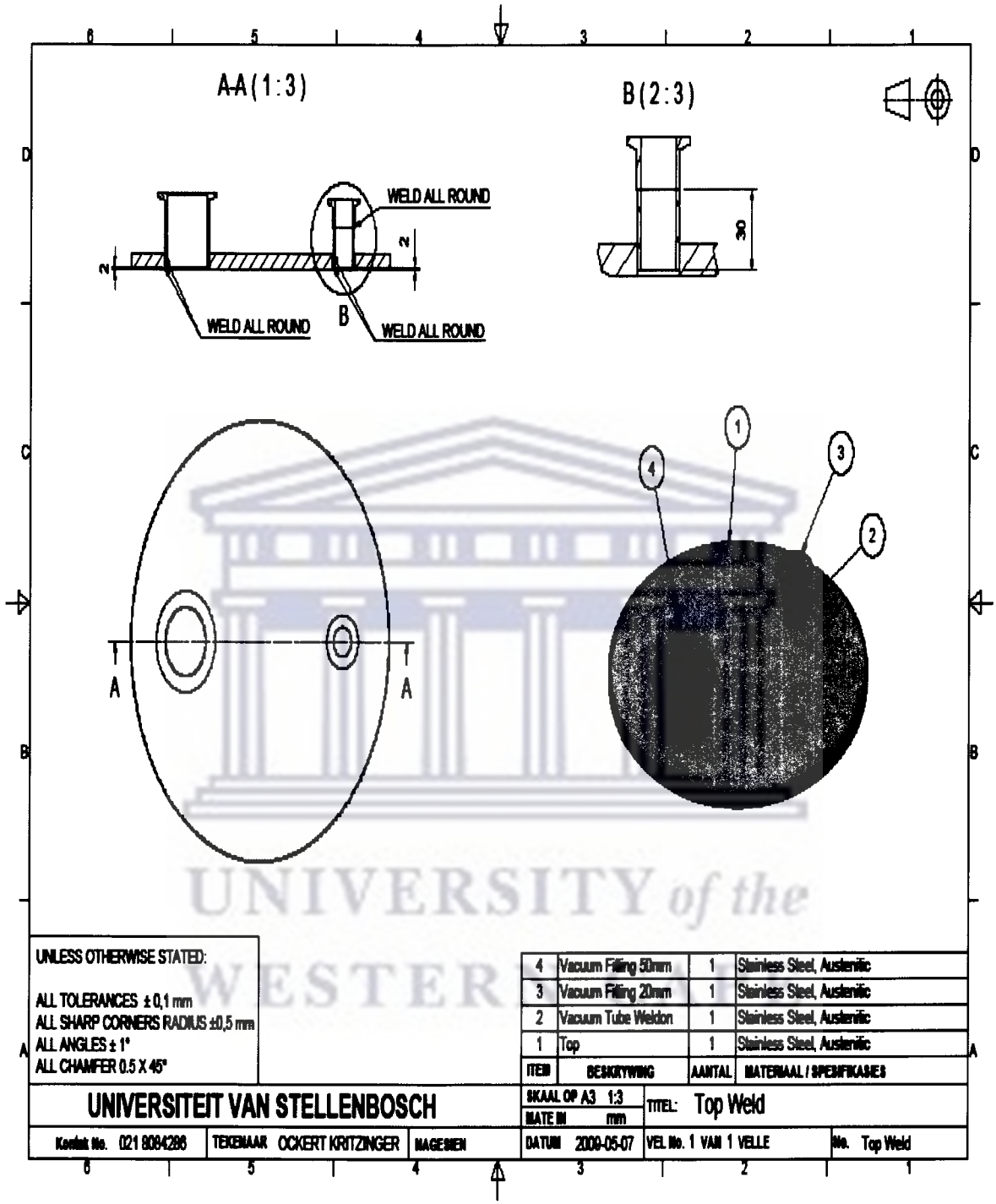

UNLESS OTHERWISE STATED:

ALL TOLERANCES ± 0,1 mm
ALL SHARP CORNERS RADIUS ±0,5 mm
ALL ANGLES ± 1°
ALL CHAMFER 0.5 X 45°

ITEM	BESKRYWING	AANTAL	MATERIAAL / SPESIFIKASIES
4	Vacuum Fitting 50mm	1	Stainless Steel, Austenitic
3	Vacuum Fitting 20mm	1	Stainless Steel, Austenitic
2	Vacuum Tube Weldon	1	Stainless Steel, Austenitic
1	Top	1	Stainless Steel, Austenitic

UNIVERSITEIT VAN STELLENBOSCH

SKAAL OP A3 1:3
MATE IN mm

TITEL: Top Weld

Kontak No. 021 8084286 | TEKENAAR OCKERT KRITZINGER | NAGESIEN | DATUM 2009-05-07 | VEL No. 1 VAN 1 VELLE | No. Top Weld

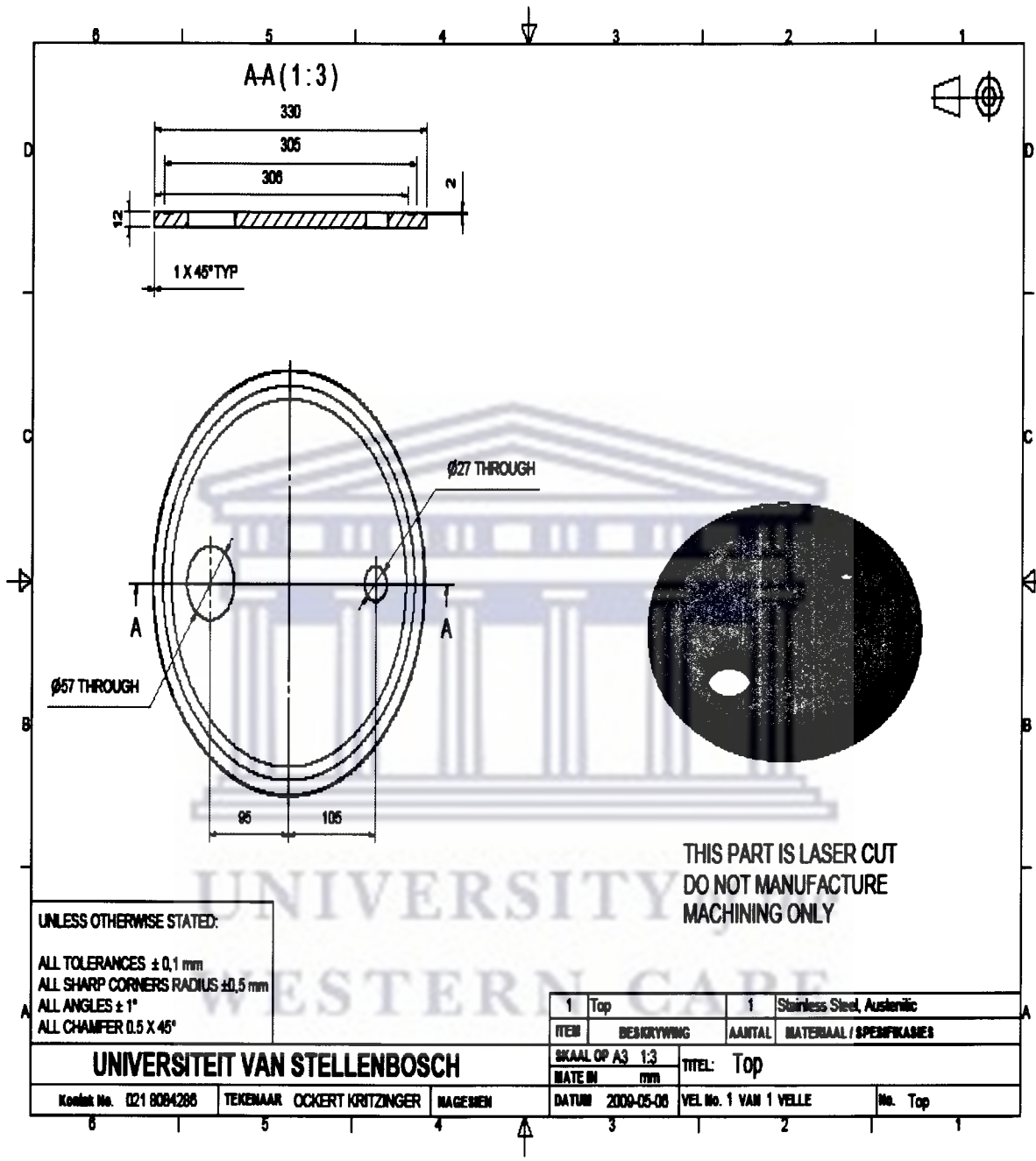

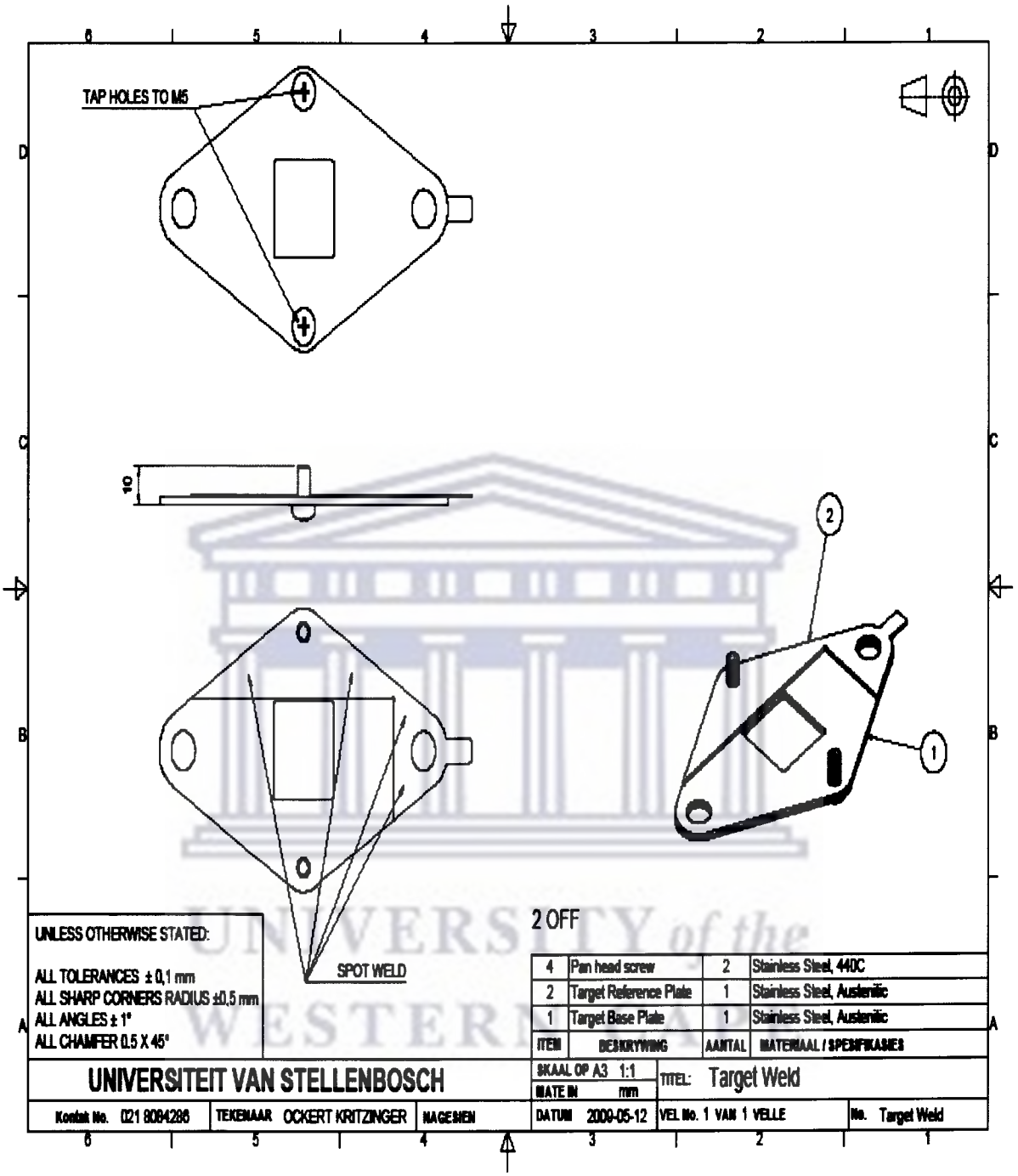

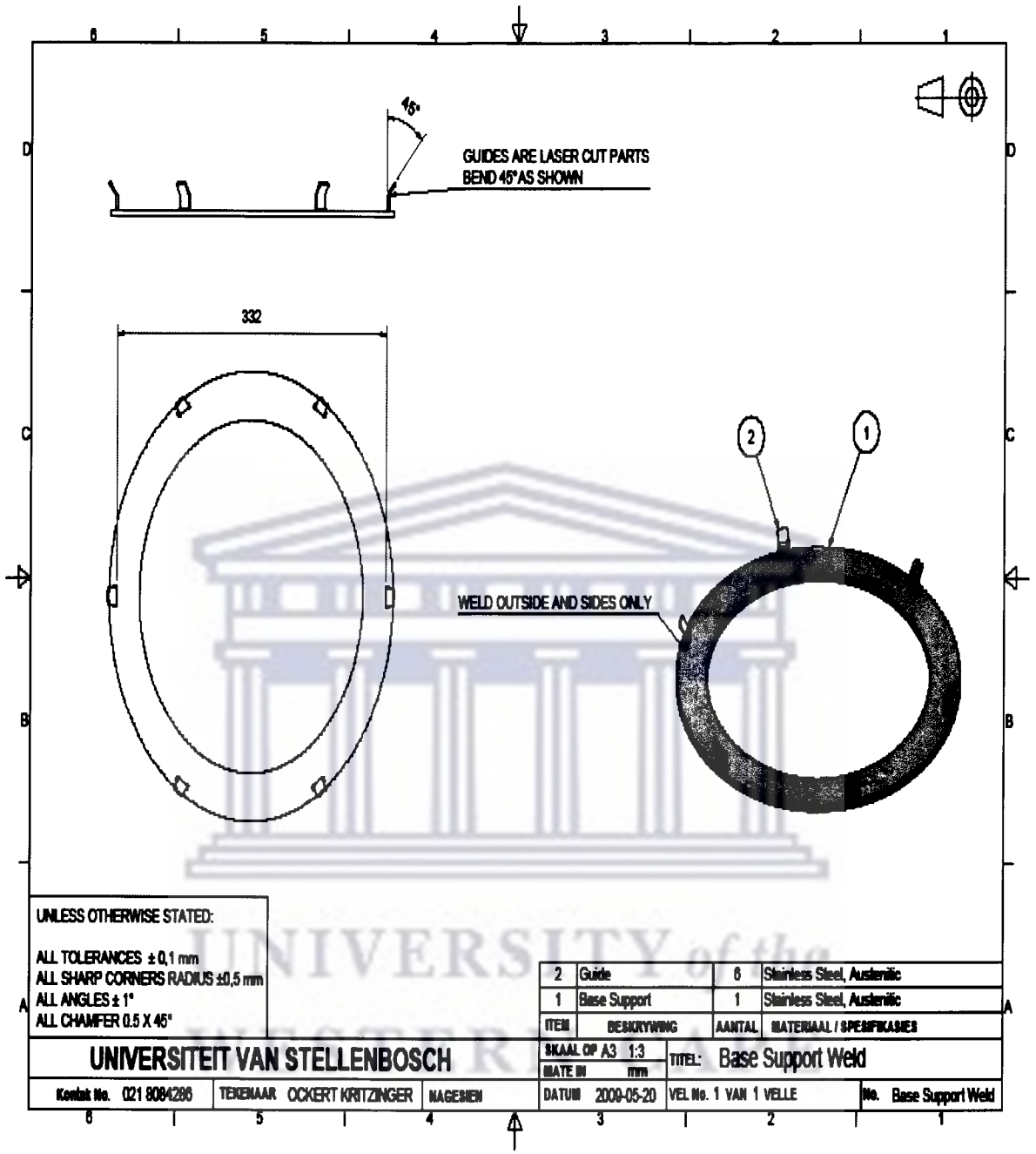

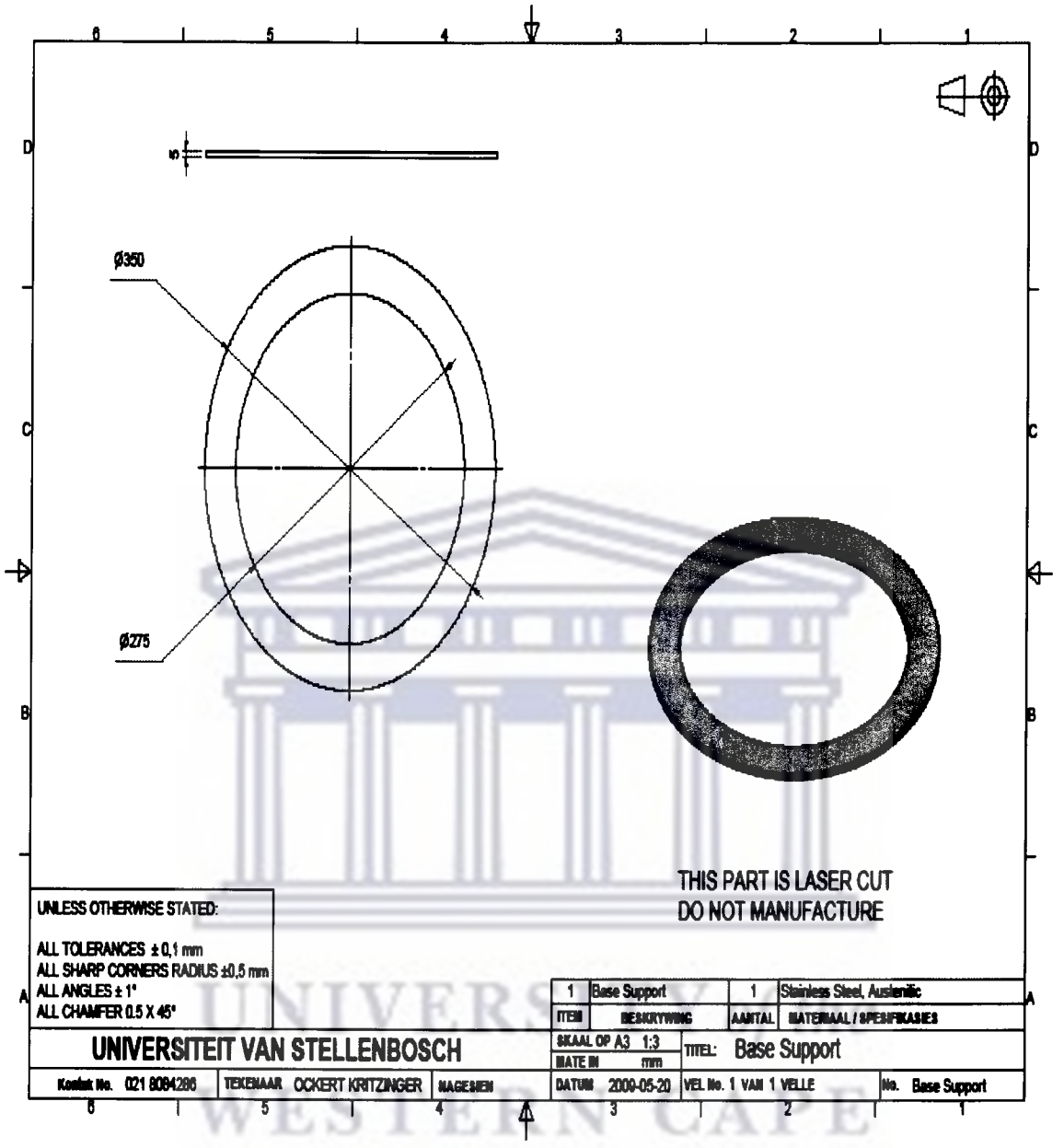

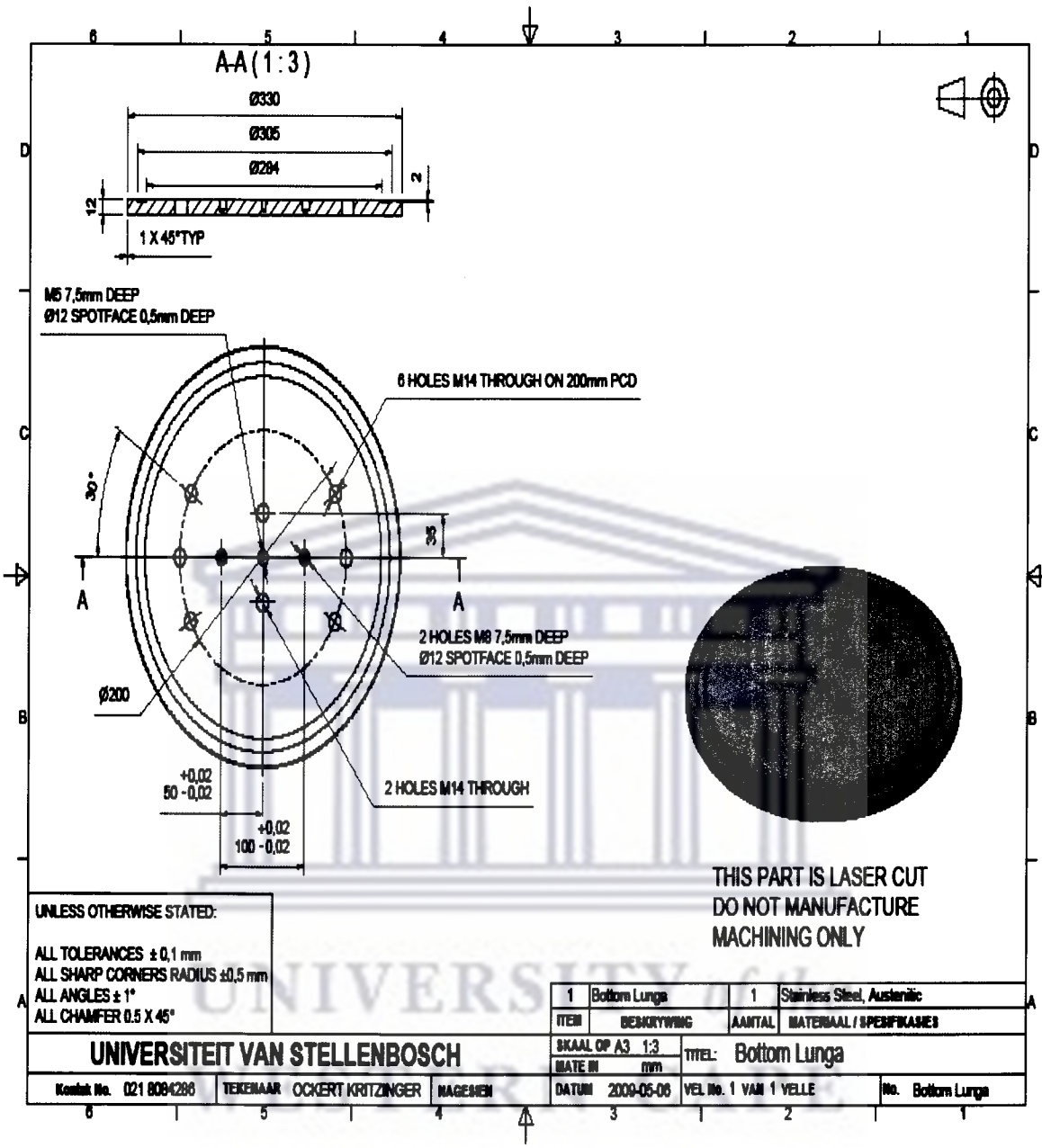

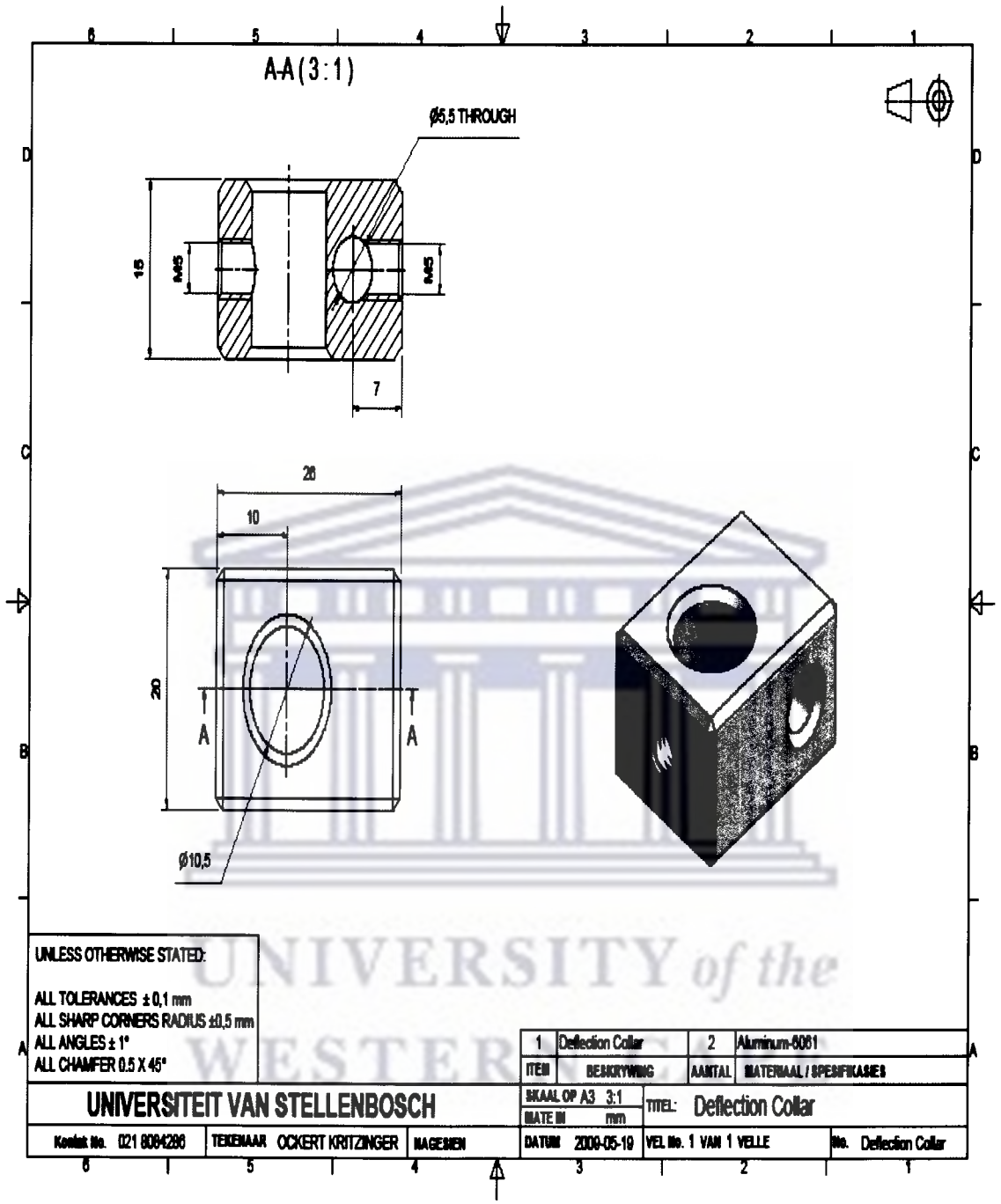

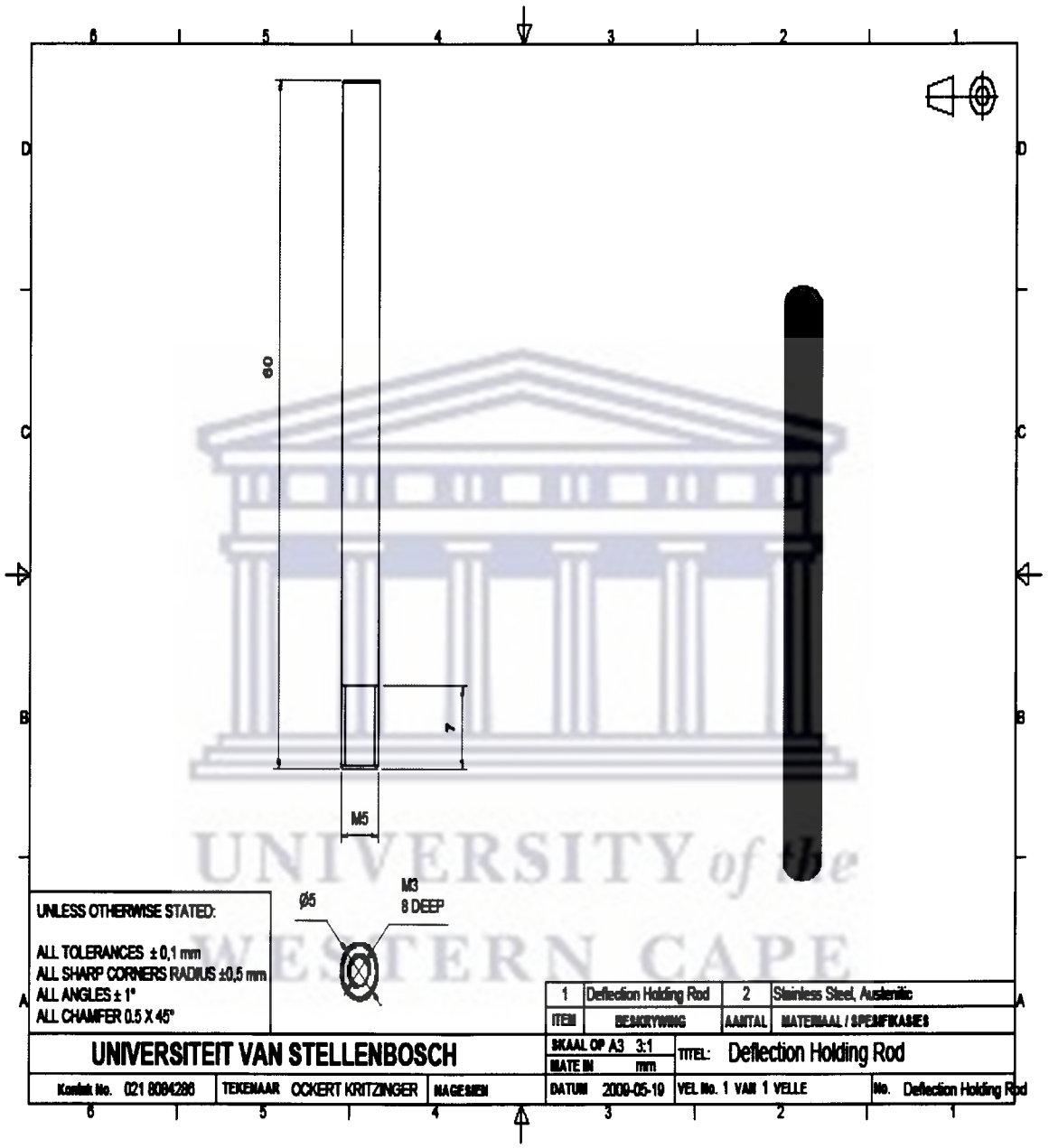

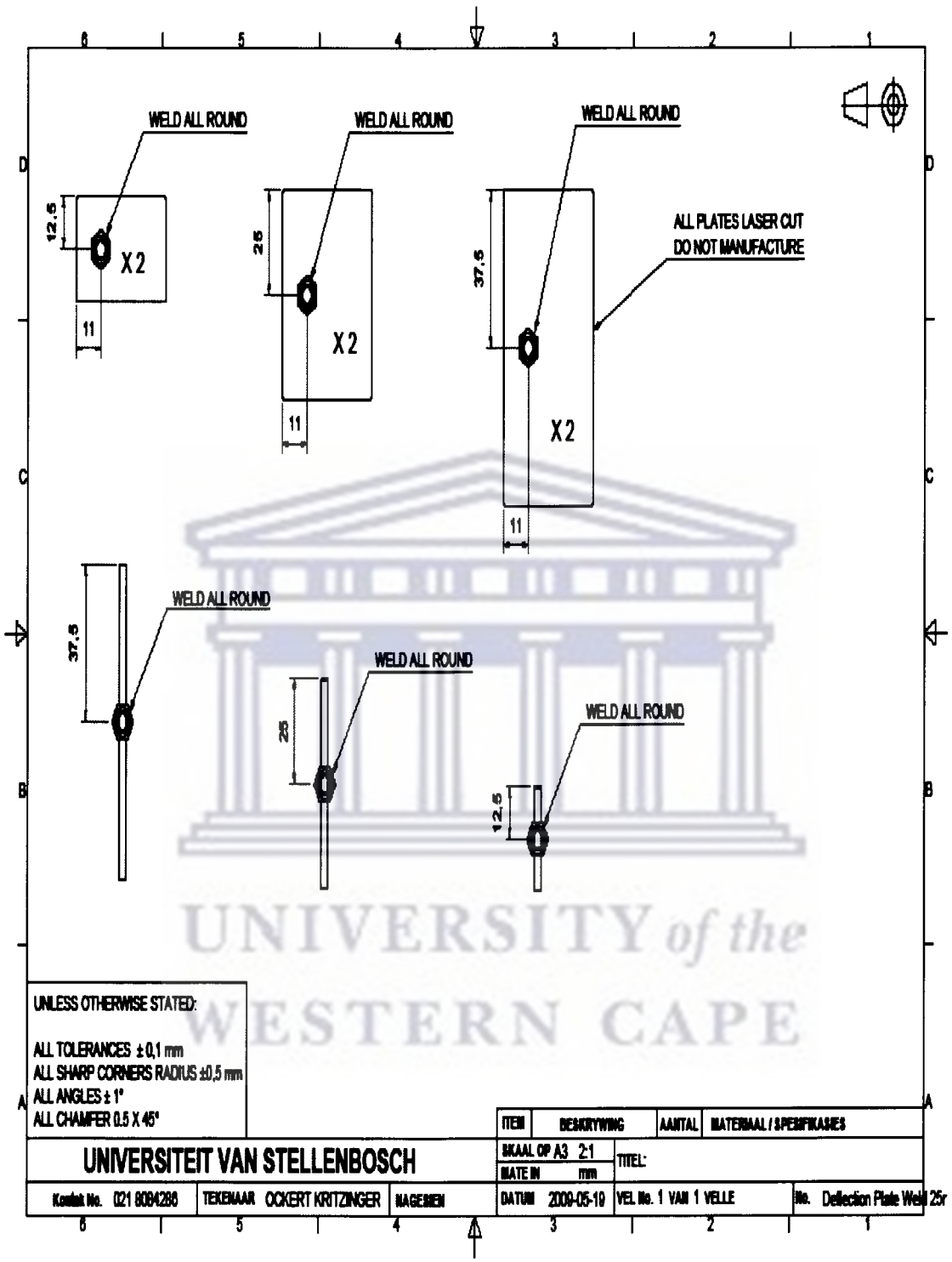

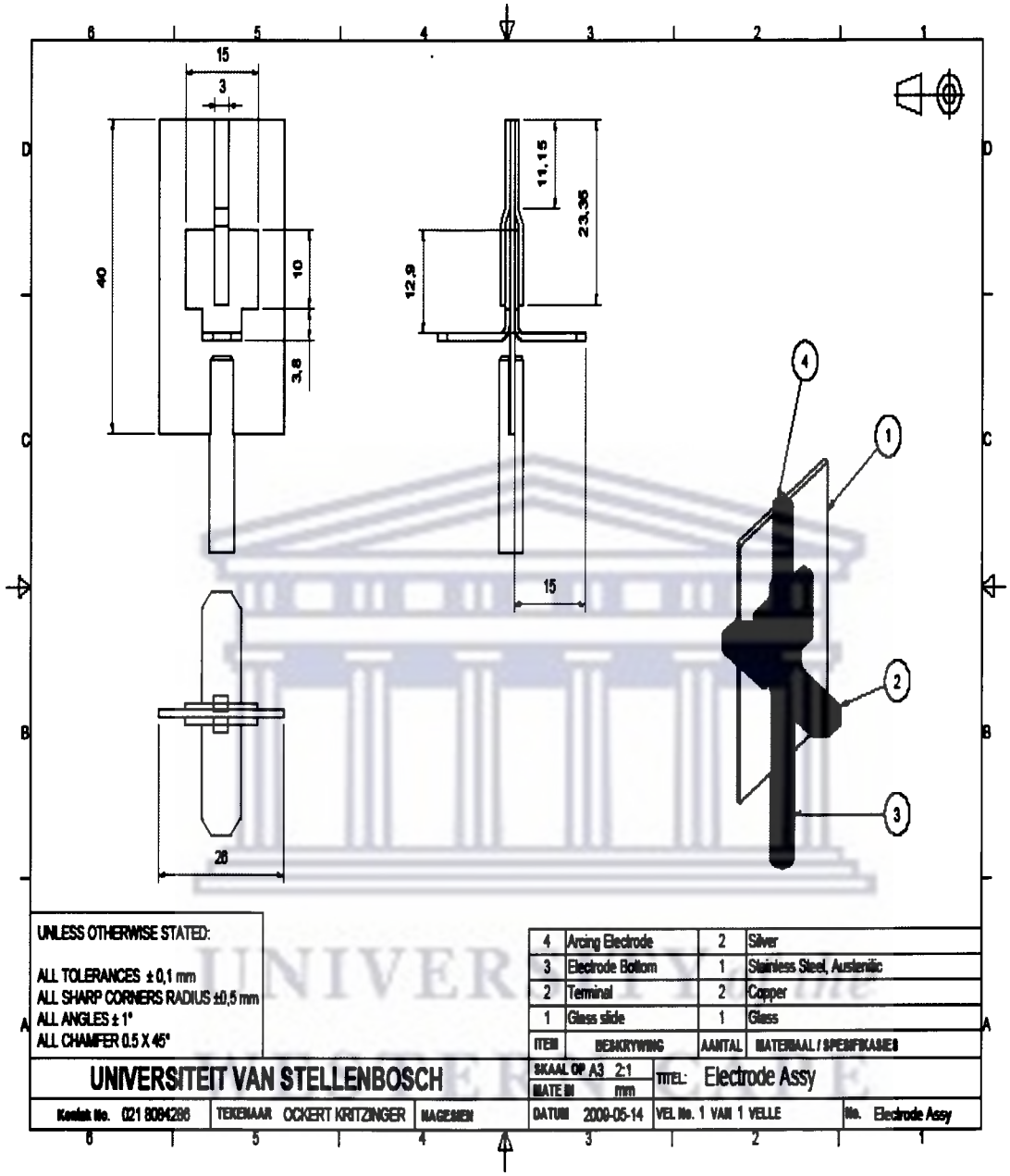

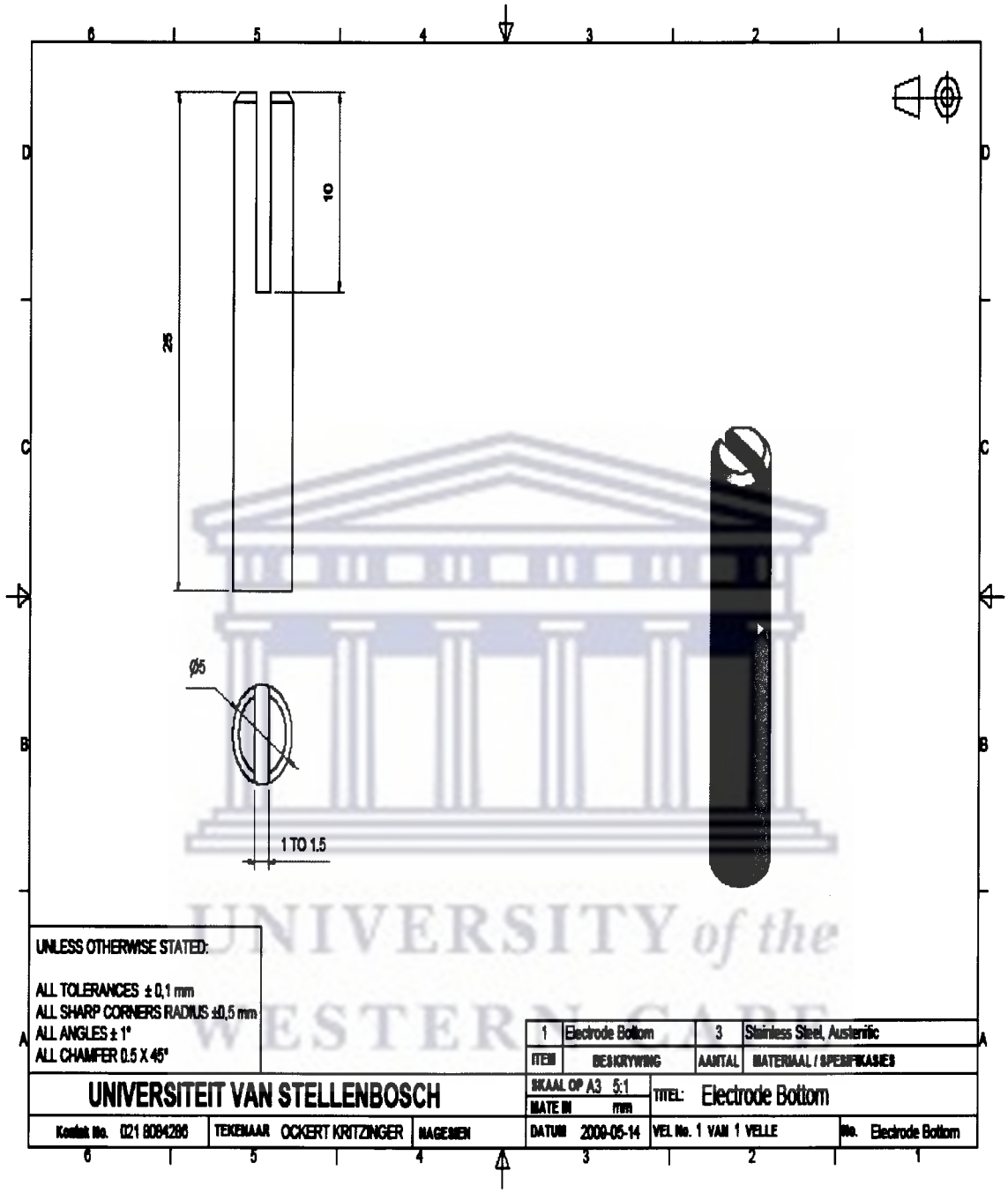

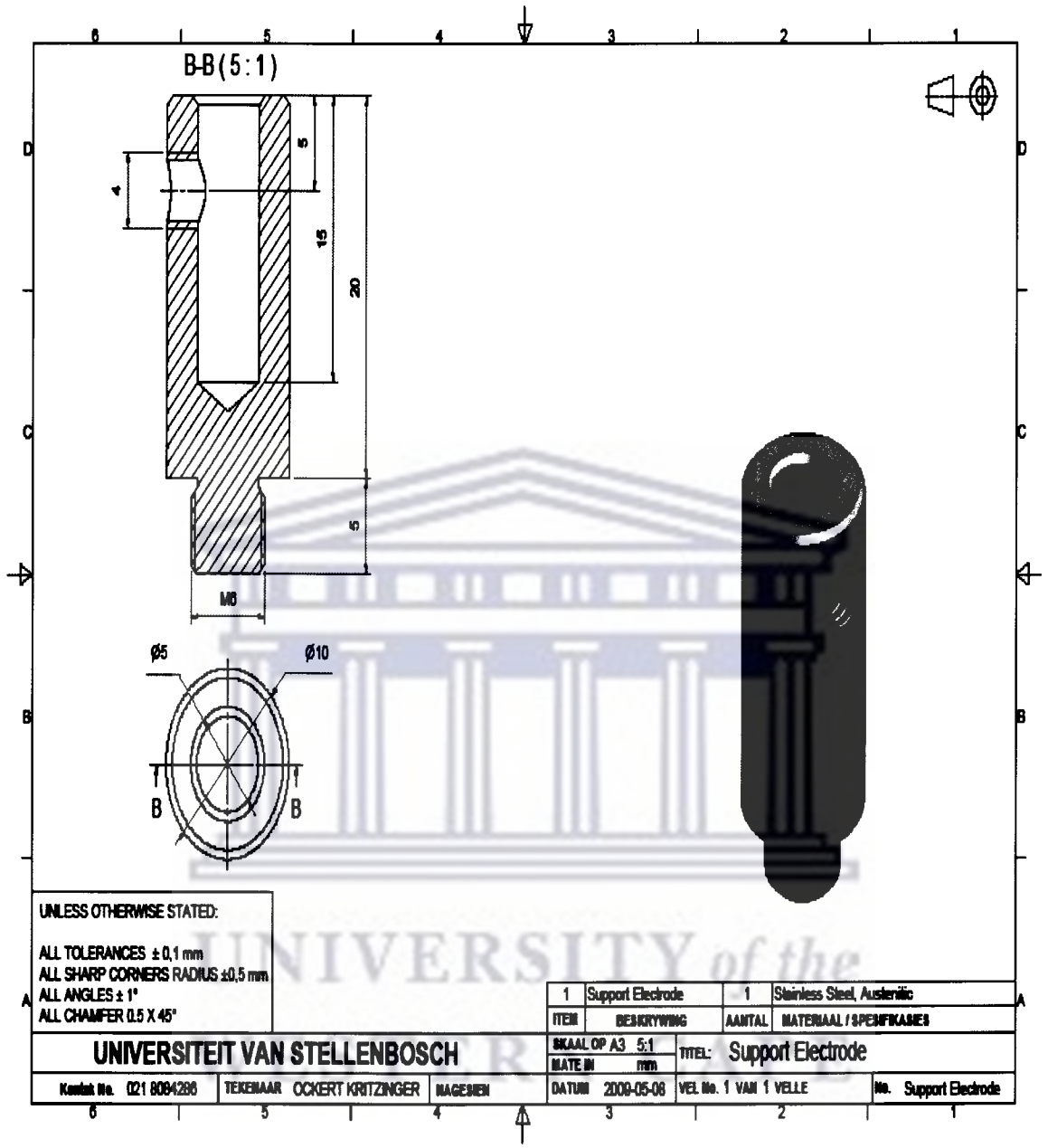

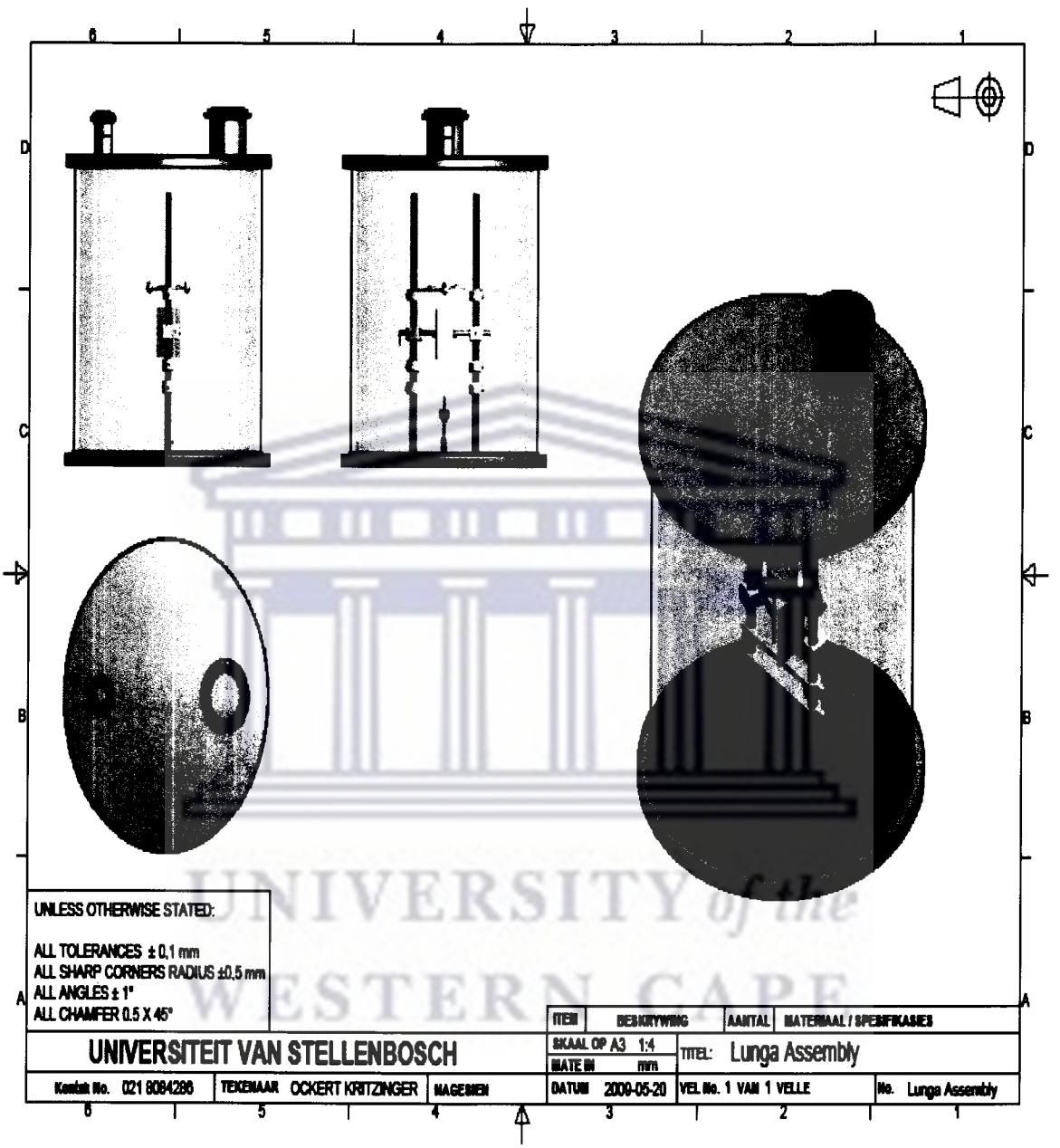

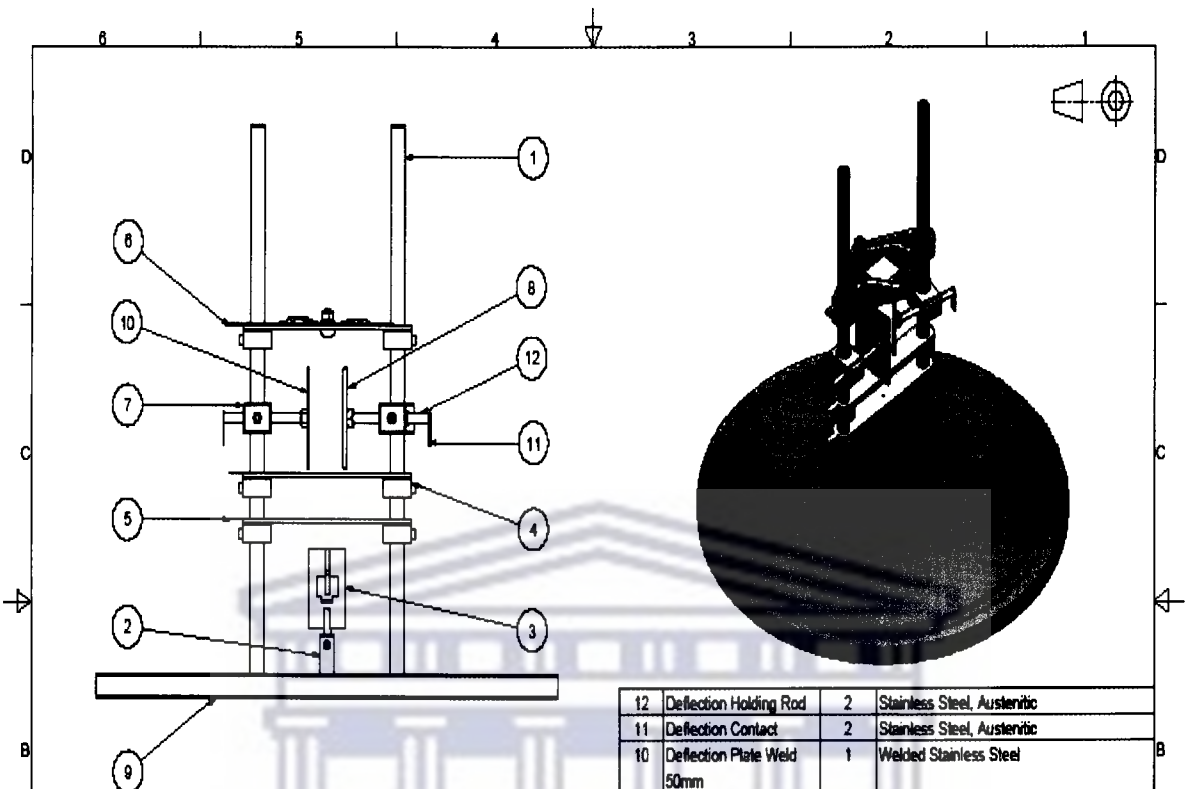

ITEM	BESKRYWING	AANTAL	MATERIAAL / SPESIFIKASIES
12	Deflection Holding Rod	2	Stainless Steel, Austenitic
11	Deflection Contact	2	Stainless Steel, Austenitic
10	Deflection Plate Weld 50mm	1	Welded Stainless Steel
9	Bottom Lunga	1	Stainless Steel, Austenitic
8	Deflection Rod Weld 50mm	1	Welded Stainless Steel
7	Deflection Collar Assy	2	
6	Target Assy	1	
5	Collimator Hole Assy	2	
4	Collar Assy	6	
3	Electrode Assy	1	
2	Electrode Holder Assy	1	
1	Support Plastic	2	Polycarbonate, Clear

UNLESS OTHERWISE STATED:

ALL TOLERANCES ± 0,1 mm
ALL SHARP CORNERS RADIUS ±0,5 mm
ALL ANGLES ± 1°
ALL CHAMFER 0.5 X 45°

UNIVERSITEIT VAN STELLENBOSCH

SKAAL OP A3 1:2
MATE IN mm
TITEL: Lunga Plate Assy

Kontak No. 021 8084286 | TEKENAAR OCKERT KRITZINGER | NAGESIEN | DATUM 2009-05-14 | VEL No. 1 VAN 1 VELLE | No. Lunga Plate Assy